

---

## **Affidavit**

I hereby declare that I have written the present thesis independently, that I have not previously submitted it at any other university or in any other degree program as an examination performance, and that I have used no sources or aids other than those indicated. All passages taken either literally or in substance from publications or other external sources are clearly marked as such.

---

Place, Date

---

Signature

## **Eidesstattliche Erklärung**

Hiermit erkläre ich, dass ich die vorliegende Arbeit selbstständig verfasst habe, dass ich sie zuvor an keiner anderen Hochschule und in keinem anderen Studiengang als Prüfungsleistung eingereicht habe und dass ich keine anderen als die angegebenen Quellen und Hilfsmittel benutzt habe. Alle Stellen der Arbeit, die wörtlich oder sinngemäß aus Veröffentlichungen oder aus anderweitigen fremden Äußerungen entnommen wurden, sind als solche kenntlich gemacht.

---

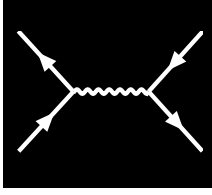
Ort, Datum

---

Unterschrift

---

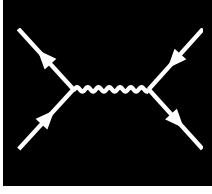
P R E A M B L E



---

# ABSTRACT





# CONTENTS

<b>1</b>	<b>Introduction</b>	<b>1</b>
<b>2</b>	<b>Foundations and Models</b>	<b>3</b>
2.1	The do-it-all Hamiltonian . . . . .	3
2.2	The Born-Oppenheimer approximation . . . . .	4
2.3	Density functional theory . . . . .	5
2.4	Wannier projection . . . . .	6
2.4.1	Multi-orbital Wannier functions . . . . .	7
2.4.2	Maximally localized Wannier functions . . . . .	7
2.5	The multi-orbital Hubbard model . . . . .	7
2.5.1	Fourier transform of the Coulomb term . . . . .	9
2.5.2	More symmetries, assumptions and the Kanamori-Hamiltonian . . . . .	10
2.6	The single-band Hubbard Hamiltonian . . . . .	11
<b>3</b>	<b>Quantum many-body framework</b>	<b>13</b>
3.1	One-particle Green's functions . . . . .	13
3.2	Self-energy . . . . .	17
3.3	Two-particle Green's functions . . . . .	19
3.4	Susceptibility . . . . .	24
3.5	Bethe-Salpeter equation . . . . .	25
3.6	Schwinger-Dyson equation . . . . .	27
3.7	Vertex asymptotics . . . . .	30
3.7.1	Kernel-function asymptotics . . . . .	31
3.7.2	U-range asymptotics . . . . .	35
3.7.3	High-frequency Bethe-Salpeter equation with vertex asymptotics . . . . .	37
3.8	Dynamical mean-field theory . . . . .	38
3.9	Dynamical vertex approximation . . . . .	40
3.10	Self-consistent dynamical vertex approximation . . . . .	45
3.11	Eliashberg equation . . . . .	47
3.11.1	Derivation of the pairing vertex $\Gamma_{pp}$ within ladder-D $\Gamma$ A . . . . .	50
3.11.2	Symmetry of the gap function . . . . .	52
3.11.3	Efficient solving of the Eliashberg equation via a Fourier transform . . . . .	53
<b>4</b>	<b>The code</b>	<b>55</b>
4.1	Structure and design choices . . . . .	55
4.1.1	Parallelization via MPI . . . . .	56

4.1.2	Memory reduction through symmetry . . . . .	56
4.1.3	Object-oriented API . . . . .	57
4.1.4	Setup and execution . . . . .	58
4.1.5	Configuration . . . . .	59
4.1.6	Input files . . . . .	62
4.2	Result validation . . . . .	63
5	Conclusions and Outlook	65

CHAPTER

**1**

---

---

# INTRODUCTION



## CHAPTER

## 2

FOUNDATIONS AND  
MODELS

## 2.1 The do-it-all Hamiltonian

In the realm of solid state physics, the many-body Schrödinger equation plays a crucial role in understanding the behavior of electrons in crystalline materials. This equation provides a fundamental framework for describing the quantum mechanical interactions between multiple electrons within a solid. The Schrödinger Hamiltonian for a system consisting of  $N_{\text{el}}$  electrons and  $N_{\text{ion}}$  atomic cores — in its full beauty — reads

$$\begin{aligned} \mathcal{H} = & -\frac{\hbar^2}{2M} \sum_i^{N_{\text{ion}}} \nabla_{\mathbf{R}_i}^2 - \frac{\hbar^2}{2m} \sum_i^{N_{\text{el}}} \nabla_{\mathbf{r}_i}^2 + \frac{1}{2} \sum_{i \neq j}^{N_{\text{ion}}} \frac{Z_i Z_j e^2}{|\mathbf{R}_i - \mathbf{R}_j|} + \\ & + \frac{1}{2} \sum_{i \neq j}^{N_{\text{el}}} \frac{e^2}{|\mathbf{r}_i - \mathbf{r}_j|} - \sum_i^{N_{\text{el}}} \sum_j^{N_{\text{ion}}} \frac{Z_j e^2}{|\mathbf{r}_i - \mathbf{R}_j|} + \mathcal{V}_R, \end{aligned} \quad (2.1)$$

where  $\mathbf{r}_i$  ( $\mathbf{R}_i$ ) are the positions of the electrons (ions),  $m$  ( $M$ ) their respective masses and  $Z_i$  the atomic number of the cores from which the crystal is constructed. The Hamiltonian above can be described in a very simple manner: the first two terms describe the kinetic energy of the ions and electrons, whereas the third and fourth terms denote the mutual Coulomb interaction between all ions and electrons. The second to last term corresponds to the coupling between the ions and electrons and finally  $\mathcal{V}_R$  expresses any relativistic effects<sup>[1]</sup>. The “only” thing left to do is solve the Schrödinger equation using the Hamiltonian of Eq. (2.1)

$$\mathcal{H}\psi(\{\mathbf{r}_i\}, \{\mathbf{R}_i\}) = E\psi(\{\mathbf{r}_i\}, \{\mathbf{R}_i\}), \quad (2.2)$$

which is easier said than done. The primary problem one faces by trying to do exactly that is the sheer number of particles present in a crystalline material. To be more precise, the wavefunction needed to fulfil the eigenvalue equation above would have to depend on all the degrees of freedom of  $\mathcal{O}(10^{23})$  electrons and atoms present in solids. The exponential growth in the number of configurations makes it computationally infeasible to directly calculate or even store this quantity, and already a very small number of electrons and atoms  $\mathcal{O}(10)$  exceeds the capability of most modern supercomputers. Thus, one goal of condensed matter physicists is not to find the underlying original Hamiltonian

<sup>[1]</sup> e.g., spin-orbit coupling, relativistic mass correction, anomalous magnetic moments, relativistic Doppler shifts, Zitterbewegung, etc. An instructive example are the relativistic effects that take place in mercury: The binding orbitals of mercury are Lorentz-contracted due to the high speed of the electrons inside these orbitals. This results in a reduction in bonding strength, where ultimately mercury is forming a liquid at room temperatures. In most real solids however, relativistic effects are always negligible and this term will not play a significant role in the majority of calculations.



but instead to construct approximate models that contain all the physics necessary while still being controllable and numerically feasible.

Usually, approaches to approximate Eq. (2.1) fall into two main categories: (i) using approximate methods to solve the exact Hamiltonian, or (ii) applying (more) exact methods to solve an approximate, mathematically simpler Hamiltonian. Density functional theory (DFT), as an example, falls under the first category, whereas dynamical mean-field theory (DMFT) or the dynamical vertex approximation (D $\Gamma$ A) reside in category two. The latter build upon a model Hamiltonian which usually incorporates only a subset of all degrees of freedom, e.g., specific orbitals of atomic shells. In modern calculations, a combination of different tools is used to calculate physical properties of materials. For example, a DFT calculation provides a band structure, where the most relevant orbitals are picked, wherefrom more sophisticated methods, such as DMFT or D $\Gamma$ A can be applied. Within this thesis, we mainly focus on the method of dynamical vertex approximation, however, we will give a short introduction to DFT and DMFT later to complete the spectrum.

## 2.2 The Born-Oppenheimer approximation

Almost a century ago it was caught that the timescales of the electronic and ionic systems are tremendously different due to their large difference in masses. An electron is around a factor 1800 lighter than a proton. Cores in real solids that contain, e.g., transition metal elements, are five orders of magnitude heavier than electrons. Since relaxation time scales inversely with mass, the electrons usually relax in a much shorter time frame than the ionic cores do, hence one can treat them to be always in the equilibrium position as the cores move through the lattice. This allows us, to a very good approximation, to solve the electronic degrees of freedom for static ionic coordinates. This approximation, called the Born-Oppenheimer approximation, is highly useful in condensed matter physics since it enables the study of electronic band structures, energy levels, and transport properties without the need to explicitly account for the complex interactions between electrons and lattice vibrations induced by the motion of ionic cores. However, there are certain phenomena, e.g., conventional phonon-mediated superconductivity, where the coupling of lattice vibrations with electrons can not be neglected. Luckily, there exist methods, like perturbation theory, which allow to circumvent this apparent issue. Within the regime of the Born-Oppenheimer approximation, the Hamiltonian of Eq. (2.1) reduces to

$$\mathcal{H}_{\text{B-O}} = -\frac{\hbar^2}{2m} \sum_i^{N_{\text{el}}} \nabla_{\mathbf{r}_i}^2 + \frac{1}{2} \sum_{i \neq j}^{N_{\text{el}}} \frac{1}{|\mathbf{r}_i - \mathbf{r}_j|} + \sum_i^{N_{\text{el}}} \mathcal{V}_{\text{ext}}(\mathbf{r}_i), \quad (2.3)$$

where  $\mathcal{V}_{\text{ext}}$  describes any external potential, e.g., from ions of the lattice. The other quantities appearing in Eq. (2.3) have already been introduced in Eq. (2.1). This approximation will serve as the basis for all upcoming models if not stated otherwise.

Despite this large simplification, the eigenvalues and the wavefunctions of the Hamiltonian in Eq. (2.3) are still impossible to compute for real-world solids. Most of the difficulties lie in the second term of Eq. (2.3), which describes the Coulomb interaction between pairs of electrons. Due to this mutual electromagnetic interaction, the evolution of every electron is influenced by all other electrons present. Hence all electrons are correlated with each other. In general, these effects are of course not negligible, however in some materials<sup>[2]</sup>, where the electrons are very mobile, screening

---

<sup>[2]</sup> E.g. for most metals.

effects take place which weaken the Coulomb interaction between the electrons. In this context, a very successful ansatz to make Eq. (2.3) treatable is to model the system as electrons interacting with an effective mean-field generated by all other electrons in its proximity. Such a mean field approach is density functional theory.

## 2.3 Density functional theory

The basic idea of density functional theory (DFT) is to work with a simple quantity, i.e., the electron density  $\rho(\mathbf{r})$ , instead of trying to solve the ab-initio Hamiltonian of Eq. (2.3) - or other, mathematically simpler variants - through complicated many-body wavefunctions. This is possible, at least for the ground state energy and its derivatives, thanks to the two Hohenberg-Kohn theorems [1], which in essence state that (i) the ground state energy is a unique functional of the electron density  $E[\rho(\mathbf{r})]$  (ii) which is minimized at the ground state density  $\rho(\mathbf{r}) = \rho_0(\mathbf{r})$ . This looks already quite promising, however, DFT lacks in some aspects: firstly, the two H-K theorems do not suggest any constructive/mathematical way to obtain the energy functional; secondly, this only holds for the ground state density. There is no way to extract any information from excited states; and lastly, the  $3N$ -dimensional object  $\psi(\{\mathbf{r}_i\})$  is compressed into a three-dimensional object  $\rho(\mathbf{r})$ . Consequently, an arbitrarily tiny variation in  $\rho(\mathbf{r})$  might correspond to a huge change in  $E[\rho(\mathbf{r})]$ .

The big question is: “How does one approximate the energy functional  $E[\rho(\mathbf{r})]$ ?”. To answer this, we start with splitting up the energy functional to distinguish different contributions,

$$E[\rho(\mathbf{r})] = T[\rho(\mathbf{r})] + E_H[\rho(\mathbf{r})] + \int d^3r \rho(\mathbf{r}) \mathcal{V}(\mathbf{r}) + E_{XC}[\rho(\mathbf{r})]. \quad (2.4)$$

Here,  $T[\rho(\mathbf{r})]$  denotes the kinetic energy of the electrons. Computing the kinetic energy functional often turns out to be very challenging.  $E_H[\rho(\mathbf{r})]$  is the electrostatic energy (inter alia self-interaction of electrons), given by the Hartree-term

$$E_H[\rho(\mathbf{r})] = \frac{1}{2} \int d^3r \int d^3r' \frac{\rho(\mathbf{r})\rho(\mathbf{r}')}{|\mathbf{r} - \mathbf{r}'|}. \quad (2.5)$$

The potential term includes energies of electrons in external potentials (e.g., nuclei) and is usually not hard to calculate. Lastly,  $E_{XC}[\rho(\mathbf{r})]$  includes everything else, i.e., the exchange and correlation energies. Dealing with the potential and the Hartree-term is easy compared to the treatment of the kinetic and exchange/correlation functional. There are many ways to construct the kinetic and XC functionals. The most frequently used framework to include the main contribution to the kinetic energy functional is Kohn-Sham DFT and exchange/correlation functionals can be obtained by the local density approximation (LDA) or higher-order variants within K-S DFT, such as different flavours of generalized gradient approximations (GGA). Stepping higher on Jacob’s ladder<sup>[3]</sup>, more sophisticated methods are hyper-GGA or several variants of (range-separated) hybrid functionals [2].

<sup>[3]</sup>Refers to a hierarchical classification of density functional approximations (DFAs) used in Kohn-Sham density functional theory (DFT). The ladder represents a sequence of increasingly accurate and complex approximations for the exchange-correlation energy, which is a key component of the total energy in DFT. Jacob’s Ladder begins with the simplest and least accurate approximations at the lower rungs and progresses towards more sophisticated and accurate methods at the higher rungs. Each rung represents a level of approximation that includes additional physical effects and improves upon the previous level.

This already sounds very promising, why should we not stop here and solely describe our metals with DFT? This apparent question can be answered very straightforwardly: increased localization of d or f orbitals and increased correlation effects therein. Since orbitals with higher angular momentum are more localized in real space, electronic densities in those orbitals are higher and consequently, the electrons within those orbitals are more correlated. Consequently, screening of other itinerant electrons is, in a way, suppressed. Therefore, since DFT is a mean-field approach and relies on the concept of screening, it is not very successful in describing those systems. For example, DFT predicts a metallic behavior in partially filled 3d transition metal or 4f rare-earth elements, whereas experiments find them to be insulating. Thus, for strongly correlated materials, sophisticated many-body methods, which do not approximate the Born-Oppenheimer Hamiltonian of Eq. (2.3), are needed. However, since all many-body techniques are numerically expensive, a straightforward application to the Hamiltonian of Eq. (2.3) is not feasible, thus model Hamiltonians, such as the Hubbard Hamiltonian — the modern standard Hamiltonian of strongly correlated condensed matter systems, which is described in Sec. 2.5 — are needed.

At the time of writing this thesis, modern DFT calculations are usually performed with, e.g., Wien2k [3] or VASP [4].

## 2.4 Wannier projection

Within DFT+others<sup>[4]</sup> approach, a Wannier projection is used to develop localized wavefunctions, also called Wannier functions, from extended Bloch wavefunctions used in DFT. These localized Wannier functions are created for the correlated orbitals and are then interpreted as the localized orbitals of multi-orbital models, such as the Hubbard model, which will be discussed later in Sec. 2.5. The eigenstates of the Schrödinger equation in a periodic lattice are Bloch functions of the form

$$\psi_{n\mathbf{k}}(\mathbf{r}) = e^{i\mathbf{k}\mathbf{r}}u_n(\mathbf{r}), \quad (2.6)$$

where  $u_n(\mathbf{r} + \mathbf{R}) = u_n(\mathbf{r})$  incorporates the periodicity of the lattice and  $n$  denotes the band index. To obtain a local set of basis functions, one applies a Fourier transform to the Bloch functions,

$$w_{n\mathbf{R}}(\mathbf{r}) = \frac{1}{\sqrt{N}} \sum_{\mathbf{k} \in \text{BZ}} e^{-i\mathbf{k}\mathbf{R}} \psi_{n\mathbf{k}}(\mathbf{r}), \quad (2.7)$$

where  $\mathbf{R}$  is a lattice vector and  $w_{n\mathbf{R}}(\mathbf{r})$  is a Wannier function centred around the lattice site  $\mathbf{R}$ . Wannier functions are an equivalent basis in band-space compared to the Bloch functions, however they are not eigenstates of the lattice Hamiltonian. Therefore, in a way, de-localization in energy is what compensates for localization in real space. Additionally, the choice for Eq. (2.7) is not unique, since the Bloch functions have a gauge freedom of a unitary transformation — similar to a basis transformation — which reads

$$\psi_{n_1\mathbf{k}}(\mathbf{r}) = \sum_{n_2} U_{n_1 n_2}^{\mathbf{k}} \psi_{n_2\mathbf{k}}(\mathbf{r}), \quad (2.8)$$

where  $U_{n_1 n_2}^{\mathbf{k}}$  is a unitary matrix, mixing orbitals  $n_1$  and  $n_2$  at each point in  $\mathbf{k}$ -space. Consequently, there is some degree of freedom to Wannier function construction, which can be applied to the creation of maximally localized Wannier functions, for example.

---

<sup>[4]</sup>“Others” being, e.g., DMFT, GW or DfA.

### 2.4.1 Multi-orbital Wannier functions

So far, we assumed a single isolated band with band index  $n$ . This does not capture real-world materials, where one usually has a “spaghetti” of many bands that overlap and hybridize with each other. Let us assume that the number of Bloch bands, which are encompassed in the Wannier projection, is  $L$  and these bands are separated by all other bands present. In this case, the transformation of Eq. (2.8) can be generalized to

$$\tilde{\psi}_{m\mathbf{k}}(\mathbf{r}) = \sum_{n=1}^L U_{mn}^{\mathbf{k}} \psi_{n\mathbf{k}}(\mathbf{r}), \quad (2.9)$$

where  $U_{mn}^{\mathbf{k}} \in L \times L$ . The construction of the Wannier functions follows

$$w_{m\mathbf{R}}(\mathbf{r}) = \sum_{\mathbf{k} \in \text{BZ}} e^{-i\mathbf{k}\mathbf{R}} \sum_{n=1}^L U_{mn}^{\mathbf{k}} \psi_{n\mathbf{k}}(\mathbf{r}), \quad (2.10)$$

which allows for an additional mixing of the Bloch states. In this case, the unitary matrix  $U_{mn}^{\mathbf{k}}$  encodes the gauge freedom of the Wannier projection. A popular unique “gauge fixing” of  $U_{mn}^{\mathbf{k}}$  is through maximally localized Wannier functions.

### 2.4.2 Maximally localized Wannier functions

The idea here is to choose  $U_{mn}^{\mathbf{k}}$  such that the sum of quadratic spreads of the Wannier functions is minimized. This spread of the set of  $L$  Wannier functions in real space is quantified by the localization functional  $\Omega$  and reads

$$\Omega = \sum_m \left[ \langle \mathbf{r}^2 \rangle_m - \langle \mathbf{r} \rangle_m^2 \right] = \sum_m \left[ \langle w_{m\mathbf{R}} | \mathbf{r}^2 | w_{m\mathbf{R}} \rangle - |\langle w_{m\mathbf{R}} | \mathbf{r} | w_{m\mathbf{R}} \rangle|^2 \right]. \quad (2.11)$$

Applying a minimization procedure to the spread of Wannier functions results in a “gauge-fixed”  $\tilde{U}_{mn}^{\mathbf{k}}$ , choosing the unitary transformation uniquely. The resulting Wannier functions are then called maximally localized. Popular programs to calculate maximally localized Wannier functions from plane waves are `wien2wannier` [5] or `wannier90` [6].

## 2.5 The multi-orbital Hubbard model

Now we have acquired enough tools to describe the “standard model” of strongly correlated electron systems. The development of this model dates back to more than a century. As already discussed at the end of Sec. 2.3, for elements with partially filled  $d$  or  $f$  orbitals, a mean-field description, as is the basis for DFT calculations, is not enough to successfully describe microscopic and macroscopic phenomena due to strong electronic correlation. On the other hand, a treatment beyond mean-field of the Born-Oppenheimer Hamiltonian of Eq. (2.3) is currently not possible. Hence, the method of choice is the introduction of a mathematically simpler, but conceptually still very relevant model Hamiltonian, which successfully captures the physical essence of condensed matter. As a result, the Hamiltonian - named for J. Hubbard - was developed.

As a starting point we choose the Hamiltonian of Eq. (2.3) in second quantization

$$\mathcal{H} = \sum_{\sigma} \int d^3r \hat{\psi}_{\sigma}^{\dagger}(\mathbf{r}) \left[ -\frac{\hbar^2}{2m} \nabla_{\mathbf{r}}^2 + \mathcal{V}(\mathbf{r}) \right] \hat{\psi}_{\sigma}(\mathbf{r}) + \frac{1}{2} \sum_{\sigma\sigma'} \int d^3r \int d^3r' \hat{\psi}_{\sigma}^{\dagger}(\mathbf{r}) \hat{\psi}_{\sigma'}^{\dagger}(\mathbf{r}') \frac{e^2}{|\mathbf{r} - \mathbf{r}'|} \hat{\psi}_{\sigma'}(\mathbf{r}') \hat{\psi}_{\sigma}(\mathbf{r}), \quad (2.12)$$

where  $\hat{\psi}_{\sigma}^{(\dagger)}(\mathbf{r})$  are field operators that annihilate (create) an electron with spin  $\sigma$  at position  $\mathbf{r}$ . We can expand these field operators in terms of maximally localized Wannier functions introduced in Sec. 2.4.2, yielding

$$\hat{\psi}_{\sigma}^{(\dagger)}(\mathbf{r}) = \sum_{\mathbf{R}, m} w_{m\mathbf{R}}^{(*)} \hat{c}_{\mathbf{R}m\sigma}^{(\dagger)}, \quad (2.13)$$

where  $w_{m\mathbf{R}}$  is the (maximally localized) Wannier function of orbital  $m$  centred around  $\mathbf{R}$ , and  $\hat{c}_{\mathbf{R}m\sigma}$  the corresponding annihilation operator. Note that the orbitals  $m$  are usually the localized 3d or 4f orbitals in transition metals or rare earth elements. With the help of Eq. (2.13), the Hamiltonian of Eq. (2.12) can be rewritten as

$$\mathcal{H} = - \sum_{\substack{\mathbf{R}\mathbf{R}' \\ m m', \sigma}} t_{mm'}(\mathbf{R}, \mathbf{R}') \hat{c}_{\mathbf{R}m\sigma}^{\dagger} \hat{c}_{\mathbf{R}'m'\sigma} + \frac{1}{2} \sum_{\substack{\mathbf{R}_1 \mathbf{R}_2 \mathbf{R}_3 \mathbf{R}_4 \\ l l' m m' \\ \sigma \sigma'}} U_{lm m' l'}(\mathbf{R}_1, \mathbf{R}_2, \mathbf{R}_3, \mathbf{R}_4) \hat{c}_{\mathbf{R}_1 l \sigma}^{\dagger} \hat{c}_{\mathbf{R}_3 m' \sigma'}^{\dagger} \hat{c}_{\mathbf{R}_4 l' \sigma'} \hat{c}_{\mathbf{R}_2 m \sigma}, \quad (2.14)$$

where  $l l' m m'$  denote different Wannier orbitals, while  $\mathbf{R}_i$  corresponds to a lattice site. Hence, the first term in the Hubbard Hamiltonian represents the kinetic energy part and describes electrons hopping from orbital  $m'$  at  $\mathbf{R}'$  to orbital  $m$  at  $\mathbf{R}$ , possibly changing spin in the process. The probability of the hopping to occur is given by the hopping matrix  $t_{mm'}(\mathbf{R}, \mathbf{R}')$ . The second term in Eq. (2.14) encodes the Coulomb interaction between two electrons. A couple terms of the multiorbital Hubbard Hamiltonian are visually depicted in Fig. 2.1, where a subset of effects of  $t_{mm'}(\mathbf{R}, \mathbf{R}')$  and  $U_{lm m' l'}(\mathbf{R}_1, \mathbf{R}_2, \mathbf{R}_3, \mathbf{R}_4)$  are shown for two lattice sites. For brevity, the hopping matrix  $t_{mm'}(\mathbf{R}, \mathbf{R}')$

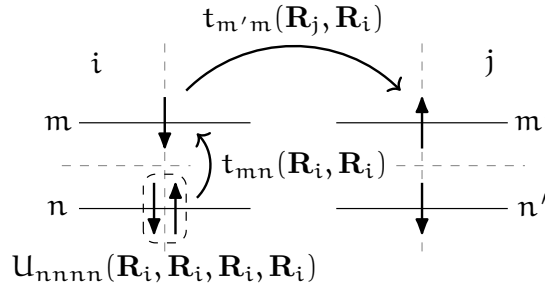


**FIGURE 2.1** – Visual representation of a subset of interaction and hopping terms of Eq. (2.14). We show two lattice sites  $i$  and  $j$  with orbitals  $m, n$  and  $m', n'$ , respectively.

and Coulomb interaction  $U_{lm m' l'}(\mathbf{R}_1, \mathbf{R}_2, \mathbf{R}_3, \mathbf{R}_4)$  are given by

$$t_{mm'}(\mathbf{R}, \mathbf{R}') = - \int d^3r w_{m\mathbf{R}}^*(\mathbf{r}) \left[ -\frac{\hbar^2}{2m} \nabla_{\mathbf{r}}^2 + \mathcal{V}(\mathbf{r}) \right] w_{m'\mathbf{R}'} \quad \text{and} \quad (2.15a)$$

$$U_{lmm'l'}(\mathbf{R}_1, \mathbf{R}_2, \mathbf{R}_3, \mathbf{R}_4) = \int d^3r \int d^3r' w_{l\mathbf{R}_1}^*(\mathbf{r}) w_{m'\mathbf{R}_3}^*(\mathbf{r}') \frac{e^2}{|\mathbf{r} - \mathbf{r}'|} w_{l'\mathbf{R}_4}(\mathbf{r}') w_{m\mathbf{R}_2}(\mathbf{r}). \quad (2.15b)$$

While for Eq. (2.14) we have already restricted ourselves to a subspace of orbitals, it is still too complex to be solved exactly in the general case. The complexity can be further reduced by either placing further assumptions and restrictions or by using symmetries of the Hamiltonian, which are present in the hopping and interaction terms. Note, that Eq. (2.15b) overestimates the repulsive Coulomb interaction since screening effects from electrons outside the orbital subspace are not considered. One way to partly overcome this issue is proposed in the constrained Random Phase Approximation (cRPA). For details on how cRPA works, we refer the reader to, e.g., [7].

### 2.5.1 Fourier transform of the Coulomb term

For reasons that become apparent later, it is more convenient to express the interaction term in Fourier space for diagrammatic calculations. The real-space interaction term in Eq. (2.14) inherently depends on four lattice vectors. However, to simplify the notation, one of these arguments (e.g.,  $\mathbf{R}_4$ ) can be eliminated by expressing the distances relative to the lattice site 4 rather than using their absolute positions. Therefore,

$$\hat{U} = \frac{1}{2} \sum_{\substack{\mathbf{R}_1 \mathbf{R}_2 \mathbf{R}_3 \\ ll'mm' \\ \sigma\sigma'}} U_{lmm'l'}(\mathbf{R}_1, \mathbf{R}_2, \mathbf{R}_3) \hat{c}_{\mathbf{R}_1 l \sigma}^\dagger \hat{c}_{\mathbf{R}_3 m' \sigma'}^\dagger \hat{c}_{0 l' \sigma'} \hat{c}_{\mathbf{R}_2 m \sigma}. \quad (2.16)$$

This quantity naturally fulfils a swapping symmetry, where the simultaneous exchange of both incoming and outgoing particles keeps it invariant, i.e.,

$$U_{lmm'l'}(\mathbf{R}_1, \mathbf{R}_2, \mathbf{R}_3) = U_{mll'm'}(\mathbf{R}_3 - \mathbf{R}_2, -\mathbf{R}_2, \mathbf{R}_1 - \mathbf{R}_2). \quad (2.17)$$

The general Fourier transform of the tensor in Eq. (2.16) with respect to the lattice positions  $\mathbf{R}_i$  yields

$$U_{lmm'l'}^{\mathbf{q}\mathbf{k}\mathbf{k}'} = \sum_{\mathbf{R}_1 \mathbf{R}_2 \mathbf{R}_3} e^{i\mathbf{k}\mathbf{R}_1} e^{-i(\mathbf{k}-\mathbf{q})\mathbf{R}_2} e^{-i(\mathbf{k}'-\mathbf{q})\mathbf{R}_3} U_{lmm'l'}(\mathbf{R}_1, \mathbf{R}_2, \mathbf{R}_3), \quad (2.18)$$

or for the full interaction operator in Eq. (2.14)

$$\hat{U} = \frac{1}{2} \sum_{\substack{\mathbf{q}\mathbf{k}\mathbf{k}' \\ ll'mm' \\ \sigma\sigma'}} U_{lmm'l'}^{\mathbf{q}\mathbf{k}\mathbf{k}'} \hat{c}_{\mathbf{k} l \sigma}^\dagger \hat{c}_{\mathbf{k}' - \mathbf{q} m' \sigma'}^\dagger \hat{c}_{\mathbf{k}' l' \sigma'} \hat{c}_{\mathbf{k} - \mathbf{q} m \sigma}, \quad (2.19)$$

where the Fourier transforms of the creation and annihilation operators are given by

$$\hat{c}_{\mathbf{k} l \sigma}^{(\dagger)} = \sum_{\mathbf{R}} e^{(-)i\mathbf{k}\mathbf{R}} \hat{c}_{\mathbf{R} l \sigma}^{(\dagger)}. \quad (2.20)$$

One potential simplification to consider here is neglecting orbital overlap of neighboring sites, pairing up the operators at sites  $\mathbf{0}$  and  $\mathbf{R}$ . This eliminates the  $\mathbf{k}$ -point dependence of the Coulomb operator and thus

$$U_{lmm'l'} \equiv U_{lmm'l'}(\mathbf{0}, \mathbf{0}, \mathbf{0}), \quad \text{and} \quad (2.21a)$$

$$V_{lmm'l'}^q \equiv \sum_{\mathbf{R} \neq 0} e^{iq\mathbf{R}} U_{lmm'l'}(\mathbf{R}, \mathbf{R}, 0), \quad (2.21b)$$

corresponding to a purely local interaction  $U_{lmm'l'}$  and a purely non-local interaction  $V_{lmm'l'}^q$ . In this case the exchange symmetry of the incoming and outgoing electron reduces to  $U_{lmm'l'} = U_{mll'm'}$  and  $V_{lmm'l'}^q = V_{mll'm'}^q$ .

### 2.5.2 More symmetries, assumptions and the Kanamori-Hamiltonian

cRPA is a framework in which all interaction combinations for  $U_{lmm'l'}(\mathbf{R}_1, \mathbf{R}_2, \mathbf{R}_3, \mathbf{R}_4)$  can be computed, however there are certain symmetries and assumptions that help reduce the amount of individual elements of  $U_{lmm'l'}(\mathbf{R}_1, \mathbf{R}_2, \mathbf{R}_3, \mathbf{R}_4)$  drastically. Similar simplifications can be made for the kinetic term in Eq. (2.14). Previously, it was stated that due to the localized nature of Wannier orbitals, the Hopping amplitudes reduce (rapidly) in magnitude the further the orbitals are located in real space due to reduced orbital overlap. The decay of  $t_{mm'}(\mathbf{R}, \mathbf{R}')$  is roughly proportional to  $|\mathbf{R} - \mathbf{R}'|^{-1}$ . Hence for practical calculations, a very good approximation can be achieved by considering only the three closest (in distance) hopping terms: nearest ( $t$ ), next-nearest ( $t'$ ); and next-next-nearest ( $t''$ ) neighbor, see Fig. 2.3 for an illustration. Elements of  $U_{lmm'l'}(\mathbf{R}_1, \mathbf{R}_2, \mathbf{R}_3, \mathbf{R}_4)$  usually decay even faster than the hopping terms due to the integral over four orbitals in Eq. (2.15b) compared to two. Aside from this argument, further assumptions about the interaction can be made: (i) the Wannier functions respect SU(2) symmetry; (ii) the Wannier functions of the subset of orbitals preserve orbital symmetry; and (iii) the Coulomb interaction of electrons on different lattice sites is small compared to the on-site Coulomb interaction, e.g.,  $U_{lmm'l'}(\mathbf{R}, \mathbf{R}, \mathbf{R}, \mathbf{R}) \gg U_{lmm'l'}(\mathbf{R}, \mathbf{R}, \mathbf{R}, \mathbf{R}') \gg U_{lmm'l'}(\mathbf{R}, \mathbf{R}, \mathbf{R}', \mathbf{R}'')$ . Let us briefly justify these assumptions: (i) holds when spin-orbit coupling is ignored, the material is in the paramagnetic phase, and no external electromagnetic fields are applied [8]; (ii) applies to degenerate orbital subsets, like the  $t_{2g}$  and  $e_g$  orbitals in the 3d shell; and (iii) is valid as long as the Wannier functions remain localized around their respective lattice sites, which is generally true for d or f shells.

Under the assumptions (i)-(iii)  $U_{lmm'l'}(\mathbf{R}_1, \mathbf{R}_2, \mathbf{R}_3, \mathbf{R}_4)$  is constrained to a single lattice site and has only three independent entries, commonly denoted by the intra-orbital and inter-orbital interactions  $U$  and  $U'$ , respectively, and the Hund's exchange  $J$  [8, 9]. A visual representation of the effects of  $U$ ,  $U'$  and  $J$  can be found in Fig. 2.2. These quantities are given by

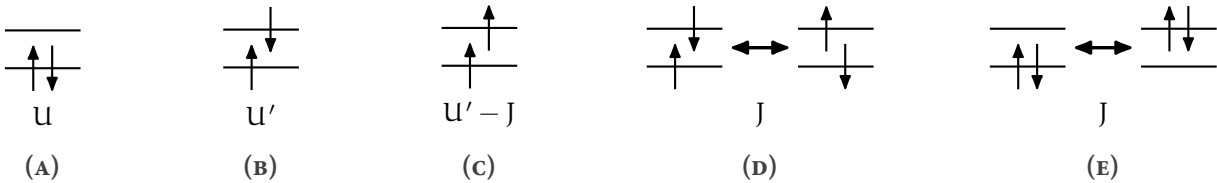


FIGURE 2.2 – Kanamori parameters  $U$ ,  $U'$  and  $J$  as described in the text:

(A) intra-orbital Coulomb interaction, (B)-(C) inter-orbital Coulomb interaction, (D) spin-flip of an electron pair and (E) pair hopping.

$$U = U_{llll} = \int d^3r \int d^3r' |w_l(\mathbf{r})|^2 \mathcal{V}_c(\mathbf{r} - \mathbf{r}') |w_l(\mathbf{r}')|^2, \quad (2.22a)$$

$$U' = U_{llmm} = \int d^3r \int d^3r' |w_l(\mathbf{r})|^2 \mathcal{V}_c(\mathbf{r} - \mathbf{r}') |w_m(\mathbf{r}')|^2 \quad \text{and} \quad (2.22b)$$



$$J = U_{lmm'l} = \int d^3r \int d^3r' w_l^*(\mathbf{r}) w_m^*(\mathbf{r}') \mathcal{V}_c(\mathbf{r} - \mathbf{r}') w_l(\mathbf{r}') w_m(\mathbf{r}), \quad (2.22c)$$

where  $\mathcal{V}_c(\mathbf{r} - \mathbf{r}')$  is the screened Coulomb interaction term. For cubic symmetry - due to constraint (ii) - there are only two independent quantities in the interaction, resulting in  $U' = U - 2J$ . With the help of these three parameters we can simplify the Hamiltonian of Eq. (2.14) and for the general case the so-called Kanamori-Hamiltonian [8, 9] reads

$$\begin{aligned} \mathcal{H}_{\text{Kanamori}} = & - \sum_{\substack{\mathbf{R}\mathbf{R}' \\ m m', \sigma}} t_{mm'}(\mathbf{R}, \mathbf{R}') \hat{c}_{\mathbf{R}m\sigma}^\dagger \hat{c}_{\mathbf{R}'m'\sigma} \\ & + U \sum_{\mathbf{R}, l} \hat{n}_{\mathbf{R}l\uparrow} \hat{n}_{\mathbf{R}l\downarrow} + \sum_{\substack{\mathbf{R}, l \neq m \\ \sigma \sigma'}} (U' - J \delta_{\sigma \sigma'}) \hat{n}_{\mathbf{R}l\sigma} \hat{n}_{\mathbf{R}m\sigma'} \\ & - J \sum_{\mathbf{R}, l \neq m} \hat{c}_{\mathbf{R}l\uparrow}^\dagger \hat{c}_{\mathbf{R}l\downarrow} \hat{c}_{\mathbf{R}m\downarrow}^\dagger \hat{c}_{\mathbf{R}m\uparrow} + J \sum_{\mathbf{R}, l \neq m} \hat{c}_{\mathbf{R}l\uparrow}^\dagger \hat{c}_{\mathbf{R}l\downarrow} \hat{c}_{\mathbf{R}m\downarrow} \hat{c}_{\mathbf{R}m\uparrow}^\dagger, \end{aligned} \quad (2.23)$$

where  $\hat{n}_{l\sigma}$  is the number operator ( $\hat{c}_{l\sigma}^\dagger \hat{c}_{l\sigma}$ ) that counts the number of electrons in orbital  $l$  with spin  $\sigma$ . The Kanamori Hamiltonian is a widely used model for strongly correlated systems and it can capture a lot of physics despite its rather crude approximations. Today, the Kanamori Hamiltonian is mostly used not only to describe spin and orbital order, including magnetically ordered phases in materials with partially filled d or f shells, but also to capture a variety of Mott-insulating states, where strong on-site electron repulsion causes electron localization.

## 2.6 The single-band Hubbard Hamiltonian

The most widely used model Hamiltonian to describe strongly correlated materials is the one-band Hubbard model. It is the single-orbital version of the Kanamori Hamiltonian and reads

$$\mathcal{H}_{\text{Hubbard}} = - \sum_{i \neq j, \sigma} t_{ij} \hat{c}_{i\sigma}^\dagger \hat{c}_{j\sigma} + U \sum_i \hat{n}_{i\uparrow} \hat{n}_{i\downarrow} - \mu \sum_i (\hat{n}_{i\uparrow} + \hat{n}_{i\downarrow}), \quad (2.24)$$

where  $i$  and  $j$  denote the lattice site in the  $N$ -dimensional lattice and the hopping is spin-independent. The interaction  $U$  is purely local and  $\mu = t_{ii}$  is the chemical potential. Due to the reduction to a single orbital, the interaction terms  $U'$  and  $J$  do not exist any more as they used to incorporate different orbitals.

This is one of the simplest forms of the most general Hubbard Hamiltonian of Eq. (2.14), however it can still not be solved exactly since the kinetic term is diagonal in momentum space whereas the interaction term is diagonal in real space. A general analytical solution to the model does therefore not exist, however recent advances allowed numerical calculations to exactly calculate the eigendecomposition of the Hubbard Hamiltonian for a couple different parameter sets. To visually illustrate the model's description, a representation of the hopping and interaction terms of Eq. (2.24) can be seen in Fig. 2.3.

The very extreme simplification of the Hubbard model is called the Hubbard Atom and it represents an isolated lattice site with either zero, one or two electrons occupying a single orbital interacting through the instantaneous electrostatic repulsion  $U$ . It is also often coined “atomic limit”, because it can be formulated as a limiting case for the Hubbard model where all hopping amplitudes are set to zero. The Hubbard Atom is analytically solvable and can already give a lot of information about



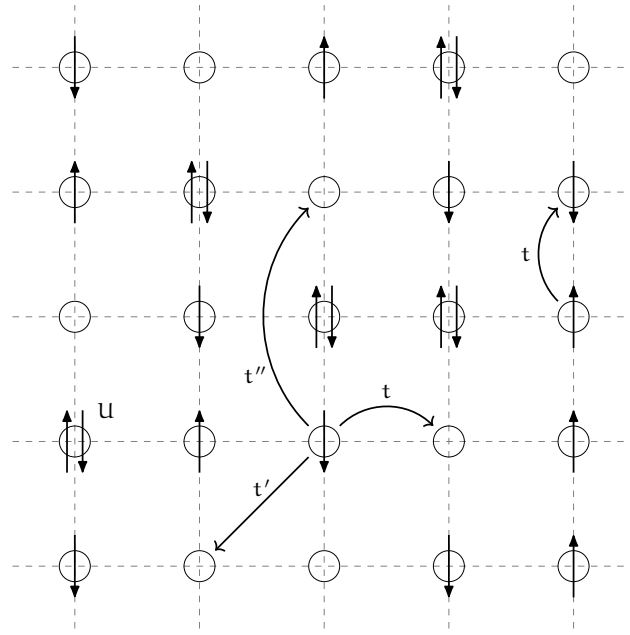


**FIGURE 2.3** – Visual representation of the two-dimensional square lattice Hubbard model. Each lattice site either contains zero, one or two electrons. Every circle represents a local orbital at any site. Here,  $t$ ,  $t'$  and  $t''$  denote nearest-neighbor hopping, next-nearest-neighbor hopping and next-next-nearest-neighbor hopping, respectively. Reasonable values for  $t$ ,  $t'$ ,  $t''$  and  $U$  are obtained from density functional theory (DFT) calculations [10] or extracted from ARPES studies [11]. For e.g., cuprates, one finds that  $t \approx 0.3\text{-}0.5$  eV,  $t' \approx -0.2t$ ,  $t'' \approx 0.1t$  and  $U \approx 8t$ .

non-perturbative processes in condensed matter physics.

In the last chapter, we looked at the fundamental Hamiltonians and a few specific models that create the theoretical foundation for modelling strongly correlated electron systems, such as transition metal oxides (e.g., manganites, cuprates or nickelates), heavy fermion systems (e.g., compounds containing rare-earth or actinide elements), Mott insulators (e.g.,  $V_2O_3$ ) and many more. We have developed the fundamental ideas required to explain the distinctive behavior of particles in systems where interactions play an important role.

With this framework in place, we now proceed to introduce the mathematical tools required to perform calculations within these models. The next chapter presents a detailed toolkit, including many-body Green's functions and diagrammatic methods, such as dynamical mean-field theory (DMFT) or the dynamical vertex approximation ( $D\Gamma A$ ). These approaches ready us to translate the abstract models into concrete results, allowing for the computation of observables and the quantitative study of strongly correlated systems. This toolkit will be essential for extracting physical insights from the models we have discussed and for bridging theory with experimental observations in the field.

## CHAPTER

## 3

QUANTUM MANY-BODY  
FRAMEWORK

This chapter is dedicated to introducing the necessary tools needed to perform realistic material calculations using dynamical mean-field theory (DMFT) or the dynamical vertex approximation D $\Gamma$ A. We start with the most central objects - the Green's functions - and subsequently assemble a complete framework which enables us to calculate a number of physical properties, e.g. the susceptibility, optical conductivity, superconductivity, pseudogap formation and more, that stem from the correlated interplay between electrons or holes.

### 3.1 One-particle Green's functions

Green's functions are fundamental tools in many-body physics, used to study the properties and behavior of interacting quantum systems. These mathematical objects encode information about the propagation of particles or excitations within a system and serve as the cornerstone for analyzing both equilibrium and nonequilibrium states. In the many-body regime, Green's functions extend beyond single-particle descriptions to include complex interactions among multiple particles. They provide insights into phenomena such as quasiparticle lifetimes, collective excitations and response functions. Specifically, one- and two-particle Green's functions describe the propagation of a single particle and the correlated motion of particle pairs, respectively. Alongside of the mathematical description of Green's function-based expressions, we also provide a pictorial description of the equations using Feynman diagrams. These Feynman diagrams allow us to easily describe interaction processes visually. Lines and vertices within the diagrams indicate particle propagators and interaction vertices, respectively. External legs will be colored gray while inner legs and interaction lines will be colored black.

In condensed matter physics, we are only interested in finite-temperature effects. Hence it is practical to use the so-called Matsubara formalism [12] in imaginary time by performing a Wick rotation  $t \rightarrow -i\tau$  [13].

Furthermore, most many-body quantities described in the following are  $n$ -point (correlation) functions<sup>[1]</sup>. These functions typically include a subset of the following parameters for each external leg: (Matsubara) frequency ( $\nu$ ), spin index ( $\sigma$ ), orbital index ( $o$ ), lattice position ( $\mathbf{R}$ ), momentum ( $\mathbf{k}$ ) or imaginary time ( $\tau$ ). This introduces a huge amount of parameters appended to a variable and can be very cumbersome to read through if explicitly written down. Therefore, to increase readability, we follow Ref. [14] and group all indices that are not explicitly written down into a compound index, e.g.  $i = \{o_i, \sigma_i, \mathbf{R}_i\}$ . If an equation containing spatial or momentum-dependent quantities is written down with a compound index, it applies equally in both real and Fourier space. Furthermore, summing over these compound indices means summing over all individual

<sup>[1]</sup> Here,  $n$  denotes the number of "connection points" of the corresponding Feynman diagram.

components they include, with a normalization of  $\frac{1}{\beta}$  for frequency sums and  $\frac{1}{N_k}$  for momentum sums, where  $\beta = \frac{1}{k_B T}$  is the inverse temperature and  $N_k$  is the total number of reciprocal lattice points.

After this short introduction, let us dive in by defining the most central quantity, the two-point (one-particle) Green's function, in a system in thermal equilibrium as

$$G_{12}^k = - \left\langle \mathcal{T} \left[ \hat{c}_{k;1} \hat{c}_{k;2}^\dagger \right] \right\rangle, \quad (3.1)$$

where  $\hat{c}_{k;i}$  ( $\hat{c}_{k;i}^\dagger$ ) are fermionic annihilation (creation) operators which annihilate (create) an electron with parameters  $i = \{\sigma_i, o_i, \tau_i\}$  and momentum  $k$  in the system.  $\langle \cdot \rangle = \frac{1}{Z} \text{Tr} \{ e^{-\beta \hat{H}} \cdot \}$  with  $Z = \text{Tr} \{ e^{-\beta \hat{H}} \}$  describes the thermal expectation value. Note, that the time evolution operator  $e^{i\hat{H}t} = e^{\hat{H}\tau}$  is real after performing the Wick rotation to imaginary time and the Boltzmann weight  $e^{\beta \hat{H}}$  describes nothing more than an additional evolution in imaginary time. Lastly,  $\mathcal{T}[\cdot]$  is the imaginary time ordering operator, where

$$\mathcal{T} \left[ \hat{c}_1^{(\dagger)}(\tau_1) \hat{c}_2^{(\dagger)}(\tau_2) \right] = \Theta(\tau_1 - \tau_2) \hat{c}_1^{(\dagger)}(\tau_1) \hat{c}_2^{(\dagger)}(\tau_2) - \Theta(\tau_2 - \tau_1) \hat{c}_2^{(\dagger)}(\tau_2) \hat{c}_1^{(\dagger)}(\tau_1). \quad (3.2)$$

The Green's function measures the probability amplitude of a propagation process and reads as a Feynman diagram

$$G_{12} = \begin{array}{c} 1 \qquad \qquad \qquad 2 \\ \bullet \longrightarrow \bullet \end{array}.$$

**FIGURE 3.1** – Diagrammatic representation of the one-particle Green's function  $G_{12}$ . The electron is annihilated at 1, propagates in imaginary time from  $\tau_1$  to  $\tau_2$  and is created at 2.

In homogeneous systems, e.g., infinite or translationally invariant systems, the Green's function inherits the system's properties and becomes invariant under spatial translations. This means that  $G_{12}(\mathbf{R}_1, \mathbf{R}_2) = G_{12}(\mathbf{R}_1 - \mathbf{R}_2, \mathbf{0}) = G_{12}(\mathbf{R})$ . In Fourier space, this means that the Green's function is also only dependent on a single momentum parameter,  $G_{12}(\mathbf{k}_1, \mathbf{k}_2) = G_{12}(\mathbf{k}_1 - \mathbf{k}_2, \mathbf{0}) = G_{12}(\mathbf{k})$ . Furthermore, if the system is stationary, i.e., the Hamiltonian is not explicitly dependent on imaginary time, then  $G_{12}(\tau_1, \tau_2) = G_{12}(\tau_1 - \tau_2, 0) = G_{12}(\tau)$ . In absence of spin-orbit coupling, the spins at 1 and 2 need to be equal and therefore  $G_{12}$  only depends on a single spin component. Additionally, the *fermionic* Green's function can be shown to be anti-periodic in imaginary time with a period of  $\beta$ <sup>[2]</sup>,

$$G_{12}(\tau) = -G_{12}(\beta - \tau) \quad \text{for } \tau > 0 \quad \text{and} \quad (3.3a)$$

$$G_{12}(\tau) = -G_{12}(\beta + \tau) \quad \text{for } \tau < 0. \quad (3.3b)$$

This anti-periodicity in time leads to the Fourier transform to be defined over a discrete set of imaginary frequencies, the so-called Matsubara frequencies, which for fermionic quantities are given by  $\nu_n = (2n + 1) \frac{\pi}{\beta}$ . In contrast, *bosonic* Green's functions are periodic in imaginary time with period  $\beta$  and therefore the Fourier transform includes the set of bosonic Matsubara frequencies

<sup>[2]</sup>This originates from the Boltzmann term  $e^{\beta \hat{H}}$  in the thermal expectation value and restricts the imaginary time domain to  $\tau \in [-\beta, \beta)$ .

$\omega_n = (2n)\frac{\pi}{\beta}$ . In the following, we will always denote fermionic Matsubara frequencies with  $\nu_n$  and bosonic ones with  $\omega_n$ . The fermionic- and bosonic-like Fourier transforms of  $G_{12}(\tau)$  become, respectively,

$$G_{12}(i\nu_n) = \int_0^\beta d\tau G_{12}(\tau) e^{i\nu_n \tau} \quad \text{and} \quad G_{12}(i\omega_n) = \int_0^\beta d\tau G_{12}(\tau) e^{i\omega_n \tau} \quad (3.4)$$

and only require the knowledge of Green's functions for positive imaginary times  $\tau$ . The inverse Fourier transforms are given by

$$G_{12}(\tau) = \frac{1}{\beta} \sum_n G_{12}(i\nu_n) e^{-i\nu_n \tau} \quad \text{and} \quad G_{12}(\tau) = \frac{1}{\beta} \sum_n G_{12}(i\omega_n) e^{-i\omega_n \tau}. \quad (3.5)$$

If we perform a spectral representation of the fermionic Green's function in Eq. (3.1) and calculate the discrete Fourier transform, we find that

$$G_{12}(i\nu_n) = \frac{1}{Z} \sum_{mn} (e^{-\beta E_n} + e^{-\beta E_m}) \frac{\langle n | \hat{c}_1 | m \rangle \langle m | \hat{c}_2^\dagger | n \rangle}{i\nu - (E_m - E_n)}. \quad (3.6)$$

If we take  $1 \equiv 2$ , which corresponds to the *local* Green's function, we can introduce the spectral function

$$A_1(\nu) = \frac{1}{Z} \sum_{mn} e^{-\beta E_n} (1 + e^{-\beta \nu}) |\langle n | \hat{c}_1 | m \rangle|^2 \delta(\nu - E_m - E_n), \quad (3.7)$$

where

$$G_1(i\nu_n) = \int_{\mathbb{R}} d\nu \frac{A_1(\nu)}{i\nu_n - \nu}. \quad (3.8)$$

The spectral function  $A_1(\nu)$  is the probability of adding or removing a particle with momentum  $\mathbf{k}_1$  with spin  $\sigma_1$  from the system. For that reason,  $A_1(\nu)$  is coined the single-particle local density of states. Furthermore, since it represents a probability distribution, the integral over all energies of  $A_1(\nu)$  is equal to 1. It is directly measurable using techniques like angle-resolved photoemission spectroscopy (ARPES) [15, 16], which probes electronic states in the material and reveals electronic structure properties, such as band gaps and quasiparticle dispersions. The peaks in  $A_1(\nu)$  correspond to quasiparticle states, with their position indicating the energy of these states and their width related to the lifetime or decay rate of the quasiparticles. A narrow peak indicates a well-defined quasiparticle with a long lifetime and weak decay rate, while a broad peak suggests the contrary. The spectral function is a key quantity in many-body theory as it connects real-world experimental results to the Green's function formalism, as is shown in Refs. [15, 16] and the following. By performing analytic continuation in the upper complex plane ( $i\nu \rightarrow \nu + i0^+$ ), one can define the retarded Green's function as

$$G_1^R(\nu) = \int_{\mathbb{R}} d\nu' \frac{A_1(\nu')}{\nu - \nu' + i0^+}, \quad (3.9)$$

from where one obtains through the Kramers-Kronig relations

$$A_1(\nu) = -\frac{1}{\pi} \Im G_1^R(\nu). \quad (3.10)$$

Thus, the spectral function is directly coupled to the imaginary part of the retarded Green's function, connecting many-body theory with physical experiments.

As an example, which will prove itself useful for the future, let us consider non-interacting electrons in a system with translational symmetry that are described by the (Wannier-) Hamiltonian

$$\hat{\mathcal{H}}_0 = \sum_{\mathbf{k};12} \varepsilon_{12}(\mathbf{k}) \hat{c}_{\mathbf{k};1}^\dagger \hat{c}_{\mathbf{k};2}, \quad (3.11)$$

where  $\varepsilon_{12}(\mathbf{k}) = - \sum_{\mathbf{R};12} t_{12}(\mathbf{R}) e^{i\mathbf{k}\mathbf{R}}$  is the momentum dispersion of the band and is measured with respect to the chemical potential  $\mu$ . In this case, it is easy to show, that

$$G_{0;12}(\nu, \mathbf{k}) = [i\nu\delta_{12} - \varepsilon_{12}(\mathbf{k})]^{-1}. \quad (3.12)$$

For the one-particle spectral function, we find in this case

$$A_{12}(\varepsilon, \mathbf{k}) = \delta(\varepsilon - \varepsilon_{\mathbf{k};12}), \quad (3.13)$$

corresponding to stable quasiparticles, due to zero width of the quasiparticle peak of  $A_{12}(\varepsilon, \mathbf{k})$ .

The direct computation of the Green's function as expressed in Eq. (3.1) generally incurs an exponential increase in cost with lattice size for interacting models. As a result, it is common practice to begin with the noninteracting case and construct a perturbative expansion in terms of the interaction around it. In this context, we will start with the non-interacting case described above. This perturbation expansion will not be derived in detail in this thesis, as there are many wonderful resources that explain it very thoroughly [17, 18], thus we will only sketch it here. In essence, the expansion is constructed using the so-called S-matrix and employs strategies such as the Wick contraction [13, 19, 20] and the linked cluster theorem [21]. The expansion begins by identifying the most general interaction part of the Hamiltonian of Eq. (2.14),

$$\hat{\mathcal{H}}_I = \frac{1}{2} \sum_{1234} U_{1234} \hat{c}_1^\dagger \hat{c}_3^\dagger \hat{c}_4 \hat{c}_2. \quad (3.14)$$

The expansion of the Green's function then reads

$$G_{12}(\tau) = - \frac{1}{\langle S(\beta) \rangle_0} \sum_{n=0}^{\infty} \frac{(-1)^n}{n!} \int_0^\beta d\tau_1 \cdots \int_0^\beta d\tau_n \langle \mathcal{T} [\hat{c}_1 \hat{c}_2^\dagger \hat{\mathcal{H}}_I(\tau_1) \cdots \hat{\mathcal{H}}_I(\tau_n)] \rangle_0, \quad (3.15)$$

where  $S(\beta)$  is the abovementioned S-matrix and  $\langle \cdot \rangle_0$  is the thermal expectation value in terms of the non-interacting Hamiltonian  $\hat{\mathcal{H}}_0$ . In Feynman diagram jargon, this contains all diagrams that are possible, also disconnected ones<sup>[3]</sup>. The linked cluster theorem allows us to get rid of those disconnected contributions by effectively canceling with the  $\frac{1}{\langle S(\beta) \rangle_0}$  term in front. This results in

$$G_{12}(\tau) = - \sum_{n=0}^{\infty} \frac{(-1)^n}{n!} \int_0^\beta d\tau_1 \cdots \int_0^\beta d\tau_n \langle \mathcal{T} [\hat{c}_1 \hat{c}_2^\dagger \hat{\mathcal{H}}_I(\tau_1) \cdots \hat{\mathcal{H}}_I(\tau_n)] \rangle_0^{\text{conn}}, \quad (3.16)$$

where  $\langle \cdot \rangle_0^{\text{conn}}$  now indicates that we only consider connected diagrams in the expansion. We can transform this into a diagrammatic representation by applying Wick contractions, which allow us

<sup>[3]</sup>Disconnected means, that the term includes a diagram that consists of two separate, disconnected diagrams.

to collect pairs of creation and annihilation operators to form independent expectation values. In the case of the  $n = 1$  term in the perturbation expansion of the Green's function,

$$G_{1;12}(\tau) = \sum_{abcd} \int_0^\beta d\tau_1 U_{abcd} \times \left[ -\langle \mathcal{T} [\hat{c}_1(\tau) \hat{c}_a^\dagger(\tau_1)] \rangle_0 \langle \mathcal{T} [\hat{c}_b(\tau_1) \hat{c}_c^\dagger(\tau_1)] \rangle_0 \langle \mathcal{T} [\hat{c}_d(\tau_1) \hat{c}_2^\dagger(0)] \rangle_0 \right. \\ \left. + \langle \mathcal{T} [\hat{c}_1(\tau) \hat{c}_a^\dagger(\tau_1)] \rangle_0 \langle \mathcal{T} [\hat{c}_b(\tau_1) \hat{c}_c^\dagger(\tau_1)] \rangle_0 \langle \mathcal{T} [\hat{c}_d(\tau_1) \hat{c}_2^\dagger(0)] \rangle_0 \right]. \quad (3.17)$$

The remaining expectation values are nothing more than minus the non-interacting Green's function of Eq. (3.12). Written in Feynman diagrams, the first relevant perturbation expansion term is shown in Fig. 3.2.

$$G_{1;12}(\tau) = \frac{1}{\tau} \rightarrow \frac{a}{\tau_1} \frac{b}{\tau_1} \rightarrow \frac{2}{0} + \frac{1}{\tau} \rightarrow \frac{a}{\tau_1} \frac{b}{\tau_1} \frac{c}{\tau_1} \frac{d}{\tau_1} \rightarrow \frac{1}{0}$$

FIGURE 3.2 – First order diagrams for the single-particle Green's function. The corresponding diagrams are coined the Hartree- and the Fock-term, respectively. As the name suggests, taking only these two diagrams as the whole perturbation expansion leads to the Hartree-Fock approximation, formulated as a diagrammatic theory.

## 3.2 Self-energy

The one-particle Green's function perturbative expansion is already much simplified in the graphical portrayal. However, the number of diagrams increases exponentially with order  $n$ <sup>[4]</sup>. Therefore, the Feynman diagram approach would be of little practical use if the only way to progress was to calculate each diagram one at a time. However, in reality the technique is actually quite useful, since it hints on how to sum up the perturbative series. Let us talk about how it applies to Green's function for single particles. First, let us define another compound index which will further levitate readability. We will set  $k = \{\nu, \mathbf{k}\}$  and  $q = \{\omega, \mathbf{q}\}$  as a compound index including momentum and frequency in one index for fermionic ( $k$ ) and bosonic ( $q$ ) frequencies and momenta. Note, that if we write  $\nu$  instead of  $k$ , we refer to the *local* part of the quantity with no momentum dependence instead of the *non-local* part.

Diagrams in general can be split up into two classes: (i) diagrams that, by cutting a single internal Green's function line, transform in two lower-order diagrams, which are called one-particle reducible and (ii) diagrams that are not one-particle reducible, which are called one-particle irreducible (1PI). Let us define as the one-particle self-energy  $\Sigma_{12}^k$  the sum of all irreducible diagrams without external

<sup>[4]</sup> For  $n = 2$  there exist 10 diagrams, for  $n = 7$  the number of diagrams is well over a million.

legs. For example, the black part of the diagrams in Fig. 3.2 corresponds to the first-order diagrams of the self-energy. It is then straightforward to rewrite Eq. (3.16) in terms of the self-energy, yielding

$$G_{12}^k = G_{0,12}^k + \sum_{ab} G_{0,1a}^k \Sigma_{ab}^k G_{b2}^k, \quad (3.18)$$

which results in - when taking Eq. (3.12) as the noninteracting Green's function and inverting in frequency and momentum space - a way to express the full (interacting) single-particle Green's function in terms of the self-energy

$$G_{12}^k = \left[ i\nu_n \delta_{12} - \varepsilon_{12}(\mathbf{k}) - \Sigma_{12}^k \right]^{-1}. \quad (3.19)$$

Eq. (3.18) is commonly known as the Dyson equation for the single-particle Green's function and for completeness, its diagrammatic representation can be found in Fig. 3.3. It is a geometric series, where each term in the sum subsequently adds irreducible diagrams that are pieced together by non-interacting Green's functions to generate all possible diagrams. The self-energy can be obtained

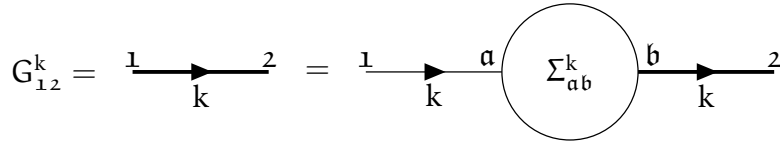


**FIGURE 3.3** – Diagrammatic representation of Eq. (3.18). The full Green's function  $G_{12}^k$  is drawn as a thick black line.

by simply inverting Eq. (3.18),

$$\Sigma_{12}^k = (G_{0,12}^k)^{-1} - (G_{12}^k)^{-1}. \quad (3.20)$$

Thus, perturbation theory can be done in two distinct ways: the simpler approach is to determine the Green's function directly, for example, up to order  $n$ , where the second method is to compute the self-energy up to order  $n$  and insert its expression in the Dyson equation Eq. (3.18). This gives an approximate Green's function containing each order of perturbation theory with only a subset of all possible diagrams. As a result, Eq. (3.18) represents a way to sum up perturbation theory and is actually more relevant from a physical standpoint. Indeed, many methods leverage the usefulness of this approach, for example the dynamical mean-field theory or the dynamical vertex approximation, as we will see later.

Let us add some physical background to the self-energy in the following.  $\Sigma$  represents the effects of the interaction on the single electron propagators. The real and imaginary part of the self-energy have significant impact on the physical properties of the system. The real part of the self-energy contributes to an energy shift of the electronic states of the single-particle energy levels  $\varepsilon(\mathbf{k})$  due to interactions. In contrast, the imaginary part of the self-energy is related to the decay or lifetime of quasiparticles and introduces a spectral broadening or damping of the electronic states, indicating how long an excitation or quasiparticle persists before interacting with other excitations or scattering events. A larger imaginary part implies a shorter lifetime and stronger interactions. The first order derivative in frequency,  $\frac{\partial \Sigma^k}{\partial \nu}$ , contributes to an effective renormalization of the bare electron mass. It also leads to a redistribution of spectral weight in the one-particle spectral function, which provides information about the distribution of energy levels available for excitations. A broader spectral function, whose broadening is controlled by the imaginary part of the self-energy, typically indicates stronger interactions and a more correlated system.



### 3.3 Two-particle Green's functions

In analogy to the one-particle Green's function, the two-particle Green's function describes the amplitude of the propagation of two particles, two holes or a particle and a hole. A similar expression to Eq. (3.1) can be formulated for the two-particle Green's function

$$G_{1234}^{qkk'} = - \left\langle \mathcal{T} \left[ \hat{c}_{\mathbf{k},1} \hat{c}_{\mathbf{k}-\mathbf{q};2}^\dagger \hat{c}_{\mathbf{k}'-\mathbf{q};3} \hat{c}_{\mathbf{k}',4}^\dagger \right] \right\rangle. \quad (3.21)$$

It describes two particles, two holes or a particle and a hole being inserted in the system at times  $\tau_2$  and  $\tau_4$ , propagating in the system until they are removed again at  $\tau_1$  and  $\tau_3$ , respectively. Assuming a stationary Hamiltonian that satisfies time-translation invariance, it is possible to eliminate one imaginary time variable by setting it zero. Then, the Green's function only depends on three time variables and through Fourier transform, also only depends on three frequency and momentum variables. Furthermore, similar to the case for the one-particle Green's function, the absence of spin-orbit coupling reduces the number of spin degrees of freedom

$$G_{\sigma\sigma';1234}^{qkk'} = G_{\sigma\sigma\sigma'\sigma';1234}^{qkk'} \quad \text{and} \quad (3.22a)$$

$$G_{\sigma\sigma';1234}^{qkk'} = G_{\sigma\sigma'\sigma'\sigma;1234}^{qkk'}. \quad (3.22b)$$

In this case, the total incoming and outgoing spin must be equal and this puts a heavy constraint on the possible spin combinations,

$$\sigma_1 = \sigma_2 = \sigma_3 = \sigma_4, \quad (\sigma_1 = \sigma_2) \neq (\sigma_3 = \sigma_4) \quad \text{and} \quad (\sigma_1 = \sigma_4) \neq (\sigma_2 = \sigma_3), \quad (3.23)$$

totaling to only six unique spin combinations, each of which can be seen in Fig. 3.4. Furthermore, if

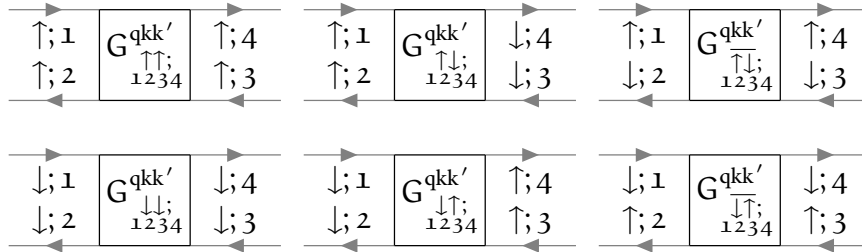


FIGURE 3.4 – In the case of absent spin-orbit coupling, these are the only non-vanishing spin combinations of the two-particle Green's function.

one describes quantities in the paramagnetic phase, where the system is SU(2)-symmetric, there are only two independent spin configurations,

$$G_{\sigma\sigma';1234}^{qkk'} = G_{(-\sigma)(-\sigma');1234}^{qkk'} = G_{\sigma'\sigma;1234}^{qkk'} \quad \text{and} \quad (3.24a)$$

$$G_{\sigma\sigma;1234}^{qkk'} = G_{\sigma(-\sigma);1234}^{qkk'} + G_{\sigma(-\sigma);1234}^{qkk'}. \quad (3.24b)$$

For these two spin combinations, the (d)ensity, (m)agnetic, (s)inglet and (t)riplet channel<sup>[5]</sup> specified in the following are a particularly helpful choice of notation, as we shall see in the upcoming sections:

$$G_{d;1234}^{qkk'} = G_{\uparrow\uparrow;1234}^{qkk'} + G_{\uparrow\downarrow;1234}^{qkk'}, \quad (3.25a)$$

<sup>[5]</sup>As we will see later, in ph/ph-notation, the Bethe-Salpeter equation will become diagonal for the d/m spin combination as well as for pp-notation in the s/t spin combination.



$$G_{m;1234}^{qkk'} = G_{\uparrow\uparrow;1234}^{qkk'} - G_{\uparrow\downarrow;1234}^{qkk'} = G_{\uparrow\downarrow;1234}^{qkk'}, \quad (3.25b)$$

$$G_{s;1234}^{qkk'} = G_{\uparrow\downarrow;1234}^{qkk'} - G_{\uparrow\uparrow;1234}^{qkk'} \quad \text{and} \quad (3.25c)$$

$$G_{t;1234}^{qkk'} = G_{\uparrow\downarrow;1234}^{qkk'} + G_{\uparrow\uparrow;1234}^{qkk'}. \quad (3.25d)$$

Besides the spin-symmetries discussed above, the Green's function also inherits other properties of the system, such as time-reversal symmetry, which manifests itself by

$$G_{1234}^{qkk'} = G_{4321}^{\bar{q}\bar{k}'\bar{k}}, \quad (3.26)$$

where  $\bar{k} = \{\nu, -\mathbf{k}\}$  is the time-reversed compound momentum variable. Furthermore, the two-particle Green's function satisfies the crossing symmetry, which is a direct manifestation of Pauli's principle. Crossing symmetry refers to the antisymmetric property of the Green's function with respect to the exchange of the incoming and outgoing fermions

$$G_{\sigma\sigma';1234}^{qkk'} = -G_{\sigma'\sigma;3214}^{(k'-k)(k'-q)k'} \quad (3.27a)$$

$$= -G_{\sigma\sigma';1432}^{(k-k')k(k-q)} \quad (3.27b)$$

$$= G_{\sigma'\sigma;3412}^{(-q)(k'-q)(k-q)}. \quad (3.27c)$$

The symmetries Eq. (3.27a) - Eq. (3.27c) describe the frequency changes that occur by exchanging the positions of the gray fermion lines, leaving the vertex unchanged. The last line corresponds to a full swap of the incoming and outgoing particle labels. The crossing symmetry is visually shown in Fig. 3.5. Lastly, the Green's function also possesses symmetry with respect to complex conjugation,

$$\left(G_{\sigma\sigma';1234}^{qkk'}\right)^* = G_{\sigma'\sigma;4321}^{(-q)(-k)(-k')}. \quad (3.28)$$

At the beginning of the section it was stated that the (four-point) two-particle Green's function

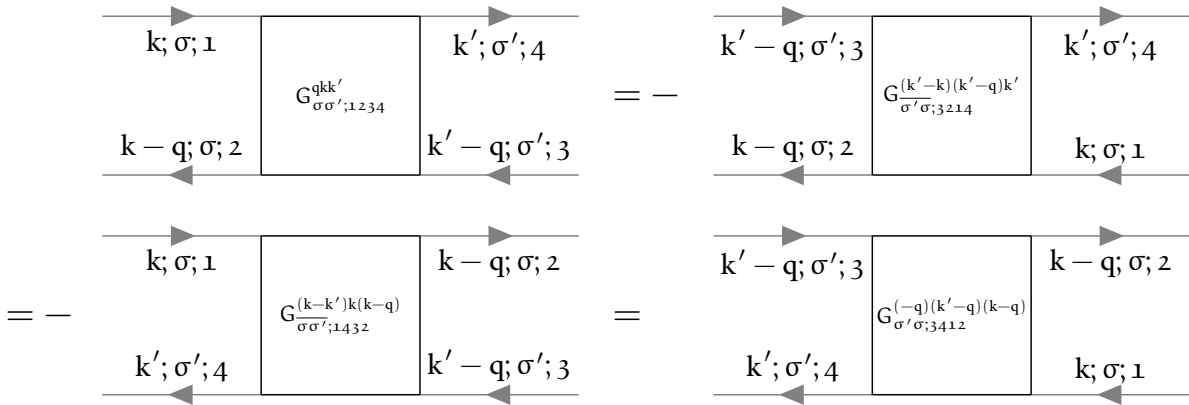


FIGURE 3.5 – Diagrammatic representation of the crossing symmetry relations in order of Eq. (3.27a) - Eq. (3.27c).

only requires three frequency arguments to be fixed since the last one is automatically given by momentum conservation. There are three equivalent choices (coined channels) of independent frequencies (with  $\nu$ ,  $\nu'$  being a fermionic and  $\omega$  a bosonic Matsubara frequency)

$$\text{ph-notation: } \{\nu_1 = \nu, \quad \nu_2 = \nu - \omega, \quad \nu_3 = \nu' - \omega, \quad \nu_4 = \nu'\}, \quad (3.29a)$$

$$\overline{\text{ph}}\text{-notation: } \{\nu_1 = \nu, \quad \nu_2 = \nu', \quad \nu_3 = \nu' - \omega, \quad \nu_4 = \nu - \omega\} \quad \text{and} \quad (3.29b)$$

$$\text{pp-notation: } \{\nu_1 = \nu, \quad \nu_2 = \omega - \nu', \quad \nu_3 = \omega - \nu, \quad \nu_4 = \nu'\}. \quad (3.29c)$$

To show the effects of this frequency shift and how they affect the labels of the diagrams, we show the two-particle Green's function in the three notations of Eq. (3.29a) - Eq. (3.29c) in Fig. 3.6 below. Obviously, the choice of frequency convention should not have any impact on the physical content

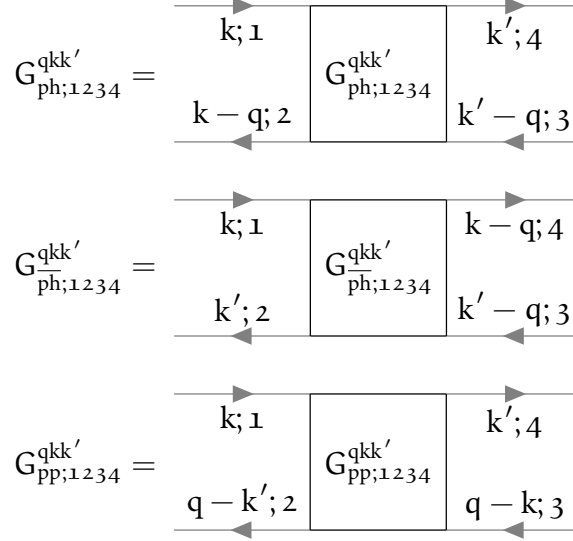


FIGURE 3.6 – Two-particle Green's functions in the different frequency notations of Eq. (3.29a) - Eq. (3.29c) expressed in Feynman diagrams. The frequency notation is encoded in an additional subscript, {ph,  $\overline{\text{ph}}$ , pp}.

of the Green's function, hence it is possible to switch between these channels by applying channel-specific frequency shifts [22],

$$G^{qkk'}_{\text{ph};1234} = G^{(k-k')(k-q)}_{\overline{\text{ph}};1234}, \quad (3.30a)$$

$$G^{qkk'}_{\overline{\text{ph}};1234} = G^{(k-k')(k-q)}_{\text{ph};1234}, \quad (3.30b)$$

$$G^{qkk'}_{\text{ph};1234} = G^{(k+k'-q)kk'}_{\text{pp};1234} \quad \text{and} \quad (3.30c)$$

$$G^{qkk'}_{\text{pp};1234} = G^{(k+k'-q)kk'}_{\text{ph};1234}. \quad (3.30d)$$

Let us finally note that the two-particle Green's function represents all diagrams that are possible that involve two electrons, two holes or an electron and a hole. It can therefore be split into two parts: (i) a part, where the electrons do not interact with each other and propagate independently; and (ii) a part, where the electrons do interact with each other through an infinite number of processes. (ii) is commonly called the connected two-particle Green's function and can be mathematically formulated by

$$G^{qkk'}_{\sigma\sigma';1234} = G^{\text{conn};qkk'}_{\sigma\sigma';1234} + \delta_{q0} G^k_{\sigma;12} G^{k'}_{\sigma';34} - \delta_{\sigma\sigma'} \delta_{kk'} G^k_{\sigma;14} G^{k-q}_{\sigma;32}. \quad (3.31)$$

Diagrammatically, the connected two-particle Green's function contains all diagrams, where two propagating electrons interact with each other. The first terms up to interaction order two are given in Fig. 3.7. The other terms in Eq. (3.31) are not that interesting, they merely describe the electrons

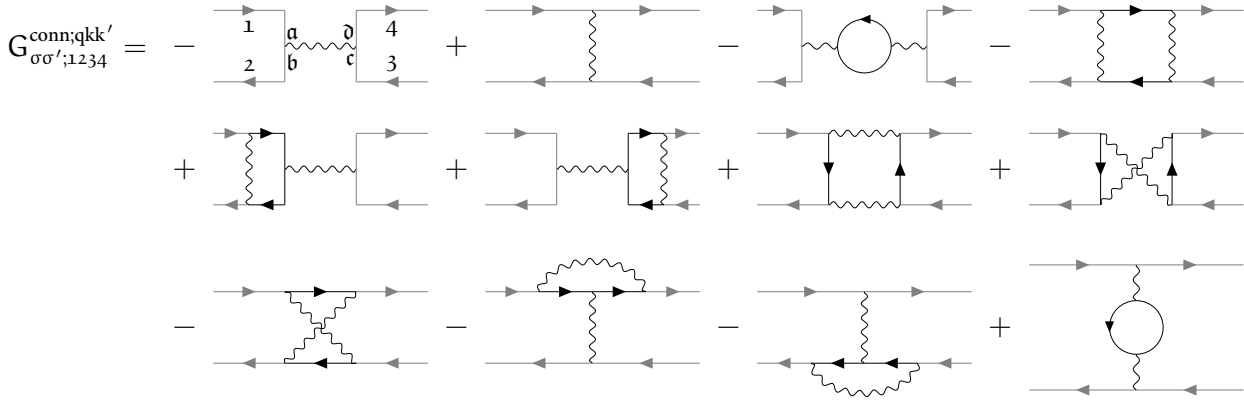


**FIGURE 3.7** – Diagrammatic representation of the two-particle connected Green's function up to order two. It includes the possible interaction processes that occur between two propagating electrons. The particle labels are only written down for the first diagram, the other diagrams are labeled analogously.

$$\delta_{q0} G_{\sigma;12}^k G_{\sigma';34}^{k'} - \delta_{\sigma\sigma'} \delta_{kk'} G_{\sigma;14}^k G_{\sigma';32}^{k-q} = \begin{array}{c|c} 1 & 4 \\ \hline \downarrow & \uparrow \\ 2 & 3 \end{array} \delta_{q0} - \begin{array}{c|c} 1 & 4 \\ \hline \delta_{\sigma\sigma'} \delta_{kk'} & \\ 2 & 3 \end{array}$$

**FIGURE 3.8** – Disconnected part (second and third term on the right hand side of Eq. (3.31)) of the two-particle Green's function.

propagating in the system without ever interacting with the other. However, we will still show the diagrammatic content of the second and third term of Eq. (3.31) in Fig. 3.8. The connected two-particle Green's function without the external legs is commonly called the full vertex  $F$ , where by convention an additional minus sign is introduced,

$$G_{1234}^{conn;qkk'} = -\frac{1}{\beta} \sum_{abc d} G_{1a}^k G_{b2}^{k-q} F_{abc d}^{qkk'} G_{3c}^{k'-q} G_{d4}^{k'}. \quad (3.32)$$

By the previous definition, the vertex function  $F_{1234}^{qkk'}$  contains all diagrams that connect two incoming and two outgoing lines. All diagrams contained in the full vertex  $F_{1234}^{qkk'}$  can be classified by their two-particle reducibility (2PR). A diagram is called two-particle reducible, if it can be split into two separate parts by cutting two internal Green's function lines. Furthermore, this classification is described by three channels,  $\{\text{ph}, \overline{\text{ph}}, \text{pp}\}$ <sup>[6]</sup>, depending on which incoming and outgoing lines are being separated by this “cutting”-process. The ph-channel corresponds to those diagrams, where the sub-parts connect 12 and 34, for the  $\overline{\text{ph}}$ -channel 14 and 23 and for the pp-channel 13 and 24 are connected. These reducible diagrams are categorized in  $\Phi_{\text{ph};1234}^{qkk'}$ ,  $\Phi_{\overline{\text{ph}};1234}^{qkk'}$  and  $\Phi_{\text{pp};1234}^{qkk'}$ , respectively.

<sup>[6]</sup>The attentive reader remembers that there are also three (identically-named) frequency notations that were mentioned previously. The channel reducibility and frequency notation are - in general - detached. From now on, if only one subscript  $r \in \{\text{ph}, \overline{\text{ph}}, \text{pp}\}$  is given per vertex quantity, it means that the channel reducibility will belong to  $r$  and the frequency notation will be ph-like. Otherwise, the channel reducibility and frequency notation will be denoted in the sub- and superscript of the variable separately. This will be relevant later when discussing the Bethe-Salpeter equation (BSE), see Sec. 3.5. The BSE is only diagonal in the bosonic transfer momentum and frequency  $q$  if the channel reducibility is the same as the frequency notation.

All diagrams that are not two-particle reducible are grouped together in the quantity  $\Lambda_{1234}^{qkk'}$ . This procedure is called the parquet decomposition and reads mathematically

$$F_{1234}^{qkk'} = \Lambda_{1234}^{qkk'} + \Phi_{ph;1234}^{qkk'} + \Phi_{\overline{ph};1234}^{qkk'} + \Phi_{pp;1234}^{qkk'}. \quad (3.33)$$

Another possibility is to split up the full vertex  $F$  in reducible and irreducible diagrams in a specific channel  $r \in \{ph, \overline{ph}, pp\}$ ,

$$F_{1234}^{qkk'} = \Gamma_{r;1234}^{qkk'} + \Phi_{r;1234}^{qkk'}, \quad (3.34)$$

where  $\Gamma_{r;1234}^{qkk'}$  is the irreducible vertex in channel  $r$  and  $\Phi_{r;1234}^{qkk'}$  the corresponding reducible one. Note, that in channel  $r$  irreducible diagrams might still be reducible in another channel  $r' \neq r$ . For example,  $\Gamma_{ph;1234}^{qkk'}$  contains all fully irreducible diagrams, but also all diagrams which are reducible in channels  $\overline{ph}$  and  $pp$ ,

$$\Gamma_{ph;1234}^{qkk'} = \Lambda_{1234}^{qkk'} + \Phi_{\overline{ph};1234}^{qkk'} + \Phi_{pp;1234}^{qkk'}. \quad (3.35)$$

This will be important later in Sec. 3.5, where we will discuss the Bethe-Salpeter equations. Furthermore, the following relations for the  $ph$  and  $\overline{ph}$  channel for  $\Gamma_{r;1234}^{qkk'}$  and  $\Phi_{r;1234}^{qkk'}$  hold:

$$\Phi_{ph;1234;\sigma\sigma'}^{qkk'} = -\Phi_{ph;3214;\sigma'\sigma}^{(k'-k)(k'-q)k'}, \quad (3.36a)$$

$$= -\Phi_{ph;1432;\sigma'\sigma}^{(k-k')k(k-q)}. \quad (3.36b)$$

From this one can construct the density and magnetic contributions to  $\Phi_{ph;1234;\sigma\sigma'}^{qkk'}$  in terms of  $\Phi_{ph;1234;\sigma\sigma'}^{qkk'}$

$$\Phi_{d;ph;1234}^{qkk'} = -\frac{1}{2}\Phi_{d;ph;3214}^{(k'-k)(k'-q)k'} - \frac{3}{2}\Phi_{m;ph;3214}^{(k'-k)(k'-q)k'} \quad (3.37a)$$

$$\Phi_{m;ph;1234}^{qkk'} = -\frac{1}{2}\Phi_{d;ph;3214}^{(k'-k)(k'-q)k'} + \frac{1}{2}\Phi_{m;ph;3214}^{(k'-k)(k'-q)k'}. \quad (3.37b)$$

The relations Eq. (3.36) and Eq. (3.37) also apply to the full- and irreducible vertices  $F_{\overline{ph};1234;\sigma\sigma'}^{qkk'}$  and  $\Gamma_{\overline{ph};1234;\sigma\sigma'}^{qkk'}$  in a similar fashion. Note that there is no connection between the  $pp$  channel and the other two channels, hence it is not possible to transform the channel reducibility from either  $ph$  or  $\overline{ph}$  to  $pp$ . The  $pp$ -channel fulfills a crossing symmetry on its own,

$$\Phi_{pp;1234;\sigma\sigma'}^{qkk'} = -\Phi_{pp;1432;\sigma\sigma'}^{(k-k')k(k-q)}. \quad (3.38)$$

As the next step, let us briefly introduce the concept of linear response and the central physical property describing the response of a system with respect to an external perturbation<sup>[7]</sup>, the susceptibility.

<sup>[7]</sup> For example an external electromagnetic field.

### 3.4 Susceptibility

Experimentally, it is not possible to directly extract information (just by “looking”) about the interactions between electrons in a system. Instead, in spectroscopic experiments, a perturbation is applied to the system and one measures the system’s response. In particular, one measures how expectation values  $\langle \cdot \rangle$  of operators (take the multi-dimensional operator  $\hat{O}_i(\tau)$  as an example) changes when an external field  $h_j(\tau)$  is applied. In linear response theory, this response is — as the name suggests — taken to be linear in the perturbing field, requiring this field to be sufficiently small in order for this description to be a good approximation [23, 24],

$$\langle \hat{O}_i(\tau) \rangle_{\mathbf{h}} - \langle \hat{O}_i(\tau) \rangle_{\mathbf{h}=0} = \int_0^\beta d\tau' \chi_{ij}(\tau - \tau') h_j(\tau') + \mathcal{O}(\mathbf{h}^2), \quad (3.39)$$

where  $\chi_{ij}(\tau - \tau')$  is coined physical susceptibility and does not depend on the field  $h_j(\tau)$ .  $\chi(\tau - \tau')$  fulfills the Kramers-Kronig relations, is causal ( $\chi_{ij}(\tau - \tau') = \Theta(\tau - \tau') \chi_{ij}(\tau - \tau')$ ) and is finite ( $\forall \tau, \tau' : \exists C \in \mathbb{R} : |\chi_{ij}(\tau - \tau')| < C$ ). The susceptibility can be computed straightforwardly by taking the functional derivative of  $\hat{O}_i(\tau)$  with respect to the field  $h_j(\tau)$ ,

$$\chi_{ij}(\tau - \tau') = \left. \frac{\delta \langle \hat{O}_i(\tau') \rangle}{\delta h_j(\tau)} \right|_{\mathbf{h}=0} = \langle \mathcal{T} \hat{O}_i(\tau) \hat{O}_j(\tau') \rangle - \langle \hat{O}_i \rangle \langle \hat{O}_j \rangle. \quad (3.40)$$

On the two-particle level, only the density’s response to variations in the one-particle energy,  $\chi_d$ , and the magnetization’s response to variation in the electromagnetic field in the same direction,  $\chi_m$ , are non-zero [23],

$$\chi_d(\tau) = \chi_{nn}(\tau) = - \left. \frac{\delta \langle \hat{n} \rangle}{\delta \mu(\tau)} \right|_{\mu=0} \quad \text{and} \quad (3.41a)$$

$$\chi_m(\tau) = \chi_{ii}(\tau) = \left. \frac{\delta \langle \hat{o}_i \rangle}{\delta h_i(\tau)} \right|_{\mathbf{h}=0}, \quad (3.41b)$$

where  $i \in \{x, y, z\}$ . The physical susceptibilities are included in the two-particle Green’s function, as we will see shortly. In fact, the sum of terms corresponding to the two disconnected, horizontal Green’s function lines and the vertex part is denoted as the generalized susceptibility and can be expressed as

$$\begin{aligned} \chi_{1234}^{\text{ph};\text{qkk}'} &= \beta \left( G_{1234}^{\text{ph};\text{qkk}'} - \delta_{q0} G_{14}^k G_{32}^{k'} \right) \\ &= -\beta \delta_{\text{kk}'} G_{14}^k G_{32}^{k-q} - \sum_{abc\bar{d}} G_{1a}^k G_{b2}^{k-q} F_{abc\bar{d}}^{\text{ph};\text{qkk}'} G_{3c}^{k'-q} G_{\bar{d}4}^{k'} \\ &= \chi_{0;1234}^{\text{qkk}'} - \frac{1}{\beta^2} \sum_{abc\bar{d}} \chi_{0;12b\bar{a}}^{\text{qkk}} F_{abc\bar{d}}^{\text{ph};\text{qkk}'} \chi_{0;\bar{d}c34}^{\text{qk}'k'}, \end{aligned} \quad (3.42)$$

where

$$\chi_{0;1234}^{\text{qkk}'} = -\beta \delta_{\text{kk}'} G_{14}^k G_{32}^{k-q} \quad (3.43)$$

is commonly denoted as the generalized bubble susceptibility<sup>[8]</sup>. From this one can obtain physical susceptibilities by contracting the inner legs, i.e.,

$$\chi_{14}^q = \sum_{kk';23} \chi_{1234}^{qkk'} \quad (3.45)$$

The diagrammatic content of the physical susceptibility is shown in Fig. 3.9 below. Similarly, the

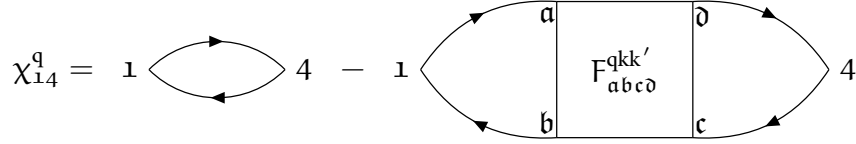


FIGURE 3.9 – The physical susceptibility is defined as the generalized susceptibility with contracted legs, see Eq. (3.45).

contracted bubble susceptibility can be written as

$$\chi_{0;14}^q = \sum_{kk';23} \chi_{0;1234}^{qkk'} \quad (3.46)$$

Analogously to Eq. (3.25a) and Eq. (3.25b), one can write down density and magnetic spin combinations of the physical susceptibility,

$$\chi_d^q = \chi_{\uparrow\uparrow}^q + \chi_{\uparrow\downarrow}^q \quad \text{and} \quad (3.47a)$$

$$\chi_m^q = \chi_{\uparrow\uparrow}^q - \chi_{\uparrow\downarrow}^q = \chi_{\uparrow\downarrow}^q. \quad (3.47b)$$

Note that expressions Eq. (3.47a) and Eq. (3.47b) are nothing more than the Fourier-transformed versions of Eq. (3.41a) and Eq. (3.41b), respectively.

### 3.5 Bethe-Salpeter equation

In the section above we have specified  $\Gamma_{r;1234}^{qkk'}$  as the fully irreducible vertex in channel  $r$  and  $\Phi_{r;1234}^{qkk'}$  as the reducible diagrams in channel  $r$ . We can now construct the full set of  $\Phi_{r;1234}^{qkk'}$  from the irreducible vertex by chaining them together with pairs of Green's functions connecting two irreducible vertices. This results in so-called ladders,

$$\begin{aligned} \Phi_{r;1234}^{qkk'} &= \sum_{k_1;abc\bar{d}} \Gamma_{r;12ab}^{qkk_1} G_{bc}^{k_1} G_{\bar{d}a}^{k_1-q} \Gamma_{r;\bar{c}d34}^{qk_1k'} \\ &+ \sum_{k_1 k_2;abc\bar{d}} \Gamma_{r;12ab}^{qkk_1} G_{bc}^{k_1} G_{\bar{d}a}^{k_1-q} \Gamma_{r;\bar{c}d\bar{e}f}^{qk_1k_2} G_{fg}^{k_2} G_{\bar{h}e}^{k_2-q} \Gamma_{r;\bar{g}h34}^{qk_2k'} + \dots \end{aligned} \quad (3.48a)$$

<sup>[8]</sup> The generalized susceptibility in the particle-particle channel reads

$$\chi_{1234;\sigma\sigma'}^{pp;qkk'} = \beta (1 - \delta_{\sigma\sigma'}) \left[ G_{1234;\sigma\sigma'}^{pp;qkk'} - \delta_{q0} G_{14}^{-k} G_{32}^{k'} \right]. \quad (3.44)$$

$$\begin{aligned}
&= -\frac{1}{\beta} \sum_{k_1; abc\bar{d}} \Gamma_{r;12ab}^{qkk_1} \chi_{0;b\bar{a}dc}^{qk_1k_1} \Gamma_{r;c\bar{d}34}^{qk_1k'} \\
&\quad + \frac{1}{\beta^2} \sum_{k_1k_2; abc\bar{d}} \Gamma_{r;12ab}^{qkk_1} \chi_{0;b\bar{a}dc}^{qk_1k_1} \Gamma_{r;c\bar{d}ef}^{qk_1k_2} \chi_{0;f\bar{e}hg}^{qk_2k_2} \Gamma_{r;g\bar{h}34}^{qk_2k'} + \dots
\end{aligned} \tag{3.48b}$$

By combining Eq. (3.34) and Eq. (3.48), one can obtain the Bethe-Salpeter equation (BSE) in all three channels [25–27],

$$F_{1234}^{qkk'} = \Gamma_{ph;1234}^{qkk'} - \frac{1}{\beta} \sum_{k_1k_2; abc\bar{d}} \Gamma_{ph;12ba}^{qkk_1} \chi_{0;abc\bar{d}}^{qk_1k_2} F_{ph;\bar{d}c34}^{qk_2k'} \tag{3.49a}$$

$$= \Gamma_{ph;1234}^{qkk'} + \frac{1}{\beta} \sum_{k_1k_2; abc\bar{d}} \Gamma_{ph;12ba}^{qkk_1} \chi_{0;abc\bar{d}}^{qk_1k_2} F_{ph;\bar{d}c34}^{qk_2k'} \tag{3.49b}$$

$$= \Gamma_{pp;1234}^{qkk'} - \frac{1}{2\beta} \sum_{k_1k_2; abc\bar{d}} \Gamma_{pp;12ba}^{qkk_1} \chi_{0;abc\bar{d}}^{qk_1k_2} F_{pp;\bar{d}c34}^{qk_2k'}, \tag{3.49c}$$

where we have expressed the full vertex  $F_{1234}^{qkk'}$  in terms of the irreducible vertex  $\Gamma_{r;1234}^{qkk'}$  and the generalized (bubble) susceptibility as a Dyson-like equation. Note that for Eq. (3.49) we used the same channel reducibility and frequency notation for each separate line. This results in a key property of the BSE: the equation becomes diagonal in the bosonic transfer momentum and frequency  $q$ . This can be taken advantage of in numerical computations as it makes it especially easy to parallelize over  $q$  as it is independent of all other quantum numbers. If we had not chosen the channel reducibility equal to the frequency notation, then the new  $q'$  would depend on the fermionic frequencies (the precise dependency is channel-specific, but in general  $q' = f(q, k, k')$ ) and the transformed BSE would not be diagonal in  $q'$ .

Eq. (3.49) can be rewritten in terms of susceptibilities with the help of Eq. (3.42),

$$\chi_{1234}^{qkk'} = \chi_{0;1234}^{qkk'} - \frac{1}{\beta^2} \sum_{k_1k_2; abc\bar{d}} \chi_{0;12ba}^{qkk_1} \Gamma_{ph;abc\bar{d}}^{qk_1k_2} \chi_{ph;\bar{d}c34}^{qk_2k'} \tag{3.50a}$$

$$= \chi_{0;1234}^{qkk'} + \frac{1}{\beta^2} \sum_{k_1k_2; abc\bar{d}} \chi_{0;12ba}^{qkk_1} \Gamma_{ph;abc\bar{d}}^{qk_1k_2} \chi_{ph;\bar{d}c34}^{qk_2k'} \tag{3.50b}$$

$$= \chi_{0;1234}^{qkk'} - \frac{1}{2\beta^2} \sum_{k_1k_2; abc\bar{d}} \chi_{0;1c3a}^{qkk_1} \Gamma_{pp;abc\bar{d}}^{qk_1k_2} (\chi_{pp;\bar{d}2b4}^{qk_2k'} + \chi_{0;\bar{d}2b4}^{qk_2k'}). \tag{3.50c}$$

This is the most general form of the Bethe-Salpeter equations, where energy and momentum is conserved. If the system under consideration is additionally SU(2)-symmetric, then we can formulate the BSE in terms of density and magnetic spin components,

$$F_{d/m;ph;1234}^{qkk'} = \Gamma_{d/m;ph;1234}^{qkk'} - \frac{1}{\beta} \sum_{k_1k_2; abc\bar{d}} \Gamma_{d/m;ph;12ba}^{qkk_1} \chi_{0;abc\bar{d}}^{qk_1k_2} F_{d/m;ph;\bar{d}c34}^{qk_2k'} \quad \text{and} \tag{3.51a}$$

$$F_{d/m;\bar{p}\bar{h};1234}^{qkk'} = \Gamma_{d/m;\bar{p}\bar{h};1234}^{qkk'} - \frac{1}{\beta} \sum_{k_1k_2; abc\bar{d}} \Gamma_{d/m;\bar{p}\bar{h};12ba}^{qkk_1} \chi_{0;abc\bar{d}}^{qk_1k_2} F_{d/m;\bar{p}\bar{h};\bar{d}c34}^{qk_2k'}. \tag{3.51b}$$

Likewise, the BSE decouples for other spin-symmetric combinations in for the pp-channel. These are the (s)inglet and (t)riplet channel, where

$$F_{s/pp;1234}^{qkk'} = \Gamma_{s/pp;1234}^{qkk'} + \frac{1}{2\beta} \sum_{k_1k_2; abc\bar{d}} \Gamma_{s/pp;12ba}^{qkk_1} \chi_{0;abc\bar{d}}^{qk_1k_2} F_{s/pp;\bar{d}c34}^{qk_2k'} \quad \text{and} \tag{3.52}$$

$$F_{t;pp;1234}^{qkk'} = \Gamma_{t;pp;1234}^{qkk'} - \frac{1}{2\beta} \sum_{k_1 k_2; abcd} \Gamma_{t;pp;12ba}^{qkk_1} \chi_{0;abcd}^{qk_1 k_2} F_{t;pp;dca34}^{qk_2 k'}. \quad (3.53)$$

For a visual representation of the Bethe-Salpeter equation (3.49), see Fig. 3.10. The BSE of Eq. (3.49)

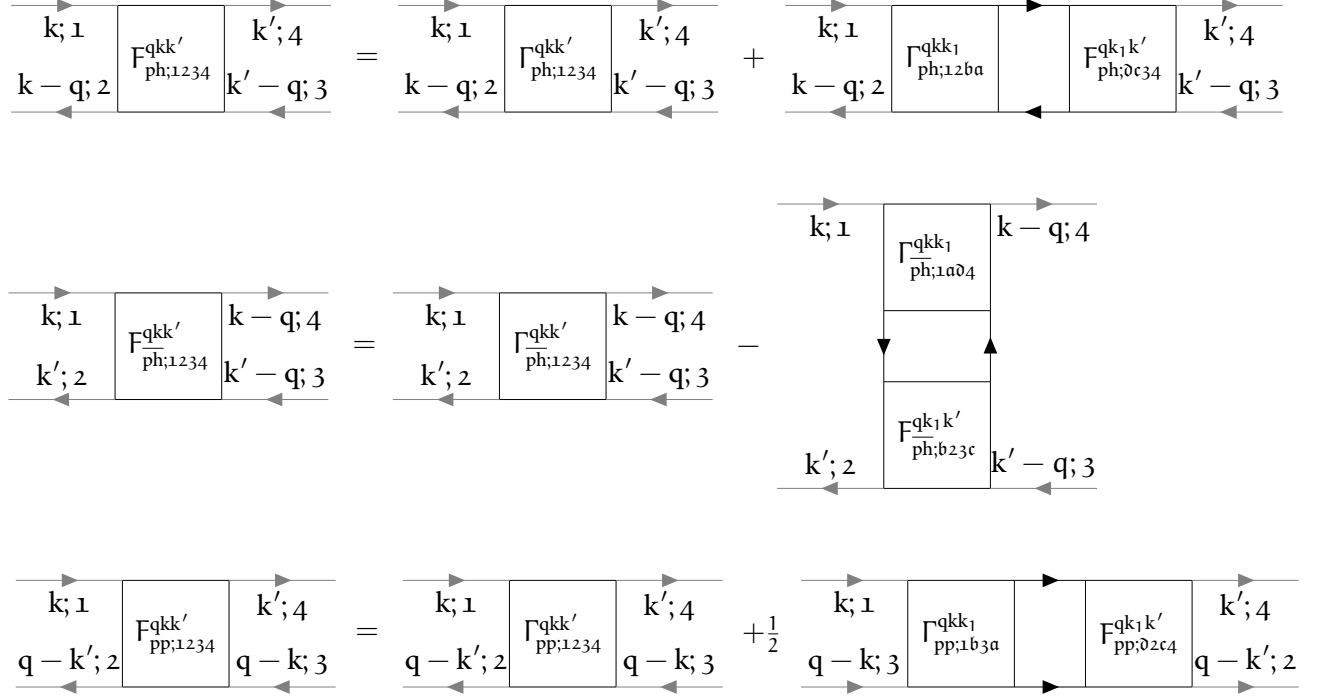


FIGURE 3.10 – Diagrammatic version of the BSE in all three channels for arbitrary spin components, see Eq. (3.49). The lower legs are exchanged in pp-notation, hence their direction is reversed.

needs to be inverted in order to be able to yield the full vertex  $F_{1234}^{qkk'}$ . This can be done in a smart way by viewing the multiplications of the vertex functions in the BSE as matrix multiplications written down in grouped indices. This means that for each transfer momentum  $q$ , we can generate a matrix from a vertex by grouping the left (right) two orbital indices and fermionic frequencies into a new grouped index  $n = \{n_1, n_2, k\}$  ( $m = \{n_3, n_4, k'\}$ ), such that [28]

$$F_{nm}^q = F_{1234}^{qkk'}. \quad (3.54)$$

This allows for a straightforward numerical implementation of vertex products and inversions with respect to these grouped indices. Hence, this yields for the full vertex  $F_{d/m;nm}^q$  obtained from the BSE,

$$F_{d/m;nm}^q = \left( \mathbb{1}_{nm} + \frac{1}{\beta} F_{d/m;nl}^q \chi_{0;lm}^q \right)^{-1}. \quad (3.55)$$

### 3.6 Schwinger-Dyson equation

To fill the missing gap in our (almost) complete theory of correlated electrons on a lattice, we have to consider the calculation of the self-energy which enters the many-body Green's function through



Eq. (3.18). This is done by the Schwinger-Dyson equation, which is derived as an equation of motion for the self-energy [27] and connects the self-energy to the full vertex via<sup>[9]</sup> [28, 29]

$$\begin{aligned}\Sigma_{12}^k &= \Sigma_{\text{HF};12}^k + \Sigma_{12}^{\text{conn};k} \\ &= 2 \underbrace{\sum_{ab;k'} \mathcal{U}_{12ab}^{q=0} n_{ba}^{k'}}_{\Sigma_{\text{HF};12}^k} - \underbrace{\sum_{ab,q} \mathcal{U}_{1ba2}^q n_{ba}^{k-q}}_{\Sigma_{12}^{\text{conn};k}} - \frac{1}{\beta} \sum_{\substack{abcdef \\ qk'}} \mathcal{U}_{a1bc}^q \chi_{0;cb\epsilon d}^{qk'k'} F_{d\epsilon 2f}^{qk'k} G_{af}^{k-q},\end{aligned}\quad (3.56)$$

where the first two sums in Eq. (3.56) are coined Hartree- and Fock-terms, respectively, and the third term is the vertex part and only contains connected diagrams. A visual representation of the Schwinger-Dyson equation can be seen in Fig. 3.11. The ph and ph contributions of the connected

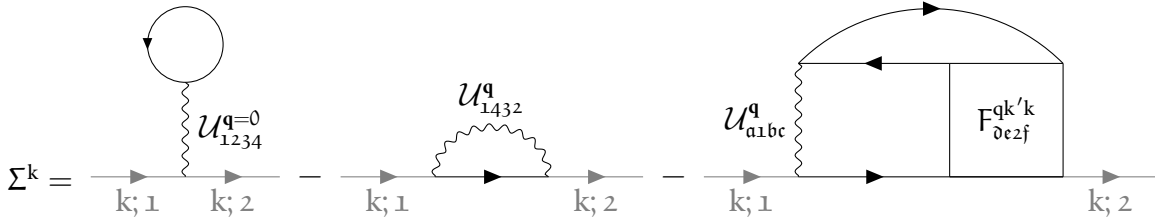


FIGURE 3.11 – Representation of the Schwinger-Dyson equation (3.56).

part yield separately (in ph notation)<sup>[10]</sup> [28]

$$\Sigma_{\text{ph};12}^{\text{conn};k} = -\frac{1}{\beta} \sum_{\substack{abcdef \\ qk'}} \mathcal{U}_{a1bc}^q \chi_{0;cb\epsilon d}^{qk'k'} F_{d\epsilon 2f}^{qk'k} G_{af}^{k-q} \quad \text{and} \quad (3.57a)$$

$$\Sigma_{\text{ph};12}^{\text{conn};\text{ph};k} = -\frac{1}{2\beta} \sum_{\substack{abcdef \\ qk'}} \tilde{\mathcal{U}}_{a1bc}^{k'-k} \chi_{0;cb\epsilon d}^{qk'k'} \left[ F_{d;2\epsilon d f}^{(k'-k)(k'-q)k'} + 3F_{m;2\epsilon d f}^{(k'-k)(k'-q)k'} \right] G_{af}^{k-q}. \quad (3.57b)$$

The self-energy  $\Sigma_{12}^k$  does not have to fulfill any crossing-symmetry relation, hence we do not use  $\mathcal{U}_{1234;\sigma\sigma'}^{qk'k'}$  from Eq. (3.66) here but rather the two terms with  $\mathcal{U}$  and  $\tilde{\mathcal{U}}$  separately. The total self-energy is now the sum of the Hartree-Fock contribution and the ph/ $\bar{\text{ph}}$  terms. We want to note that the Schwinger-Dyson equation can be rewritten in terms of three-leg vertices (also commonly called Hedin-vertices) instead of four-point Green's functions, see [30, 31] to eliminate the need of calculating the full vertex  $F$  via an inversion of the irreducible vertex  $\Gamma$ <sup>[11]</sup>. This equivalent formulation is commonly called the Hedin form. In this form, the SDE can be rewritten in terms of susceptibilities. We start by rewriting the full vertex as a combination of susceptibilities

$$F_{1234;\sigma\sigma'}^{qk'k'} = \beta^2 \left[ \left( \chi_{0;1234}^{qk'k'} \right)^{-1} - \sum_{k_1 k_2; abc d} \left( \chi_{0;12ba}^{qk'k_1} \right)^{-1} \chi_{abc d; \sigma\sigma'}^{qk_1 k_2} \left( \chi_{0;d\epsilon 34}^{qk_2 k'} \right)^{-1} \right]^{-1}. \quad (3.58)$$

<sup>[9]</sup>In its most general form, the self-energy  $\Sigma$  also depends on the particle spin  $\sigma$ . In the SU(2)-symmetric case however we can omit the spin label, since  $\Sigma_{\uparrow} = \Sigma_{\downarrow} = \Sigma$ .

<sup>[10]</sup>With the help of Eq. (3.37)

<sup>[11]</sup>In principle, one could retrieve the full vertex as  $F_r^q = [(\Gamma_r^q)^{-1} - \chi_0^q]^{-1}$ . However, as shown in Ref. [32], the (local) irreducible vertex  $\Gamma$  contains an infinite set of divergencies, hence inverting it is numerically unstable.

Here and in the following, we will restrict ourselves to the ph channel reducibility and frequency notation if not stated otherwise. Next, we define the irreducible vertex as the first-order contribution - which is the bare Coulomb interaction in crossing-symmetric notation, see Eq. (3.66) - and the rest,

$$\Gamma_{1234;\sigma\sigma'}^{\text{qkk}'} = \mathcal{U}_{1234;\sigma\sigma'}^{\text{qkk}'} + \delta\Gamma_{1234;\sigma\sigma'}^{\text{qkk}'} \quad (3.59)$$

It is then straightforward to define an auxiliary susceptibility (denoted by the asterisk \*)

$$\begin{aligned} \chi_{1234;\sigma\sigma'}^{*,\text{qkk}'} &= \left[ \left( \chi_{0;1234}^{\text{qkk}} \right)^{-1} + \frac{1}{\beta^2} \delta\Gamma_{1234;\sigma\sigma'}^{\text{qkk}'} \right]^{-1} \\ &= \left[ \left( \chi_{0;1234}^{\text{qkk}} \right)^{-1} + \frac{1}{\beta^2} \left( \Gamma_{1234;\sigma\sigma'}^{\text{qkk}'} - \mathcal{U}_{1234;\sigma\sigma'}^{\text{qkk}'} \right) \right]^{-1}, \end{aligned} \quad (3.60)$$

with which we can rewrite the generalized susceptibility as

$$\chi_{1234;\sigma\sigma'}^{\text{qkk}'} = \chi_{1234;\sigma\sigma'}^{*,\text{qkk}'} - \sum_{\mathbf{k}_1 \mathbf{k}_2; \mathbf{a} \mathbf{b} \mathbf{c} \mathbf{d}} \chi_{12\mathbf{b}\mathbf{a};\sigma\sigma'}^{*,\text{qkk}_1} \mathcal{U}_{\mathbf{a}\mathbf{b}\mathbf{c}\mathbf{d};\sigma\sigma'}^{\text{qk}_1 \mathbf{k}_2} \chi_{\mathbf{d}\mathbf{c}\mathbf{34};\sigma\sigma'}^{\text{qk}_2 \mathbf{k}'}. \quad (3.61)$$

Previously, the BSE was formulated as a ladder with  $\Gamma_{1234}^{\text{qkk}'}$  and  $\chi_{0;1234}^{\text{qkk}}$  as building blocks. The rewritten BSE can now be understood as a ladder with  $\chi_{1234;\sigma\sigma'}^{*,\text{qkk}'}$  and  $\mathcal{U}_{1234;\sigma\sigma'}^{\text{qkk}'}$  as building blocks. Here, the auxiliary susceptibility can be seen as the irreducible part with respect to the bare Coulomb interaction, contrary to how  $\Gamma_{1234}^{\text{qkk}'}$  is the set of irreducible diagrams with respect to cutting two Green function lines (or a bare susceptibility  $\chi_{0;1234}^{\text{qkk}}$ ). Hence, this is commonly called interaction-reducibility [33]. The BSE displayed in terms of susceptibilities can be seen in Fig. 3.12. If one

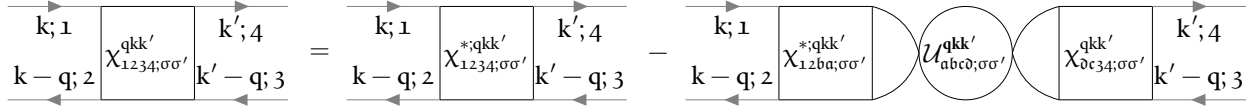


FIGURE 3.12 – Interaction-reducible form of the Schwinger-Dyson equation (3.61) with susceptibilities.

neglects the nonlocal  $\overline{\text{ph}}$  contribution from the bare Coulomb interaction, one can rewrite the following expression in terms of sums of susceptibilities, where after some algebra,

$$\sum_{\mathbf{k}'; \mathbf{a} \mathbf{b}} F_{12\mathbf{a} \mathbf{b}; \sigma \sigma'}^{\text{qkk}'} \chi_{0; \mathbf{b} \mathbf{a} 34}^{\text{qk}' \mathbf{k}'} = \beta \sum_{\mathbf{a} \mathbf{b} \mathbf{c} \mathbf{d}; \sigma_1} \gamma_{12\mathbf{a} \mathbf{b}; \sigma \sigma'}^{\text{qk}} \left( \mathbb{1}_{\mathbf{b} \mathbf{a} 34}^{\text{kk}'} - \mathcal{U}_{\mathbf{b} \mathbf{a} \mathbf{d} \mathbf{c}; \sigma \sigma_1}^{\text{q}} \chi_{\mathbf{d} \mathbf{c} 34; \sigma_1 \sigma}^{\text{q}} \right), \quad (3.62)$$

where the Fermi-Bose three-leg vertex  $\gamma_{1234;\sigma\sigma'}^{\text{qk}}$  is defined as

$$\gamma_{1234;\sigma\sigma'}^{\text{qk}} = \beta \sum_{\mathbf{k}_1; \mathbf{a} \mathbf{b}} \left( \chi_{0; 12\mathbf{a} \mathbf{b}}^{\text{qkk}} \right)^{-1} \chi_{\mathbf{b} \mathbf{a} 34; \sigma \sigma'}^{*,\text{qkk}_1}. \quad (3.63)$$

This allows us to rewrite Eq. (3.56) as

$$\Sigma_{12;\sigma\sigma'}^{\mathbf{k}} = \Sigma_{\text{HF};12}^{\mathbf{k}} - \sum_{\substack{\mathbf{q}; \mathbf{a} \mathbf{b} \mathbf{c} \mathbf{d} \\ \mathbf{e} \mathbf{f} \mathbf{g} \mathbf{h}; \sigma_1}} \mathcal{U}_{\mathbf{a} 1 \mathbf{b} \mathbf{c}}^{\mathbf{q}} \left[ \gamma_{\mathbf{a} \mathbf{c} \mathbf{e} \mathbf{d}; \sigma \sigma'}^{\text{qk}} \left( \mathbb{1}_{\mathbf{d} \mathbf{e} \mathbf{h} 2} - \mathcal{U}_{\mathbf{d} \mathbf{e} \mathbf{f} \mathbf{g}; \sigma \sigma_1}^{\mathbf{q}} \chi_{\mathbf{g} \mathbf{f} \mathbf{h} 2; \sigma_1 \sigma'}^{\mathbf{q}} \right) \right] G_{\mathbf{b} \mathbf{h}}^{\mathbf{k}-\mathbf{q}}. \quad (3.64)$$

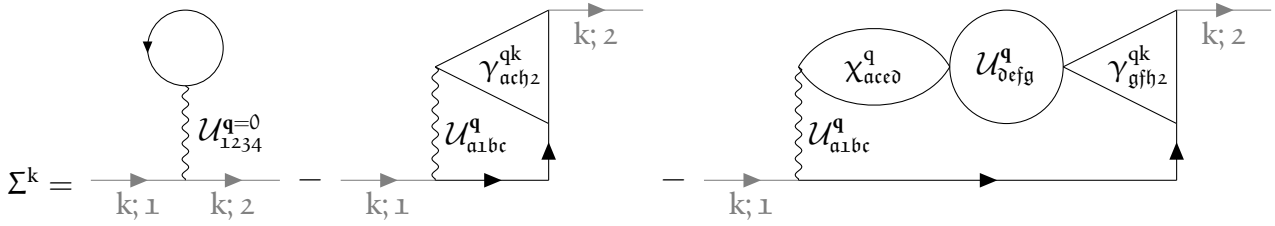


FIGURE 3.13 – Interaction-reducible form of the Schwinger-Dyson equation (3.64) with three-leg vertices.

A visual representation of the rewritten SDE can be found in Fig. 3.13. This expression has some numerical advantages, since the frequency dimensions of the Fermi-Bose vertices needed for the calculation of the self-energy are by one smaller compared to the approach with the full vertices, hence reducing the required memory storage in the process.

For numerical calculations of the equations in the above sections one is always restricted to a certain frequency range where the input quantities are known, which is usually limited by time and the impurity solver’s capabilities. However, the full and irreducible vertex functions outside of this “core” frequency box are often not negligible<sup>[12]</sup>. Hence for more accurate descriptions of materials, one employs explicit asymptotics that should mimic the outer frequency structure of the vertex functions. These asymptotics can be done in many ways, from the simple concatenation of constant values<sup>[13]</sup> to more complicated formulations using so-called kernel functions. In this thesis we want to introduce two treatments of asymptotic behavior in vertex functions: one being the kernel-function approach, where upon the pioneering work of Ref. [34] and subsequent development of a full local framework [22, 35–39] has been developed that mimics the coarse frequency structure of the vertex function outside of the core frequency region; and the other being an “RPA-esque” approach [40], where a constant value outside the core frequency region of the irreducible vertex is assumed and diagrams are generated by a ladder, similar to the BSE. We will outline the two methods in detail, explain their advantages and drawbacks and reason briefly when to choose either of them. Since the former method using kernel-functions has not been generalized to non-local quantities yet at the writing of this thesis, we will derive equations that include non-local contributions to better incorporate these asymptotics in the upcoming frameworks that will be introduced.

### 3.7 Vertex asymptotics

A full treatment of frequency and momentum dependence of multi-orbital vertex functions severely restricts the speed and memory consumption of numerical calculations. A step towards reducing the computational cost of numerical implementations of equations involving vertex functions, such as the Bethe-Salpeter equations, see Sec. 3.5, or the Schwinger-Dyson equation, see Sec. 3.6, thus requires an efficient treatment of the vertex for high Matsubara frequencies. As noted above, we will describe two treatments of vertex asymptotics in the following.

<sup>[12]</sup> Especially not if one is interested in low-temperature behavior. Since the frequencies scale with  $\sim \frac{1}{\beta} \sim T$ , the smaller the temperature, the smaller the effective frequency box. Even though the full and irreducible vertex functions decay like  $\frac{1}{\nu}$  as  $\nu \rightarrow \infty$ , the contributions outside of the core frequency region are of importance.

<sup>[13]</sup> Like the bare Coulomb interaction  $\mathcal{U}_{1234;\sigma\sigma'}^{qkk'}$ ,

### 3.7.1 Kernel-function asymptotics

Shortly, we will see, that the full vertex in the high-frequency regime, which generally depends on three independent frequency parameters, can be approximated well as an object with only two frequency dimensions, thus drastically reducing the storage capacity required, while also reducing the computational cost after assembling these objects. Let us start with a sketch of the basic idea of how to take advantage of certain frequency structures when handling explicit vertex asymptotics. In

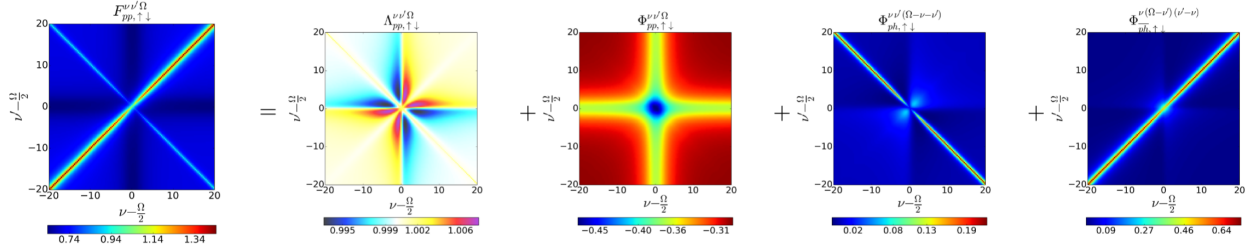


FIGURE 3.14 – Numerical SIAM results for all local vertices contained in the parquet equation Eq. (3.33) for vanishing transfer frequency  $\Omega = 0$ , taken from Ref. [35]. In our convention,  $\Omega$  should be replaced by  $\omega$ .

Fig. 3.14, the frequency dependence of local vertex functions  $F_{pp;\uparrow\downarrow}^{\omega\nu\nu'}$ ,  $\Lambda_{pp;\uparrow\downarrow}^{\omega\nu\nu'}$  and  $\Phi_{r;\uparrow\downarrow}^{\omega\nu\nu'}$  calculated for the Single-Impurity Anderson Model (SIAM) are shown for vanishing transfer frequency  $\omega$  [35]. From this, one can see three very prominent and distinct features of the full vertex  $F$ : (i) a constant background that differs from the (local and constant) Hubbard interaction  $U$ ; (ii) two diagonal structures, the main ( $\nu = \nu'$ ) and secondary ( $\nu = -\nu'$ ) diagonal; and (iii) a “cross”-like structure along  $\nu = \pm \frac{\pi}{\beta}$  and  $\nu' = \pm \frac{\pi}{\beta}$ . While only shown for the antiparallel spin combination  $\uparrow\downarrow$  and vanishing transfer frequency  $\omega = 0$ , the features are analogous for the parallel spin combination  $\uparrow\uparrow$  and for finite  $\omega \neq 0$ . These three attributes do *not* decay for high Matsubara frequencies  $\nu$  and  $\nu'$  and therefore indicate complex asymptotic behaviour. The individual asymptotic contributions of the fully irreducible vertex  $\Lambda$  and the reducible vertex in channel  $r$  to the full vertex  $F$  are written in detail in Ref. [35]. Summarized,  $\Lambda$  adds a constant background of size  $U$ ,  $\Phi_{ph}$  adds a secondary diagonal structure,  $\Phi_{ph}$  adds a diagonal structure and  $\Phi_{pp}$  adds a constant background and a “cross”-like structure. Notice that the description in Ref. [35] only refers to the SIAM model and considers solely the one-band case with local quantities and a constant local interaction  $U$ . An extension to a multi-orbital formalism and momentum-dependent vertices and interaction  $U$  follows naturally and will be discussed shortly.

The simplest quantity to describe in terms of their asymptotics is the fully irreducible vertex  $\Lambda_{1234}^{qkk'}$ , for which

$$\Lambda_{1234;\sigma\sigma'}^{\text{asympt};qkk'} \approx \mathcal{U}_{1234;\sigma\sigma'}^{qkk'}, \quad (3.65)$$

where  $\mathcal{U}_{1234;\sigma\sigma'}^{qkk'}$  is the non-local Coulomb interaction, written in crossing-symmetric notation [41]

$$\mathcal{U}_{1234;\sigma\sigma'}^{qkk'} = \underbrace{U_{1234} + V_{1234}^q}_{U_{1234}^q} - \delta_{\sigma\sigma'} \underbrace{\left( U_{2314} + V_{2314}^{k'-k} \right)}_{\tilde{U}_{1234}^{k'-k}}, \quad (3.66)$$

containing the purely local interaction  $U$  and the purely non-local interaction  $V$ . Eq. (3.66) is diagrammatically displayed in Fig. 3.15. Constructing d, m, s and t combinations of Eq. (3.66) is

$$\mathcal{U}_{1234;\sigma\sigma'}^{qkk'} \equiv \sigma_2^1 \left( \mathcal{U}_{1234;\sigma\sigma'}^{qkk'} \right)_{\substack{4 \\ 3}} = \begin{array}{c} 2 \\ 1 \end{array} \mathcal{U}_{1234}^q \begin{array}{c} 3 \\ 4 \end{array} - \delta_{\sigma\sigma'} \begin{array}{c} 1 \\ 2 \\ 4 \end{array} \mathcal{U}_{1234}^{k'-k} \begin{array}{c} 3 \\ 4 \end{array}$$

FIGURE 3.15 – Crossing-symmetric interaction, see Eq. (3.66).

useful for future calculations,

$$\mathcal{U}_{d;1234}^{qkk'} = 2\mathcal{U}_{1234}^q - \tilde{\mathcal{U}}_{1234}^{k'-k}, \quad (3.67a)$$

$$\mathcal{U}_{m;1234}^{qkk'} = -\tilde{\mathcal{U}}_{1234}^{k'-k}, \quad (3.67b)$$

$$\mathcal{U}_{s;1234}^{qkk'} = \mathcal{U}_{1234}^{k+k'-q} + \tilde{\mathcal{U}}_{1234}^{k'-k} \quad \text{and} \quad (3.67c)$$

$$\mathcal{U}_{t;1234}^{qkk'} = \mathcal{U}_{1234}^{k+k'-q} - \tilde{\mathcal{U}}_{1234}^{k'-k}. \quad (3.67d)$$

Next, we begin examining the diagrams contributing to  $\Phi_r$ . A smart choice introduced in Ref. [35] is to classify these diagrams in each channel further into three categories:

- Class 1: These are diagrams which connect incoming and outgoing particles only by a single interaction vertex. These diagrams are bubble diagrams and hence only depend on a single bosonic frequency and momentum. The sum of all these diagrams will be encoded in the variable  $\mathcal{K}_{r;1234;\sigma\sigma'}^{(1);q}$ , see the first line in Fig. 3.16.
- Class 2: Diagrams corresponding to class 2 are identified by them having either the incoming *or* outgoing particles connected to the same interaction vertex. These diagrams depend on the bosonic transfer frequency and momentum and one fermionic frequency and momentum. The sum of all these diagrams will be encoded in the variables  $\mathcal{K}_{r;1234;\sigma\sigma'}^{(2);qk}$  and  $\bar{\mathcal{K}}_{r;1234;\sigma\sigma'}^{(2);qk}$ , depending on whether the outgoing particles ( $\mathcal{K}$ ) or the incoming particles ( $\bar{\mathcal{K}}$ ) are connected to the interaction vertex, see the second line in Fig. 3.16.  $\mathcal{K}$  and  $\bar{\mathcal{K}}$  are related to each other via time-reversal symmetry, where in the case of a system with additional SU(2)-symmetry corresponds to [27]  $\mathcal{K}_{r;1234;\sigma\sigma'}^{(2);qk} = \bar{\mathcal{K}}_{r;1234;\sigma\sigma'}^{(2);qk}$ .
- Class 3: These are diagrams where each external Green's function is connected to a different interaction vertex. These diagrams are parametrized by three independent frequency and momentum arguments and are encoded in the “rest” function  $\mathcal{R}_{r;1234;\sigma\sigma'}^{qkk'}$ .

In the following, we will refer to  $\mathcal{K}^{(1)}$ ,  $\mathcal{K}^{(2)}$  and  $\bar{\mathcal{K}}^{(2)}$  as kernel functions. One now can - with the help of these classifications - write the reducible  $\Phi_r$ -vertices as a decomposition of the different kernel functions and the “rest”-function

$$\Phi_{r;1234;\sigma\sigma'}^{qkk'} = \mathcal{K}_{r;1234;\sigma\sigma'}^{(1);q} + \mathcal{K}_{r;1234;\sigma\sigma'}^{(2);qk} + \mathcal{K}_{r;1234;\sigma\sigma'}^{(2);qk'} + \mathcal{R}_{r;1234;\sigma\sigma'}^{qkk'}. \quad (3.68)$$

This composition is *per se* exact. However, to take advantage of this formalism for numerical calculations, one discards the “rest”-function due to its additional frequency dependence entering the inner propagators, resulting in a quicker drop-off in all frequency directions. Thus, the approximation

$$\Phi_{r;1234;\sigma\sigma'}^{\text{asympt};qkk'} \approx \mathcal{K}_{r;1234;\sigma\sigma'}^{(1);q} + \mathcal{K}_{r;1234;\sigma\sigma'}^{(2);qk} + \mathcal{K}_{r;1234;\sigma\sigma'}^{(2);qk'} \quad (3.69)$$

serves as a valid expression for the high-frequency regime of  $\Phi_r$  and becomes exact for  $\nu, \nu' \rightarrow \infty$  [35]. As we can see above, the quantities on the right hand side of Eq. (3.69) only depend on one (q) or two (q, k) Matsubara frequencies and momenta instead of three, reducing the numerical complexity and memory usage for  $\Phi_r$  significantly. Using these explicit asymptotics results in a tremendous improvement of numerical results over a simple truncation in  $\Phi_r$  for high frequencies [35]. The explicit expressions for the kernel functions needed to calculate the reducible diagrams can be obtained by [22, 42, 43]

$$\mathcal{K}_{\text{ph};1234;\sigma\sigma'}^{(1);q} = \sum_{\substack{abc\delta; k_1 k_2 \\ \sigma_1 \sigma_2}} \mathcal{U}_{12ab;\sigma\sigma_1}^{qk_1} \chi_{ba\delta c;\sigma_1 \sigma_2}^{qk_1 k_2} \mathcal{U}_{c\delta 34;\sigma_2 \sigma'}^{q(-k_2)}, \quad (3.70)$$

$$\mathcal{K}_{\text{pp};1234;\sigma\sigma'}^{(1);q} = \frac{1}{4} \sum_{\substack{abc\delta; k_1 k_2 \\ \sigma_1 \sigma_2 \sigma_3 \sigma_4}} \mathcal{U}_{1b3a}^{qk_1} \chi_{ac\delta b}^{qk_1 k_2} \mathcal{U}_{\delta 2c4}^{q(-k_2)} \mathcal{U}_{\sigma_4 \sigma_3 \sigma'}^{q}, \quad (3.71)$$

$$\begin{aligned} \mathcal{K}_{\text{ph};1234;\sigma\sigma'}^{(2);qk} &= \sum_{\substack{ab; k_1 \\ \sigma_1}} F_{12ab;\sigma\sigma_1}^{qkk_1} \chi_{0;baab}^{qk_1 k_1} \mathcal{U}_{ba34;\sigma_1 \sigma'}^{q(-k_1)} - \mathcal{K}_{\text{ph};1234;\sigma\sigma'}^{(1);q} \\ &= - \sum_{\substack{ab; k_1 \\ \sigma_1}} \frac{\chi_{c\delta ab;\sigma\sigma_1}^{qkk_1}}{G_{c1}^k G_{2\delta}^{k-q}} \mathcal{U}_{ba34;\sigma_1 \sigma'}^{q(-k_1)} - \mathcal{K}_{\text{ph};1234;\sigma\sigma'}^{(1);q} \end{aligned} \quad (3.72)$$

$$\begin{aligned} \mathcal{K}_{\text{pp};1234;\sigma\sigma'}^{(2);qk} &= \frac{1}{2} \sum_{\substack{ab; k_1 \\ \sigma_1 \sigma_2 \sigma_3 \sigma_4}} F_{pp;1a3b}^{qkk_1} \chi_{0;baab}^{qk_1 k_1} \mathcal{U}_{b2a4}^{q(-k_1)} \mathcal{U}_{\sigma_2 \sigma_1 \sigma'}^{q} - \mathcal{K}_{\text{pp};1234;\sigma\sigma'}^{(1);q} \\ &= - \frac{1}{2} \sum_{\substack{abc\delta; k_1 \\ \sigma_1 \sigma_2 \sigma_3 \sigma_4}} \frac{\chi_{pp;ca\delta b}^{qkk_1}}{G_{1c}^k G_{3\delta}^{k-q}} \mathcal{U}_{b2a4}^{q(-k_1)} \mathcal{U}_{\sigma_2 \sigma_1 \sigma'}^{q} - \mathcal{K}_{\text{pp};1234;\sigma\sigma'}^{(1);q} \end{aligned} \quad (3.73)$$

where the subtraction of  $\mathcal{K}^{(1)}$  in the kernel-2 function is to account for double-counting of diagrams and  $\mathcal{U}_{1234;\sigma\sigma'}^{qk'}$  is obtained from Eq. (3.66) by setting  $\mathbf{k} = \mathbf{0}$ . Both kernel functions are displayed diagrammatically for the ph-channel in Fig. 3.16. The density and magnetic contributions to the

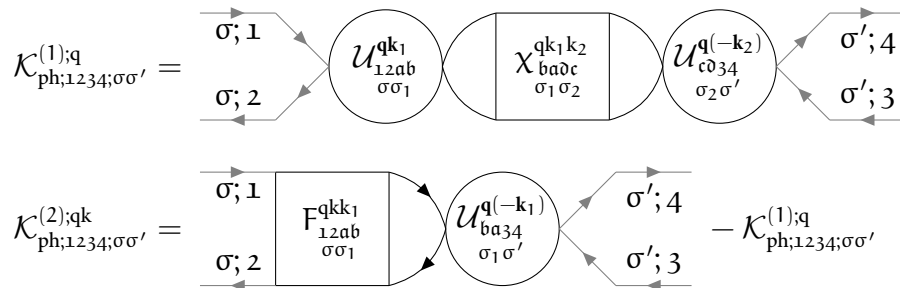


FIGURE 3.16 – Diagrammatic version of the kernel-1 and kernel-2 functions of Eq. (3.70) and Eq. (3.72).

kernel functions read<sup>[14]</sup>

$$\mathcal{K}_{d;1234}^{(1);q} = \sum_{\substack{abc\delta \\ k_1 k_2}} \mathcal{U}_{d;12ab}^{qk_1} \chi_{d;ba\delta c}^{qk_1 k_2} \mathcal{U}_{d;c\delta 34}^{q(-k_2)}, \quad (3.74a)$$

<sup>[14]</sup> Remember, that for density and magnetic contributions, frequencies should be in ph notation whereas for (s)inglet and (t)riplet contributions, frequencies should be in pp notation.

$$\mathcal{K}_{m;1234}^{(1);q} = \sum_{\substack{abcd \\ k_1 k_2}} \mathcal{U}_{m;12ab}^{qk_1} \chi_{m;ba\bar{d}c}^{qk_1 k_2} \mathcal{U}_{m;c\bar{d}34}^{q(-k_2)}, \quad (3.74b)$$

$$\begin{aligned} \mathcal{K}_{d;1234}^{(2);qk} &= \sum_{ab;k_1} F_{d;12ab}^{qkk_1} \chi_{0;b\bar{a}ab}^{qk_1 k_1} \mathcal{U}_{d;ba34}^{q(-k_1)} - \mathcal{K}_{d;1234}^{(1);q} \\ &= - \sum_{ab\bar{c}\bar{d};k_1} \frac{\chi_{d;c\bar{d}ab}^{qkk_1}}{G_{c1}^k G_{2\bar{d}}^{k-q}} \mathcal{U}_{d;ba34}^{q(-k_1)} - \mathcal{K}_{d;1234}^{(1);q} \quad \text{and} \end{aligned} \quad (3.74c)$$

$$\begin{aligned} \mathcal{K}_{m;1234}^{(2);qk} &= \sum_{ab;k_1} F_{m;12ab}^{qkk_1} \chi_{0;b\bar{a}ab}^{qk_1 k_1} \mathcal{U}_{m;ba34}^{q(-k_1)} - \mathcal{K}_{m;1234}^{(1);q} \\ &= - \sum_{ab\bar{c}\bar{d};k_1} \frac{\chi_{m;c\bar{d}ab}^{qkk_1}}{G_{c1}^k G_{2\bar{d}}^{k-q}} \mathcal{U}_{m;ba34}^{q(-k_1)} - \mathcal{K}_{m;1234}^{(1);q}. \end{aligned} \quad (3.74d)$$

The s/t combinations can be constructed analogously for the pp-channel (written in pp frequency notation):

$$\mathcal{K}_{s;1234}^{(1);q} = \frac{1}{4} \sum_{\substack{abcd \\ k_1 k_2}} \mathcal{U}_{s;1b3a}^{qk_1} \chi_{s;a\bar{c}b\bar{d}}^{qk_1 k_2} \mathcal{U}_{s;\bar{d}2c4}^{q(-k_2)} \stackrel{(3.44)}{=} \frac{1}{2} \sum_{\substack{abcd \\ k_1 k_2}} \mathcal{U}_{s;1b3a}^{qk_1} \chi_{ac\bar{b}\bar{d};\uparrow\downarrow}^{pp;qk_1 k_2} \mathcal{U}_{s;\bar{d}2c4}^{q(-k_2)}, \quad (3.75a)$$

$$\mathcal{K}_{t;1234}^{(1);q} = \frac{1}{4} \sum_{\substack{abcd \\ k_1 k_2}} \mathcal{U}_{t;1b3a}^{qk_1} \chi_{t;a\bar{c}b\bar{d}}^{qk_1 k_2} \mathcal{U}_{t;\bar{d}2c4}^{q(-k_2)} \stackrel{(3.44)}{=} 0, \quad (3.75b)$$

$$\begin{aligned} \mathcal{K}_{s;1234}^{(2);qk} &= \frac{1}{2} \sum_{ab;k_1} F_{s;1a3b}^{qkk_1} \chi_{0;b\bar{a}ab}^{qk_1 k_1} \mathcal{U}_{s;b2a4}^{q(-k_1)} - \mathcal{K}_{s;1234}^{(1);q} \\ &= - \frac{1}{2} \sum_{ab\bar{c}\bar{d};k_1} \frac{\chi_{s;c\bar{a}db}^{qkk_1}}{G_{1c}^k G_{3\bar{d}}^{k-q}} \mathcal{U}_{s;b2a4}^{q(-k_1)} - \mathcal{K}_{s;1234}^{(1);q} \end{aligned} \quad (3.75c)$$

$$\stackrel{(3.44)}{=} - \sum_{ab\bar{c}\bar{d};k_1} \frac{\chi_{ca\bar{d}b;\uparrow\downarrow}^{pp;qkk_1}}{G_{1c}^k G_{3\bar{d}}^{k-q}} \mathcal{U}_{s;b2a4}^{q(-k_1)} - \mathcal{K}_{s;1234}^{(1);q} \quad \text{and}$$

$$\begin{aligned} \mathcal{K}_{t;1234}^{(2);qk} &= \frac{1}{2} \sum_{ab;k_1} F_{t;1a3b}^{qkk_1} \chi_{0;b\bar{a}ab}^{qk_1 k_1} \mathcal{U}_{t;b2a4}^{q(-k_1)} - \mathcal{K}_{t;1234}^{(1);q} \\ &= - \frac{1}{2} \sum_{ab\bar{c}\bar{d};k_1} \frac{\chi_{t;c\bar{a}db}^{qkk_1}}{G_{1c}^k G_{3\bar{d}}^{k-q}} \mathcal{U}_{t;b2a4}^{q(-k_1)} - \mathcal{K}_{t;1234}^{(1);q} \stackrel{(3.44)}{=} 0. \end{aligned} \quad (3.75d)$$

Finally, the asymptotic part of the full vertex  $(F_{r;1234;\sigma\sigma'}^{\text{asympt};qkk'})$  can now be assembled using the asymptotic contributions of  $\mathcal{L}_{1234;\sigma\sigma'}^{\text{asympt};qkk'}$  and  $\Phi_{r;1234;\sigma\sigma'}^{\text{asympt};qkk'}$  through the parquet decomposition of Eq. (3.33). This results in

$$F_{1234;\sigma\sigma'}^{\text{asympt};qkk'} - \mathcal{U}_{1234;\sigma\sigma'}^{qkk'} = \Phi_{ph;1234;\sigma\sigma'}^{\text{asympt};qkk'} + \Phi_{\bar{ph};1234;\sigma\sigma'}^{\text{asympt};qkk'} + \Phi_{pp;1234;\sigma\sigma'}^{\text{asympt};qkk'}, \quad (3.76)$$

or explicitly with kernel-1 and kernel-2 functions,

$$\begin{aligned} F_{1234;\sigma\sigma'}^{\text{asympt};qkk'} - \mathcal{U}_{1234;\sigma\sigma'}^{qkk'} &= \mathcal{K}_{ph;1234;\sigma\sigma'}^{(1);q} + \mathcal{K}_{ph;1234;\sigma\sigma'}^{(2);qk} + \mathcal{K}_{ph;1234;\sigma\sigma'}^{(2);qk'} \\ &\quad + \mathcal{K}_{\bar{ph};1234;\sigma\sigma'}^{(1);q} + \mathcal{K}_{\bar{ph};1234;\sigma\sigma'}^{(2);qk} + \mathcal{K}_{\bar{ph};1234;\sigma\sigma'}^{(2);qk'} \\ &\quad + \mathcal{K}_{pp;1234;\sigma\sigma'}^{(1);q} + \mathcal{K}_{pp;1234;\sigma\sigma'}^{(2);qk} + \mathcal{K}_{pp;1234;\sigma\sigma'}^{(2);qk'}. \end{aligned} \quad (3.77)$$



The asymptotic behavior of the irreducible vertex in channel  $r$  follows from Eq. (3.34),

$$\Gamma_{r;1234;\sigma\sigma'}^{\text{asympt};qkk'} = F_{1234;\sigma\sigma'}^{\text{asympt};qkk'} - \Phi_{r;1234;\sigma\sigma'}^{\text{asympt};qkk'} \quad (3.78)$$

and reads for the  $ph$ -channel explicitly

$$\begin{aligned} \Gamma_{ph;1234;\sigma\sigma'}^{\text{asympt};qkk'} &= \mathcal{U}_{1234;\sigma\sigma'}^{qkk'} + \Phi_{ph;1234;\sigma\sigma'}^{\text{asympt};qkk'} + \Phi_{pp;1234;\sigma\sigma'}^{\text{asympt};qkk'} \\ &= \mathcal{U}_{1234;\sigma\sigma'}^{qkk'} - \Phi_{ph;3214;\sigma'\sigma}^{\text{asympt};(k'-k)(k'-q)k'} + \Phi_{pp;1234;\sigma\sigma'}^{\text{asympt};(k+k'-q)kk'}, \end{aligned} \quad (3.79)$$

where we used Eq. (3.36) to transform the  $\overline{ph}$ -channel reducible vertex to a  $ph$ -channel reducible one. From this follows the irreducible vertex in the density and magnetic channel (in  $ph$  frequency notation) [36]

$$\begin{aligned} \Gamma_{d;1234}^{\text{asympt};qkk'} &= \mathcal{U}_{d;1234}^{qkk'} - \frac{1}{2}\Phi_{d;3214}^{\text{asympt};(k'-k)(k'-q)k'} - \frac{3}{2}\Phi_{m;3214}^{\text{asympt};(k'-k)(k'-q)k'} \\ &\quad + \frac{1}{2}\Phi_{s;1234}^{\text{asympt};(k+k'-q)kk'} + \frac{3}{2}\Phi_{t;1234}^{\text{asympt};(k+k'-q)kk'}, \end{aligned} \quad (3.80a)$$

$$\begin{aligned} \Gamma_{m;1234}^{\text{asympt};qkk'} &= \mathcal{U}_{m;1234}^{qkk'} - \frac{1}{2}\Phi_{d;3214}^{\text{asympt};(k'-k)(k'-q)k'} + \frac{1}{2}\Phi_{m;3214}^{\text{asympt};(k'-k)(k'-q)k'} \\ &\quad - \frac{1}{2}\Phi_{s;1234}^{\text{asympt};(k+k'-q)kk'} + \frac{1}{2}\Phi_{t;1234}^{\text{asympt};(k+k'-q)kk'}, \end{aligned} \quad (3.80b)$$

where the  $\Phi_{r;1234}^{\text{asympt};qkk'}$  are given by the kernel functions of Eq. (3.74) and Eq. (3.75). The irreducible vertices in channels  $\overline{ph}$  and  $pp$  in  $m/d$  and  $s/t$  combinations can be constructed analogously.

### 3.7.2 U-range asymptotics

Aside from the kernel-function formalism introduced above, there also exist many other asymptotic schemes for vertex functions. The second one we would like to cover in this thesis is the “U-range” approach, where the irreducible vertex  $\Gamma_{1234;\sigma\sigma'}^{qkk'}$  is padded with the bare non-local Coulomb interaction  $\mathcal{U}_{1234;\sigma\sigma'}^{qkk'}$ , see Eq. (3.66), in the high-frequency regime. This in turn means that there is no complicated frequency structure for the asymptotic region. We denote some equations that are necessary to employ these types of asymptotics and follow Ref. [40] with the addition of multi-orbital notation. First, we will split up the frequencies into a “core” and an “asymptotic” region and denote quantities that exist in those frequency regimes with an additional sub- or superscript  $\in \{\text{core}, \text{asympt}\}$ . Generally speaking, we require  $n_{\text{asympt}} \geq n_{\text{core}}$ , where  $n$  is the number of fermionic Matsubara frequencies. Furthermore, if a quantity is written as  $(A^{\text{asympt}})_{\text{core}}$  it means that the asymptotic value of  $A$  is cut to the core frequency region. Additionally, the size change and matrix inverse do *not* commute, i.e.,  $A_{\text{core}}^{-1} \equiv (A^{\text{core}})^{-1} \neq (A^{-1})_{\text{core}}$ . This only commutes if the matrix  $A$  is block-diagonal.

The advantages of this method are not only the simpler way of treating asymptotics, as no complicated kernel-functions are needed, but also considers the ease of extending  $n_{\text{asympt}}$  without too much computational effort. As we will see shortly, we only need to solve the  $n_{\text{asympt}}$ -size of the local inverse BSE once and the rest of the equations can be performed within  $n_{\text{core}}$ . This allows us to increase  $n_{\text{asympt}}$  to very large sizes without sacrificing too much computational time and memory. Fortunately, as will be seen later in Sec. 3.9, this only needs to be done once at the beginning of the routine of the dynamical vertex approximation, since the local irreducible vertex is constant throughout the



DΓA algorithm. Only the bare bubble susceptibility  $\chi_{0;1234}^{\text{qk}}$  has to be known additionally, however, due to the simple frequency dependence of this quantity, it is easily available for  $n_{\text{asympt}}$  Matsubara frequencies.

We begin by extracting the local irreducible vertex  $\Gamma_{1234;\sigma\sigma'}^{\omega\nu\nu'}$  from the generalized susceptibility and the bare bubble susceptibility obtained from the impurity solver in the core region,

$$\Gamma_{1234;\sigma\sigma'}^{\text{core};\omega\nu\nu'} = \left(\chi_{1234;\sigma\sigma'}^{\text{core};\omega\nu\nu'}\right)^{-1} - \left(\chi_{0;1234}^{\text{core};\omega\nu\nu'}\right)^{-1}. \quad (3.81)$$

In order to incorporate the asymptotic bare (and local) Coulomb interaction  $\mathcal{U}_{1234;\sigma\sigma'}^{\text{asympt}}$  into the local irreducible vertex, we need to solve the  $n_{\text{asympt}}$ -size BSE,

$$\delta\Gamma_{1234;\sigma\sigma'}^{\text{core};\omega\nu\nu'} + \mathcal{U}_{1234;\sigma\sigma'}^{\text{asympt}} = \left(\chi_{1234;\sigma\sigma'}^{\text{asympt};\omega\nu\nu'}\right)^{-1} - \left(\chi_{0;1234}^{\text{asympt};\omega\nu\nu'}\right)^{-1}, \quad (3.82)$$

where  $\delta\Gamma_{1234;\sigma\sigma'}^{\text{core};\omega\nu\nu'}$  is the irreducible vertex minus the bare Coulomb interaction. Additionally,  $\chi_{1234;\sigma\sigma'}^{\text{asympt};\omega\nu\nu'}$  must equal the generalized susceptibility obtained from the impurity solver in the  $n_{\text{core}}$  region. Since we do not know how the generalized susceptibility behaves outside the core frequency region at this stage, this approach does not look promising. However, since we have fixed the irreducible vertex to the bare Coulomb interaction for high frequencies, we can obtain the local (corrected) irreducible vertex with the help of an intermediary susceptibility, where

$$\left(\tilde{\chi}_{1234;\sigma\sigma'}^{\text{asympt};\omega\nu\nu'}\right)^{-1} = \left(\chi_{0;1234}^{\text{asympt};\omega\nu\nu'}\right)^{-1} + \mathcal{U}_{1234;\sigma\sigma'}^{\text{asympt}}. \quad (3.83)$$

From the above two equations we can formulate the BSE as

$$\delta\Gamma_{1234;\sigma\sigma'}^{\text{core};\omega\nu\nu'} = \left(\chi_{1234;\sigma\sigma'}^{\text{asympt};\omega\nu\nu'}\right)_{\text{core}}^{-1} - \left(\tilde{\chi}_{1234;\sigma\sigma'}^{\text{asympt};\omega\nu\nu'}\right)_{\text{core}}^{-1}, \quad (3.84)$$

where after some rewriting and algebra [40]

$$\Gamma_{1234;\sigma\sigma'}^{\text{core};\omega\nu\nu'} + \mathcal{U}_{1234;\sigma\sigma'}^{\text{core}} = \left(\chi_{1234;\sigma\sigma'}^{\text{core};\omega\nu\nu'}\right)^{-1} - \left[\left(\tilde{\chi}_{1234;\sigma\sigma'}^{\text{asympt};\omega\nu\nu'}\right)_{\text{core}}\right]^{-1}. \quad (3.85)$$

We now have rewritten the irreducible vertex in terms of quantities that are already available from the impurity solver, such as  $\chi_{1234;\sigma\sigma'}^{\text{core};\omega\nu\nu'}$ , and the intermediate susceptibility, which is easily retrieved from the  $n_{\text{asympt}}$ -range bare bubble susceptibility and the bare Coulomb interaction. This can be seen as an asymptotic correction to the  $n_{\text{core}}$ -size BSE. Due to the frequency structure of  $\tilde{\chi}_{1234;\sigma\sigma'}^{\text{asympt};\omega\nu\nu'}$ , this does not require a lot of computational effort or memory and hence is a very resourceful approach.

The extension to non-local asymptotics is straightforward and can be derived in a few steps, where we will only outline the most important results. For a more in-depth discussion, we refer the reader to Ref. [40]. At the beginning, we define

$$\Gamma_{1234;\sigma\sigma'}^{X;\omega\nu\nu'} = \left(\chi_{1234;\sigma\sigma'}^{X;\omega\nu\nu'}\right)^{-1} - \left(\chi_{0;1234}^{X;\omega\nu\nu'}\right)^{-1} \quad \text{and} \quad (3.86)$$

$$\left(\chi_{1234;\sigma\sigma'}^{*;X;\omega\nu\nu'}\right)^{-1} = \left(\chi_{1234;\sigma\sigma'}^{X;\omega\nu\nu'}\right)^{-1} - \mathcal{U}_{1234;\sigma\sigma'}^X, \quad (3.87)$$

where  $X \in \{\text{core}, \text{asympt}\}$  and  $\chi_{1234;\sigma\sigma'}^{*;X;\omega\nu\nu'}$  is the same auxiliary susceptibility as already seen in Eq. (3.60). Both of these equations have to be satisfied for each frequency range  $n_X$ . From the lower equation we obtain

$$\chi_{1234;\sigma\sigma'}^{*;X;\text{qkk}'} = \chi_{1234;\sigma\sigma'}^{X;\text{qkk}'} + \sum_{\substack{k_1 k_2; \text{ab} \text{cd} \\ \sigma_1 \sigma_2}} \frac{\chi_{12\text{ba};\sigma\sigma_1}^{X;\text{qk}k_1} \mathcal{U}_{\text{ab} \text{cd};\sigma_1 \sigma_2}^{X;\text{qk}k_2} \chi_{\text{dc}34;\sigma_2 \sigma'}^{X;\text{qk}k_2'}}{\mathbb{1}_{1234} - \mathcal{U}_{12\text{ab};\sigma\sigma_1}^{X;\text{qk}k_1} \chi_{\text{ba}34;\sigma_1 \sigma'}^{X;\text{qk}k_2'}}. \quad (3.88)$$

From this one can arrive at an expression for the generalized physical susceptibility [40]

$$\chi_{1234;\sigma\sigma'}^{\text{core};q} = \sum_{\mathbf{k}\mathbf{k}'} \chi_{1234;\sigma\sigma'}^{\text{core};q\mathbf{k}\mathbf{k}'} = \sum_{\mathbf{k}\mathbf{k}'} \left[ \left( \chi_{1234;\sigma\sigma'}^{*,\text{core};q\mathbf{k}\mathbf{k}'} + \chi_{0;1234;\sigma\sigma'}^{\text{asympt};q\mathbf{k}\mathbf{k}'} - \chi_{0;1234;\sigma\sigma'}^{\text{core};q\mathbf{k}\mathbf{k}'} \right)^{-1} + \mathcal{U}_{1234;\sigma\sigma'}^{\text{core};q\mathbf{k}\mathbf{k}'} \right]^{-1}. \quad (3.89)$$

This is especially useful, since the generalized physical susceptibility enters the SDE (3.64) with the three-leg vertices of Eq. (3.63). Hence, this scheme proves to be powerful [40, 44] for this explicit form of the equation of motion of  $\Sigma_{12}^{\mathbf{k}}$ . Lastly, it can be shown [45], that for the three-leg vertex  $\gamma_{\text{d/m};1234}^{\text{qk}} \xrightarrow{\nu \rightarrow \infty} \mathbb{1}_{1234}$  holds.

### 3.7.3 High-frequency Bethe-Salpeter equation with vertex asymptotics

Sometimes it is convenient to separate low- and high-frequency components of a quantity to simplify calculations. Some DMFT solvers [46] employ such a frequency separation to calculate the self-energy: a high-frequency asymptotic expansion derived from the spectral function's lowest moments is incorporated in the numerical solution of the Dyson equation at low frequencies. Inspired by this idea, we can proceed similarly for the irreducible vertex  $\Gamma$ , working with the framework of the Bethe-Salpeter equation instead of the Dyson equation. By explicitly using the SU(2)-symmetric combinations d, m — in which the BSE for the ph-channel becomes diagonal<sup>[15]</sup> — we are able to reduce the computational effort by using a high-frequency expansion of the vertex functions. Following [34, 36, 38], the vertex in the low-frequency regime can be obtained by the regular BSE, where an additional high-frequency correction term is added. In the spirit of the end of Sec. 3.5, the BSE of Eq. (3.50) can be written as a matrix equation (in grouped indices nm) for spin combinations d, m in the following fashion

$$\chi^{\mathbf{q}} = \chi_0^{\mathbf{q}} - \frac{1}{\beta^2} \chi_0^{\mathbf{q}} \Gamma^{\mathbf{q}} \chi^{\mathbf{q}}. \quad (3.90)$$

Similar to Refs. [34, 36, 38], we will now split the matrices  $\mathbf{F}$ ,  $\mathbf{\Gamma}$  and  $\chi$  in segments of low and high frequencies. We will denote this by an additional superscript (L/H, L/H), where (L, L) denotes the segment, where  $\nu$  and  $\nu'$  are in the low frequency region and, e.g., (L, H) denotes the segment, where  $\nu$  is in the low- and  $\nu'$  in the high-frequency region. We will therefore construct a set of low frequencies  $\mathcal{I}_L$  and a set of high frequencies  $\mathcal{I}_H$ . This means, that for  $\mathbf{\Gamma}^{\text{LH}}$ ,  $\nu \in \mathcal{I}_L$  and  $\nu' \in \mathcal{I}_H$ . In the LH, HL and HH blocks, where atleast one frequency is considered large, we will employ explicit asymptotics for the vertex functions, as already discussed in Sec. 3.7. The goal is to calculate the vertex function with the BSE for the low-frequency region where we will expect a correction term arising from the low-frequency cutoff which employs the use of high-frequency blocks of the BSE components. The size of  $\mathcal{I}_L$  has to be atleast the number of bosonic Matsubara frequencies  $\omega$  [36] and might differ if non-local correlations are included [47]. Regarding  $\mathcal{I}_H$ , there is no minimum size and the maximum size of the high-frequency region is only bounded by the availability of computational resources and memory.

Using this idea, we will solve Eq. (3.90) for  $\mathbf{\Gamma}$  as

$$\begin{pmatrix} \mathbf{\Gamma}^{\text{LL}} & \mathbf{\Gamma}^{\text{LH}} \\ \mathbf{\Gamma}^{\text{HL}} & \mathbf{\Gamma}^{\text{HH}} \end{pmatrix} = \beta^2 \left[ \begin{pmatrix} \chi^{\text{LL}} & \chi^{\text{LH}} \\ \chi^{\text{HL}} & \chi^{\text{HH}} \end{pmatrix}^{-1} - \begin{pmatrix} \chi_0^{\text{LL}} & 0 \\ 0 & \chi_0^{\text{HH}} \end{pmatrix}^{-1} \right] \quad (3.91)$$

<sup>[15]</sup>The same can be done for the s, t combinations in the pp-channel, however only the ph-channel will be shown.

where we omitted frequency labels for brevity. Multiplying on the left by  $\chi$  and solving this matrix-like equation for  $\Gamma^{\text{LL}}$ , we find

$$\Gamma^{\text{LL}} = \beta^2 \left[ (\chi^{\text{LL}})^{-1} - (\chi_0^{\text{LL}})^{-1} \right] - (\chi^{\text{LL}})^{-1} \chi^{\text{LH}} \Gamma^{\text{HL}}, \quad (3.92)$$

with

$$\chi^{\text{LH}} = -\chi^{\text{LL}} \Gamma^{\text{LH}} \left[ \Gamma^{\text{HH}} + \beta^2 (\chi_0^{\text{HH}})^{-1} \right]^{-1}. \quad (3.93)$$

Combining these two equations yields for  $\Gamma^{\text{LL}}$

$$\Gamma^{\text{LL}} = \beta^2 \left[ (\chi^{\text{LL}})^{-1} - (\chi_0^{\text{LL}})^{-1} \right] + \Gamma^{\text{LH}} \left[ \Gamma^{\text{HH}} + \beta^2 (\chi_0^{\text{HH}})^{-1} \right]^{-1} \Gamma^{\text{HL}}. \quad (3.94)$$

The last term in the sum of Eq. (3.94) can be thought of as a correction to the inversion of the BSE in the low-frequency subspace, which otherwise reads

$$\Gamma^{\text{LL}} = \beta^2 \left[ (\chi^{\text{LL}})^{-1} - (\chi_0^{\text{LL}})^{-1} \right]. \quad (3.95)$$

The correction term can be obtained at a significantly lower cost compared to the full vertex — since for the high-frequency regimes of  $\Gamma$  we use either (i) kernel-1 and kernel-2 functions, which depend on one or two momentum and frequency dimensions less than the full vertex (or the generalized susceptibility), see Sec. 3.7.1 or (ii) the even more resourceful “U-range” approach of Sec. 3.7.2 — and is therefore easily available for much larger asymptotic frequency ranges. Other sets of equations for  $\Gamma^{\text{LL}}$ <sup>[16]</sup> can be acquired easily by manipulating the original BSE (3.90). These methods would require the calculation of the full vertex for a large frequency range<sup>[17]</sup>, which is more storage-heavy than the use of kernel-1 and kernel-2 functions or a padding of the bare Coulomb interaction. Thus, the approach outlined in this thesis is more efficient and is going to be a more practical one to use for multi-orbital calculations.

Since we have now assembled all necessary tools to describe the properties of correlated electrons on a lattice, let us introduce the D $\Gamma$ A’s purely local predecessor: the dynamical mean-field theory (DMFT).

### 3.8 Dynamical mean-field theory

Dynamical mean-field theory is based on the idea that in the limit of infinite spatial dimension ( $d \rightarrow \infty$ ), the self-energy  $\Sigma_{12}^k$  becomes *purely local*, i.e.,  $\Sigma_{\text{DMFT};12}^v = \delta_{12} \Sigma_{12}^v$  [48], where the Kronecker delta reduces the non-local self-energy to a purely local one<sup>[18]</sup>. The intuition behind this is that in high dimensions, an electron hops to many neighbors before returning, making non-local

<sup>[16]</sup> One can already use Eq. (3.92) instead of Eq. (3.94), cf. “Method 2” in Ref. [36].

<sup>[17]</sup> Retrieving the vertex functions in a high-frequency regime is *per se* not difficult; they can be obtained for arbitrary frequency ranges from the impurity solver of choice. However, the computing time increases drastically the larger the frequency box and thus this method is not preferred over the one mentioned above.

<sup>[18]</sup> Due to the spatial locality of the self-energy, a Fourier transform to momentum space results in a flat dispersion of  $\Sigma_{\text{DMFT}}^k$ .

correlations increasingly negligible<sup>[19]</sup>. Starting from this discovery, it was shown [49] that there is a connection between an auxiliary single-impurity Anderson model (SIAM) and the Hubbard model in infinite dimensions, which allowed for a derivation of a self-consistency cycle determining the purely local self-energy. This was crucial as people were able to solve the SIAM with existing numerical many-body algorithms, effectively solving the many-body problem in the DMFT framework. This can be done using approximate<sup>[20]</sup> and exact<sup>[21]</sup> methods [50, 51]. A modern DMFT solver — which is used in this thesis to calculate input data for the dynamical vertex approximation, more on that later — is w2dynamics [52], a continuous-time hybridization expansion (CT-HYB) QMC solver for the SIAM.

Let us briefly outline the idea and self-consistency equations of DMFT in the following, see [50] for a more in-depth discussion. In high spatial dimensions, the number of neighboring sites  $Z_{ij}$  grows as  $Z_{ij} \sim d$ . To ensure a well-defined competition between kinetic energy and Coulomb interaction, the hopping amplitudes must therefore scale as

$$t_{im,jn} \rightarrow t_{im,jn}^* = \frac{t_{im,jn}}{\sqrt{Z_{ij}}}, \quad (3.96)$$

where  $m, n$  denote source and target orbitals, respectively. Furthermore, the one-particle Green's function also has to be renormalized. It is written as

$$G_{12}^k = \left[ (i\nu + \mu)\delta_{12} - \varepsilon_{12}^k - \Sigma_{\text{DMFT};12}^\nu \right]^{-1}, \quad (3.97)$$

where the Fourier transforms of the hopping amplitudes  $\varepsilon_{12}^k$  enter the Green's function, hence it scales similarly.

Diagrammatically, DMFT includes the local contribution of all topologically inequivalent Feynman diagrams which can also be obtained via the SIAM, however only if the interaction of the SIAM Hamiltonian has the same form as the original Hubbard Hamiltonian,

$$\hat{\mathcal{H}}_{\text{AIM}} = \sum_{ab;k} \varepsilon_{ab}^k \hat{c}_{k,a}^\dagger \hat{c}_{k,b} + \sum_{ab} \varepsilon_{ab}^d \hat{d}_a^\dagger \hat{d}_b + \frac{1}{2} \sum_{abcd} u_{abcd} \hat{d}_a^\dagger \hat{d}_c^\dagger \hat{d}_b \hat{d}_d + \sum_{ab;k} \left[ V_{ab}^k \hat{d}_a^\dagger \hat{c}_{k,b} + \text{h.c.} \right]. \quad (3.98)$$

Here,  $\hat{d}_a^\dagger$  ( $\hat{d}_a$ ) creates (annihilates) an electron on the impurity, whereas the operators  $\hat{c}_{k,a}^\dagger$  ( $\hat{c}_{k,a}$ ) create (annihilate) bath — i.e., non-interacting conduction — electrons, which hybridize with the localized impurity electrons via  $V_{ab}^k$ . For a successful mapping of the Hubbard model onto the AIM, there are three distinct equations in DMFT that describe a self-consistency cycle [50]. One starts by “guessing” a local self-energy as a starting point and then iterates through the following set of equations until convergence:

$$G_{12}^\nu = \frac{1}{V_{\text{BZ}}} \int_{\text{BZ}} d\mathbf{k} \left[ (i\nu + \mu)\delta_{12} - \varepsilon_{12}^k - \Sigma_{\text{DMFT};12}^\nu \right]^{-1}, \quad (3.99a)$$

$$\mathcal{G}_{0;12}^\nu = \left[ \left( G_{12}^\nu \right)^{-1} + \Sigma_{\text{DMFT};12}^\nu \right]^{-1}, \quad (3.99b)$$

<sup>[19]</sup> Indeed, one can show, that the diagrams contributing to the non-local character (i.e. between lattice sites  $i$  and  $j$ ) of the self-energy are suppressed by  $\frac{1}{\sqrt{Z_{ij}}}$ , where  $Z_{ij}$  is the number of neighbors for a given distance  $\|\mathbf{R}_i - \mathbf{R}_j\|$  from lattice site  $i$ .

<sup>[20]</sup> e.g. self-consistent perturbation theory, iterated perturbation theory or non-crossing approximation

<sup>[21]</sup> e.g., quantum Monte Carlo (QMC), numerical renormalization group or even exact diagonalization

$$G_{12}^v = \langle \mathcal{T} \hat{d}_1 \hat{d}_2^\dagger \rangle \quad \text{and} \quad (3.99c)$$

$$\Sigma_{\text{DMFT};12}^v = \left( \mathcal{G}_{0;12}^v \right)^{-1} - \left( G_{12}^v \right)^{-1}. \quad (3.99d)$$

Here,  $\mathcal{G}_{0;12}^v$  denotes the local and non-interacting propagator of the impurity. The numerically challenging part is the computation of the AIM's Green's function in Eq. (3.99c) for which a number of different solvers are available, see the beginning of Sec. 3.8.

### 3.9 Dynamical vertex approximation

DMFT — as a local framework — is very capable of describing strong quasiparticle renormalization and the Mott-Hubbard metal-to-insulator transition in heavy fermion systems and transition metal oxides accurately. Its capabilities extend way beyond that, where successful descriptions of (anti-)ferromagnetic structure effects including metamagnetism, influence on ferromagnetic properties through the lattice and Hund's coupling, scattering at spins or impurities and many more have been reported [50, 53]. As wide as the range of DMFT's capabilities extends, it still comes with a major drawback: the exclusion of non-local correlations. Numerous scientific phenomena, including the formation of valence bonds, pseudogaps, and d-wave superconductivity, as well as (para-)magnons, quantum critical behavior, and generally the critical behavior in the proximity of phase transitions, are caused by such non-local correlations.

There are two main routes to extend DMFT beyond the local scope to also include non-local correlations [54] (i) cluster extensions and (ii) diagrammatic extensions. Cluster extensions make use of a small cluster of impurities that are embedded in a bath of non-interacting conduction electrons [55]. Non-local interaction effects within this cluster are then taken into account, making it possible to capture short-range fluctuations. Diagrammatic extensions on the other hand extend DMFT by explicitly adding non-local diagrammatic contributions. The dynamical vertex approximation falls into the latter one and will be in the main focus of this thesis, more specifically the self-consistent “ladder” variant [56]. For other flavors of D $\Gamma$ A, we refer the reader to Refs. [45, 57–63], which are all excellent reads. For a first introduction to the “standard” description of the dynamical vertex approximation, we refer the reader to Ref. [64].

Here, we will extend the original description by including the purely non-local Coulomb interaction to the irreducible vertex and follow the derivation outlined in Ref. [28] closely. For completeness, we will also derive the set of equations analogously to [44] for the case of non-local interactions. For brevity, we will govern those two separate derivation branches each their own section. The reason we include both derivations in this thesis is simple: Previously, we have written down two distinct ways to treat explicit vertex asymptotics. The first one, where explicit kernel-functions are used, see Sec. 3.7.1, works well if one explicitly employs the full vertex  $F$  in the equations, as [28] does. However, the second derivation, where we do not need the full vertex in the equations explicitly, benefits when treating vertex asymptotics with the “U-range” approach, see Sec. 3.7.2, since the numerical implementation of these asymptotics are more resourceful and one does not need local quantities on a very large frequency grid, i.e., it is easier to increase the size of the asymptotic range compared to the kernel-function approach.

The D $\Gamma$ A uses a converged DMFT solution, thus including all local diagrams. It then solves the

Schwinger-Dyson equation (3.56) using an approximated (full) vertex. We will show the “ladder”-approach, which reduces the numerical complexity by assuming locality of the pp-(ir-)reducible diagrams<sup>[22]</sup>. For the following, we assume that we already have an existing converged DMFT solution at hand, containing all local diagrams. The quantities we require for the execution of the dynamical vertex approximation are the DMFT self-energy, the local two-particle Green’s function and the local irreducible vertex in the particle-hole channel<sup>[23]</sup>.

At the heart of D $\Gamma$ A is the irreducible vertex in the particle-hole channel<sup>[24]</sup>, which we extend by the purely non-local Coulomb interaction,

$$\Gamma_{1234;\sigma\sigma'}^{\mathbf{q}\mathbf{k}\mathbf{k}'} = \Gamma_{1234;\sigma\sigma'}^{\omega\nu\nu'} + \mathcal{V}_{1234;\sigma\sigma'}^{\mathbf{q}\mathbf{k}\mathbf{k}'}, \quad (3.100)$$

where  $\mathcal{V}_{1234;\sigma\sigma'}^{\mathbf{q}\mathbf{k}\mathbf{k}'}$  is given by the crossing-symmetric expression (similar to Eq. (3.66))

$$\mathcal{V}_{1234;\sigma\sigma'}^{\mathbf{q}\mathbf{k}\mathbf{k}'} = V_{1234}^{\mathbf{q}} - \delta_{\sigma\sigma'} V_{1432}^{\mathbf{k}'-\mathbf{k}}. \quad (3.101)$$

This vertex can now be seen as containing all local irreducible diagrams plus the non-locality of the first order, providing a natural extension to this framework. This means that we have now included the first-order term — which is also the major contributor to the irreducible vertex — fully momentum-dependent. We will, similar to Ref. [28], exclude from now on the transversal particle-hole contribution to the non-local irreducible vertex in Eq. (3.100), similar to the GW approach [65], which will reduce the complexity of the D $\Gamma$ A equations considerably, since two out of three momentum indices vanish; the only leftover one from now on is the transfer momentum  $\mathbf{q}$ . This yields for the irreducible vertex in ph-channel for the d/m spin combinations

$$\Gamma_{\mathbf{d};1234}^{\mathbf{q}\nu\nu'} = \Gamma_{\mathbf{d};1234}^{\omega\nu\nu'} + 2V_{1234}^{\mathbf{q}} \quad \text{and} \quad (3.102a)$$

$$\Gamma_{\mathbf{m};1234}^{\mathbf{q}\nu\nu'} = \Gamma_{\mathbf{m};1234}^{\omega\nu\nu'}. \quad (3.102b)$$

From this, the Bethe-Salpeter equation in the ph-channel of Eq. (3.49) reduces to

$$F_{\mathbf{d}/\mathbf{m};1234}^{\mathbf{q}\nu\nu'} = \Gamma_{\mathbf{d}/\mathbf{m};1234}^{\mathbf{q}\nu\nu'} + \sum_{\mathbf{a}\mathbf{b}\mathbf{c}\mathbf{d};\nu_1} \Gamma_{\mathbf{d}/\mathbf{m};12\mathbf{a}\mathbf{b}}^{\mathbf{q}\nu_1\nu_1} \chi_{0;\mathbf{b}\mathbf{a}\mathbf{d}\mathbf{c}}^{\mathbf{q}\nu_1\nu_1} F_{\mathbf{d}/\mathbf{m};\mathbf{c}\mathbf{d}34}^{\mathbf{q}\nu_1\nu'}, \quad (3.103)$$

where

$$\chi_{0;1234}^{\mathbf{q}\nu\nu'} = \sum_{\mathbf{k}\mathbf{k}'} \chi_{0;1234}^{\mathbf{q}\mathbf{k}\mathbf{k}'} = -\beta \sum_{\mathbf{k}\mathbf{k}'} G_{14}^{\mathbf{k}} G_{32}^{\mathbf{k}'-\mathbf{q}}. \quad (3.104)$$

From now on we will sometimes work with grouped indices, as described at the end of Sec. 3.5, to simplify the following derivation of the D $\Gamma$ A equations. Notice that the grouped indices are now  $\{\mathbf{n}_1, \mathbf{n}_2, \nu\}$  and  $\{\mathbf{n}_3, \mathbf{n}_4, \nu'\}$ , respectively, and do not include any momenta anymore. We will denote quantities written in grouped indices as bold quantities, similar to before. We can now see that the

<sup>[22]</sup>This is not a priori justified, however, results of the full (parquet) D $\Gamma$ A equations yield a negligible contribution of the particle-particle channel to the full vertex  $F$  in the presence of strong spin fluctuations close to the antiferromagnetic phase transition in two dimensions [60]. It is therefore reasonable to neglect the non-locality of the particle-particle channel diagrams. For superconducting properties on the other hand, these non-local diagrams are often essential.

<sup>[23]</sup>For the asymptotics of the vertex functions as described in Sec. 3.7.1, we also require the local two-particle Green’s function in the ph-channel.

<sup>[24]</sup>From now on, if not explicitly specified otherwise, we will always assume the frequency notation and channel reducibility to be particle-hole like.



numerical implementation of the D $\Gamma$ A equations is easier, since the vertex matrices decrease in size from  $(N_k \cdot N_v \cdot N_{\text{bands}}^2) \times (N_k \cdot N_v \cdot N_{\text{bands}}^2) \rightarrow (N_v \cdot N_{\text{bands}}^2) \times (N_v \cdot N_{\text{bands}}^2)$ , which reduces the storage capacity by  $N_k^2$  and the number of operations by  $N_k^2$  for matrix multiplication and  $N_k^3$  for matrix inversion compared to the full parquet approach.

In principle, it would be straightforward to retrieve the full vertex via  $\mathbf{F}_r^q = [(\mathbf{\Gamma}_r^q)^{-1} - \chi_0^q]^{-1}$  from Eq. (3.90). This poses numerical problems, as already stated at the end of Sec. 3.6. Thus, we rewrite the inversion of the irreducible vertex  $\mathbf{\Gamma}$  using the local variant of Eq. (3.49) and Eq. (3.102),

$$\mathbf{\Gamma}_d^q = \frac{\mathbf{F}_d^\omega}{\mathbb{1} + \chi_0^\omega \mathbf{F}_d^\omega} + 2\mathbf{V}^q \quad \text{and} \quad (3.105a)$$

$$\mathbf{\Gamma}_m^q = \frac{\mathbf{F}_m^\omega}{\mathbb{1} + \chi_0^\omega \mathbf{F}_m^\omega}, \quad (3.105b)$$

where  $\mathbb{1}$  is an identity matrix in grouped index space. After some algebra, the full vertex in the density and magnetic spin combinations reads

$$\mathbf{F}_d^q = [\mathbf{F}_d^\omega + 2\mathbf{V}^q (1 + \chi_0^\omega \mathbf{F}_d^\omega)] [\mathbb{1} - \chi_0^{\text{nl};q} \mathbf{F}_d^\omega - 2\chi_0^q \mathbf{V}^q (1 + \chi_0^\omega \mathbf{F}_d^\omega)]^{-1} \quad \text{and} \quad (3.106a)$$

$$\mathbf{F}_m^q = \mathbf{F}_m^\omega [\mathbb{1} - \chi_0^{\text{nl};q} \mathbf{F}_m^\omega]^{-1}. \quad (3.106b)$$

Here, the purely non-local susceptibility  $\chi_0^{\text{nl};q}$  is given by

$$\chi_0^{\text{nl};q} = \chi_0^q - \chi_0^\omega. \quad (3.107)$$

Rewriting the full vertex this way avoids the aforementioned numerical difficulties that lie in the inversion of the irreducible vertex  $\mathbf{\Gamma}$ , however we still have to deal with the inclusion of the transversal particle-hole channel, since the above equations were generated though the BSE (3.49) in the ph-channel only. The BSE only carries over the swapping symmetry of the two-particle Green's function to the (ir-)reducible vertices  $\mathbf{\Gamma}$  and  $\mathbf{\Phi}$ . The crossing symmetry of the full vertex can be restored by explicitly adding diagrams that belong to the transversal particle-hole channel. We therefore modify the parquet-decomposition in Eq. (3.33) in the following way

$$\mathbf{F}_{d;1234}^{\text{qkk}'} = \mathbf{F}_{d;1234}^{\omega\text{vv}'} + 2\mathbf{V}_{1234}^q + (\Phi_{d;1234}^{\text{qv}v'} - \Phi_{d;1234}^{\omega\text{vv}'} + (\Phi_{d;\text{ph};1234}^{\text{qkk}'} - \Phi_{d;\text{ph};1234}^{\omega\text{vv}'})) \quad \text{and} \quad (3.108)$$

$$\mathbf{F}_{m;1234}^{\text{qkk}'} = \mathbf{F}_{r;1234}^{\omega\text{vv}'} + (\Phi_{m;1234}^{\text{qv}v'} - \Phi_{m;1234}^{\omega\text{vv}'} + (\Phi_{m;\text{ph};1234}^{\text{qkk}'} - \Phi_{m;\text{ph};1234}^{\omega\text{vv}'})). \quad (3.109)$$

Here, all diagrams in the pp-channel and all fully irreducible diagrams (except the bare interaction  $\mathbf{V}_{r;1234}^q$ ) are local. We furthermore find via the local and non-local BSE,

$$(\Phi_{d;1234}^{\text{qv}v'} - \Phi_{d;1234}^{\omega\text{vv}'} = \mathbf{F}_{d;1234}^{\text{nl;qv}v'} - 2\mathbf{V}_{1234}^q \quad \text{and} \quad (3.110a)$$

$$(\Phi_{m;1234}^{\text{qv}v'} - \Phi_{m;1234}^{\omega\text{vv}'} = \mathbf{F}_{m;1234}^{\text{nl;qv}v'}, \quad (3.110b)$$

where  $\mathbf{F}_{r;1234}^{\text{nl;qv}v'}$  is defined analogously to the purely non-local susceptibility

$$\mathbf{F}_{r;1234}^{\text{nl;qv}v'} = \mathbf{F}_{r;1234}^{\text{qv}v'} - \mathbf{F}_{r;1234}^{\omega\text{vv}'} \quad (3.111)$$

We can express the difference of the transversal particle-hole diagrams of Eq. (3.108) with the help of Eq. (3.37), yielding

$$\left( \Phi_{d;ph;1234}^{qkk'} - \Phi_{d;ph;1234}^{\omega vv'} \right) = -\frac{1}{2} F_{d;3214}^{nl;(k'-k)(v'-\omega)v'} - \frac{3}{2} F_{m;3214}^{nl;(k'-k)(v'-\omega)v'} \quad \text{and} \quad (3.112a)$$

$$\left( \Phi_{m;ph;1234}^{qkk'} - \Phi_{m;ph;1234}^{\omega vv'} \right) = -\frac{1}{2} F_{m;3214}^{nl;(k'-k)(v'-\omega)v'} + \frac{1}{2} F_{m;3214}^{nl;(k'-k)(v'-\omega)v'}. \quad (3.112b)$$

We can combine the results of Eq. (3.108) which now states

$$F_{d;1234}^{qkk'} = F_{d;1234}^{\omega vv'} + F_{d;1234}^{nl;qvv'} - \frac{1}{2} F_{d;3214}^{nl;(k'-k)(v'-\omega)v'} - \frac{3}{2} F_{m;3214}^{nl;(k'-k)(v'-\omega)v'} \quad \text{and} \quad (3.113a)$$

$$F_{m;1234}^{qkk'} = F_{m;1234}^{\omega vv'} + F_{m;1234}^{nl;qvv'} - \frac{1}{2} F_{d;3214}^{nl;(k'-k)(v'-\omega)v'} + \frac{1}{2} F_{m;3214}^{nl;(k'-k)(v'-\omega)v'}. \quad (3.113b)$$

Within the approximations introduced above, the connected part of the self-energy (see Eq. (3.56) and below) loses the momentum-dependent contribution from the non-local bare interaction  $V_{1234}^{k'-k}$  and now reads

$$\Sigma_{12}^k = \Sigma_{HF;12}^k - \frac{1}{\beta} \sum_{\substack{abcd \in f \\ qv'}} \left[ \mathcal{U}_{a1bc}^q \chi_{0;cbe d}^{qv'v'} F_{d;de2f}^{qv'v'} - \frac{1}{2} \tilde{\mathcal{U}}_{a1bc} \chi_{0;cbe d}^{qv'v'} \left[ F_{d;de2f}^{nl;qv'v'} + 3F_{m;de2f}^{nl;qv'v'} \right] \right] G_{af}^{k-q}. \quad (3.114)$$

It is now time to split up the derivation in two paths, one devoted to the steps outlined in [28], coined “Approach 1”, and one devoted to the steps outlined in [44], coined “Approach 2”.

**Approach 1** — From the purely local part of Eq. (3.114), which is contained in the first term in the brackets, one can extract the DMFT self-energy, since the ph-channel contribution with the local  $\mathcal{U}_{1234}$  can be rewritten as

$$\Sigma_{ph;\mathcal{U};12}^k = \Sigma_{HF;12}^k - \frac{1}{\beta} \sum_{qv'} \mathcal{U}_{a1bc} \left( \chi_{0;cbe d}^{nl;qv'v'} + \chi_{0;cbe d}^{\omega v'v'} \right) F_{d;de2f}^{\omega v'v'} G_{af}^{k-q} \quad (3.115)$$

$$= \Sigma_{DMFT;12}^v + \Sigma_{HF;12}^{nl;k} - \frac{1}{\beta} \sum_{qv'} \mathcal{U}_{a1bc} \chi_{0;cbe d}^{nl;qv'v'} F_{d;de2f}^{\omega v'v'} G_{af}^{k-q}, \quad (3.116)$$

where  $\Sigma_{HF;12}^{nl;k}$  is the purely non-local Hartree-Fock term with the contributions from  $V_{1234}^q$  but not  $\mathcal{U}_{1234}$ , see Eq. (3.56). We can take advantage of the momentum and frequency structure in the SDE above to simplify the numerical calculation of the self-energy. Therefore, we — in analogy to Ref. [28] — define three Hedin vertices in  $r \in \{d, m\}$  spin combinations,

$$\zeta_{r;1234}^{\omega v} = \sum_{ab;v'} \chi_{0;12ab}^{\omega v'v'} F_{r;ba34}^{\omega v'v'}, \quad (3.117)$$

$$\zeta_{r;1234}^{qv} = \sum_{ab;v'} \chi_{0;12ab}^{nl;qv'v'} F_{r;ba34}^{\omega v'v'} \quad \text{and} \quad (3.118)$$

$$\xi_{r;1234}^{qv} = \sum_{ab;v'} \left[ \chi_{0;12ab}^{qv'v'} F_{r;ba34}^{qv'v'} - \chi_{0;12ab}^{\omega v'v'} F_{r;ba34}^{\omega v'v'} \right]. \quad (3.119)$$

The completely local Hedin vertex can straightforwardly be retrieved from DMFT. The vertex  $\xi_{1234}^{qv}$  in spin combinations d/m can be calculated efficiently with a matrix inversion

$$\xi_d^q = \left( \vec{1} + \zeta_d^\omega \right) \left( \left[ \vec{1} - \chi_0^{nl;q} F_d^\omega - 2\chi_0^q V^q \left( \vec{1} + \zeta_d^\omega \right) \right]^{-1} - \vec{1} \right) \quad \text{and} \quad (3.120a)$$



$$\xi_m^q = (\vec{1} + \zeta_m^\omega) \left( [\mathbb{1} - \chi_0^{nl;q} \mathbf{F}_m^\omega]^{-1} - \mathbb{1} \right), \quad (3.120b)$$

where  $\vec{1}_{1234} = \delta_{14}\delta_{23}$ , contrary to  $\mathbb{1}$ , which is given by  $\mathbb{1}_{1234}^{vv'} = \delta_{14}\delta_{23}\delta_{vv'}$ . Combining these expressions and simplifying it [28] yields the D $\Gamma$ A self-energy

$$\begin{aligned} \Sigma_{D\Gamma A}^k &= \Sigma_{DMFT}^v + \Sigma_{HF}^{nl;k} - \frac{1}{\beta} \sum_q \left( U + V^q - \frac{\tilde{U}}{2} \right) \xi_d^q G^{k-q} \\ &\quad + \frac{3}{2\beta} \sum_q \tilde{U} \xi_m^q G^{k-q} - \frac{1}{\beta} \sum_q (V^q \zeta_d^\omega - U \zeta_d^q) G^{k-q}. \end{aligned} \quad (3.121)$$

**Approach 2** — For an alternative formulation using the three-leg vertices already derived in Sec. 3.6, see Eq. (3.63), we have to rewrite Eq. (3.114) with the full ladder vertices  $F_{d/m;1234}^{qv'v}$ ,

$$F_{d/m;1234}^{nl;qv'v} = F_{d/m;1234}^{qv'v} - F_{d/m;1234}^{\omega v'v}, \quad (3.122)$$

such that

$$\Sigma_{12}^k = \Sigma_{HF;12}^k - \frac{1}{\beta} \sum_{\substack{abcde f \\ qv'}} \left[ \mathcal{U}_{a1bc}^q \chi_{0;cbe d}^{qv'v'} F_{d;de2f}^{qv'v} - \frac{1}{2} \tilde{\mathcal{U}}_{a1bc} \chi_{0;cbe d}^{qv'v'} \left[ F_{d;de2f}^{qv'v} + 3F_{m;de2f}^{qv'v} \right] \right] G_{af}^{k-q} - \Sigma_{dc;12}^k, \quad (3.123)$$

where  $\Sigma_{dc;12}^k$ , which is merely a double-counting correction, is given by

$$\Sigma_{dc;12}^k = \frac{1}{2\beta} \sum_{\substack{abcde f \\ qv'}} \tilde{\mathcal{U}}_{a1bc} \chi_{0;cbe d}^{qv'v'} \left[ F_{d;de2f}^{\omega v'v} + 3F_{m;de2f}^{\omega v'v} \right] G_{af}^{k-q}. \quad (3.124)$$

With the definition of the three-leg vertex from Eq. (3.63), we can write the upper equation as

$$\begin{aligned} \Sigma_{D\Gamma A;12}^k &= \Sigma_{HF;12}^k - \frac{1}{2} \sum_{\substack{q;abc d \\ e f g h}} \left[ \mathcal{U}_{d;a1bc}^q \gamma_{d;cbe d}^{qv} \left( \mathbb{1}_{de2h} - \mathcal{U}_{d;de f g}^q \chi_{d;gf2h}^q \right) \right. \\ &\quad \left. + 3\mathcal{U}_{m;a1bc}^q \gamma_{m;cbe d}^{qv} \left( \mathbb{1}_{de2h} - \mathcal{U}_{m;de f g}^q \chi_{m;gf2h}^q \right) - 2\mathcal{U}_{m;a12h}^q \right] G_{ah}^{k-q} - \Sigma_{dc;12}^k \\ &= \Sigma_{HF;12}^k - \frac{1}{2} \sum_{\substack{q;abc d \\ e f g h}} \left[ \left( 2\mathcal{U}_{a1bc} + 2V_{a1bc}^q - \mathcal{U}_{ac b1} \right) \gamma_{d;cbe d}^{qv} \times \right. \\ &\quad \times \left( \mathbb{1}_{de2h} - \left( 2\mathcal{U}_{de f g} + 2V_{de f g}^q - \mathcal{U}_{dg f e} \right) \chi_{d;gf2h}^q \right) \\ &\quad \left. - 3\mathcal{U}_{ac b1} \gamma_{m;cbe d}^{qv} \left( \mathbb{1}_{de2h} + \mathcal{U}_{dg f e} \chi_{m;gf2h}^q \right) + 2\mathcal{U}_{ah21} \right] G_{ah}^{k-q} - \Sigma_{dc;12}^k. \end{aligned} \quad (3.125)$$

### 3.10 Self-consistent dynamical vertex approximation

The self-energy obtained from a simple “one-shot” calculation with the ladder-D $\Gamma$ A does not (always) show the correct asymptotic behavior. This deficiency is even more pronounced for higher values of the physical susceptibilities [56]. In addition, the susceptibilities that can be derived from the full vertex diverge at the DMFT Néel temperature. This is concerning, since it therefore violates the Mermin-Wagner theorem [66] for the case of two-dimensional systems. This can be resolved by applying a so-called  $\lambda$ -correction [67], where enforcing a specific sum rule of the spin (and charge) susceptibilities yields a renormalization parameter  $\lambda$ , which is in turn used to renormalize physical susceptibilities in the D $\Gamma$ A routine.

The formalism for the  $\lambda$ -correction is currently only viable in the one-band regime, a straightforward extension to multi-orbital systems has not been discovered yet. The reasons being (i)  $\lambda$  would become a matrix object with as many entries as spin-orbit combinations exist, yielding a multidimensional optimization problem; and (ii) the solution of this multidimensional problem can be non-unique and there is no rules of which of these solutions to choose, hence the approach using a regularization scheme with the help of a  $\lambda$ -correction is not suitable for multi-orbital systems, which are in the focus of this thesis. Therefore, to “repair” the violation of the Mermin-Wagner theorem, we will employ a different scheme, a so-called self-consistency iteration, more on that later.

Since the  $\lambda$ -correction is currently not possible for multi-band systems, simply using a non-renormalized one-shot ladder-D $\Gamma$ A calculation might be a first approach. However, this comes with major drawbacks: it lacks viable descriptions in parameter regimes where non-local corrections are large [56], e.g., where the DMFT susceptibilities diverge due to a phase transition. The source of this is two-fold: (i) due to the assumed locality of the particle-particle reducible diagrams in the ladder-D $\Gamma$ A equations, which would dampen the particle-hole fluctuations [68], the ladder diagrams of the particle-hole channel lack non-local contributions; and (ii) the self-energy entering the Bethe-Salpeter equations would still only be the local DMFT self-energy. Hence any non-local contributions in that regard are simply missing. These two problems can be solved by applying a self-consistency scheme within the D $\Gamma$ A equations as shown in Fig. 3.17. The steps to acquire a converged D $\Gamma$ A routine with an appropriate self-energy and vertex functions are as follows:

1. First, a bunch of preprocessing has to be done before the actual D $\Gamma$ A equations can be iterated self-consistently. At first, the method requires the calculated bandstructure  $\epsilon_{12}^k$  and the (non-local) interaction  $U_{1234}^a$  performed with DFT and/or cRPA, respectively. Using the momentum-dependent bandstructure and the (non-local) interaction, a DMFT calculation with the impurity solver of choice is performed. After the DMFT calculation is converged, the necessary local one- and two-particle quantities, such as the local self-energy and certain local vertex functions, are extracted. All of these aforementioned quantities serve as the input for the following D $\Gamma$ A calculation.
2. The first step in the sc-D $\Gamma$ A routine is the calculation of the one-particle Green’s function via the Dyson equation (3.18). This is done with the local self-energy from DMFT in the first iteration and then with the non-local self-energy calculated from the non-local SDE of the previous iteration.
3. The next step is to update the chemical potential from the newly acquired Green’s function, since the eigenenergies of the particles are subject to change and the underlying Fermi-Dirac distribution needs to be adapted accordingly.

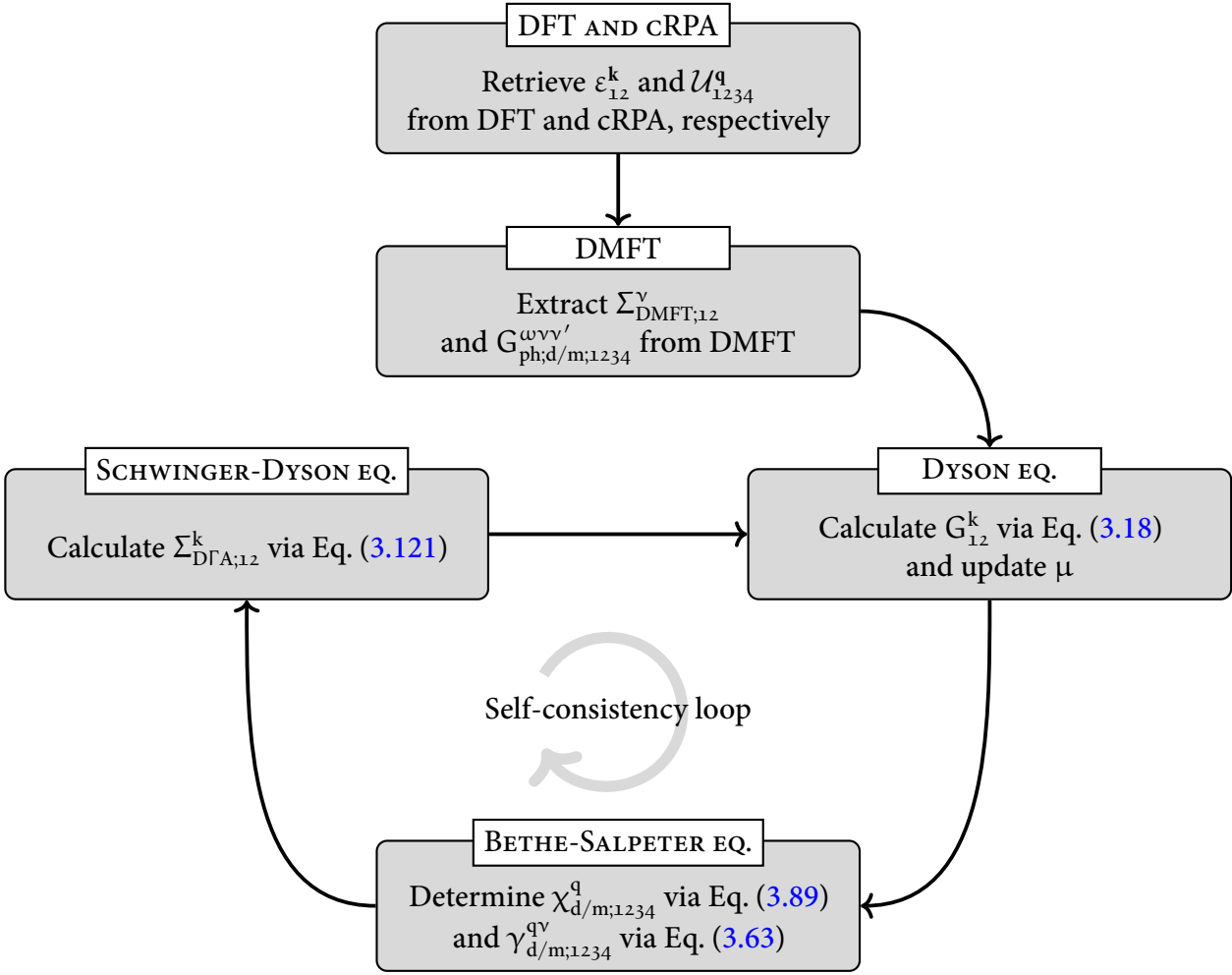


**FIGURE 3.17** – This flowchart shows the D $\Gamma$ A self-consistency cycle. The first box is concerned with the bandstructure and interaction calculations using DFT and/or cRPA. The next box denotes the DMFT calculation which is performed using the previously calculated quantities. From the converged DMFT calculation we extract the DMFT self-energy and local two-particle vertex functions, such as the two-particle Green’s function in the ph and pp-channel. The three boxes below describe the self-consistency cycle of the D $\Gamma$ A approach. The output quantities from DFT/cRPA and DMFT, i.e. all purely local vertex functions and the interaction, are kept constant throughout the D $\Gamma$ A self-consistency cycle.

4. We then proceed with the calculation of the necessary (non-local) three-leg vertices, see Eq. (3.63), and the generalized physical susceptibility from Eq. (3.89).
5. To complete the cycle, the self-energy of the current iteration is finally calculated via Eq. (3.121) using the previously acquired vertex functions and susceptibilities. The self-energy then enters the Green’s function again via the Dyson equation, see step 2. To ensure a steady convergence, the self-energy that enters the Green’s function is either mixed linearly with a parameter  $\alpha$ , such that  $\Sigma_n = \alpha \Sigma_n + (1 - \alpha) \Sigma_{n-1}$ , where  $n$  denotes the iteration number and  $\alpha$  is typically chosen around 0.2 – 0.4 or with other mixing schemes, such as Periodic Pulay mixing

[69]. This accelerated and predictive mixing scheme has been used previously in numerical calculations [70] with significant improvement in convergence speed and behavior over the linear mixing strategy, despite the additional computational and storage cost. To determine whether the self-energy is converged or not, a simple criteria comparing the magnitude of the self-energy from the previous iteration and the current iteration is used.

6. Once the non-local self-energy within the dynamical vertex approximation is converged, some postprocessing steps are typically executed.

To connect the aforementioned one- and two-particle vertex functions to quantities we can measure experimentally<sup>[25]</sup>, we can insert the Green's functions and certain vertex functions into further diagrammatic methods that are able to describe, for example, superconducting phase transitions and electron-pairing symmetry via the Eliashberg equation.

### 3.11 Eliashberg equation

After a successful converged ladder-DΓA routine, we have the most important non-local one- and two-particle quantities available. Starting from this, we can further study superconductivity with the so-called Eliashberg equations [71, 72], an extensive diagrammatic framework based upon particle-particle interactions that lead to the formation of Cooper pairs. Due to the coupling of electrons, we introduce, additionally to the one-particle Green's function of Eq. (3.1), two *anomalous* Green's functions [73]

$$F_{12}^k = -\langle \mathcal{T} [\hat{c}_{k,1} \hat{c}_{-k,2}] \rangle \quad \text{and} \quad (3.126a)$$

$$\bar{F}_{12}^k = -\langle \mathcal{T} [\hat{c}_{k,1}^\dagger \hat{c}_{-k,2}^\dagger] \rangle. \quad (3.126b)$$

Here,  $F_{12}^k$  and  $\bar{F}_{12}^k$  are not to be confused with the full vertex  $F_{1234}^{qkk'}$ . The anomalous Green's functions are rather unusual contractions of either two electrons or two holes, contrary to the regular Green's function, which is a contraction of an electron and a hole. These two contractions will vanish in the normal state, however they are of finite value in the superconducting phase.

At this point it is helpful to switch to the Nambu formalism [26], where the basis is spanned by the spinors

$$\hat{\psi}_1^k = \left( \hat{c}_{k,1,\uparrow}, \hat{c}_{k,1,\downarrow}, \hat{c}_{-k,1,\uparrow}^\dagger, \hat{c}_{-k,1,\downarrow}^\dagger \right)^T. \quad (3.127)$$

In this basis, the anomalous Green's functions are (block-)off-diagonal entries of the (generalized) Gro'kov single-particle propagator [74, 75]

$$\begin{aligned} \hat{G}_{12}^k &= -\langle \mathcal{T} [\hat{\psi}_1^k \hat{\psi}_2^{k\dagger}] \rangle \\ &= \begin{pmatrix} G_{12}^k & -F_{12}^k \\ -\bar{F}_{12}^k & \bar{G}_{12}^k \end{pmatrix}, \end{aligned} \quad (3.128)$$

where  $G_{12}^k$  and  $F_{12}^k$  are  $2n \times 2n$  matrices in spin-orbital space, where  $n$  denotes the number of bands. The diagonal entries of the Gro'kov single-particle propagator are the regular single-particle ( $G_{12}^k$ )

<sup>[25]</sup>Aside from the imaginary part of the retarded Green's function, which is directly connected to the spectral function and is measurable with, e.g., ARPES.

and single-hole ( $\bar{G}_{12}^k = -G_{12}^{-k}$ ) propagators. After a Fourier transform to Matsubara frequencies, the generalized Dyson equation can be written as follows:

$$\hat{G}_{12}^k = \hat{G}_{0;12}^k + \sum_{ab} \hat{G}_{0;1a}^k \hat{\Sigma}_{ab}^k \hat{G}_{b2}^k, \quad (3.129)$$

where

$$\hat{G}_{0;12}^k = \begin{pmatrix} G_{0;12}^k & 0 \\ 0 & G_{0;12}^k \end{pmatrix} \quad (3.130)$$

is the non-interacting generalized propagator and

$$\hat{\Sigma}_{12}^k = \begin{pmatrix} \Sigma_{12}^k & \Delta_{12}^k \\ \bar{\Delta}_{12}^k & \bar{\Sigma}_{12}^k \end{pmatrix} \quad (3.131)$$

denotes the generalized self-energy, where the diagonal entries  $\Sigma_{12}^k$  and  $\bar{\Sigma}_{12}^k$  are the single-particle and single-hole self-energies, respectively and the off-diagonal *pairing* function  $\Delta_{12}^k$  is coined the superconducting *gap function*.  $\Delta_{12}^k$  is directly connected to the anomalous propagators and therefore can capture the relevant Cooper-pairing nature of the electrons in the superconducting phase. While the gap function is non-zero only in the superconducting phase, it is nevertheless possible to obtain a solution directly from the normal state: The phase transition from the normal to the superconducting state is characterized by a divergence in the respective particle-particle susceptibility, which results in an eigenvalue problem also known as the Eliashberg equation [76]. We will start with the BSE written in terms of singlet and triplet susceptibilities in the particle-particle channel, see Eq. (3.50c),

$$\chi_{s/t;1234}^{qkk'} = \chi_{s/t;0;1234}^{qkk'} - \frac{1}{2\beta^2} \sum_{k_1 k_2; abc\bar{d}} \chi_{s/t;0;1c3a}^{qkk_1} \Gamma_{s/t;abc\bar{d}}^{qk_1 k_2} (\chi_{s/t;\bar{d}2b4}^{qk_2 k'} + \chi_{s/t;0;\bar{d}2b4}^{qk_2 k'}), \quad (3.132)$$

where the bare bubble susceptibility in the singlet and triplet channel is given by [77]

$$\chi_{s/t;0;1234}^{qkk'} = \mp \chi_{0;1234}^{qkk'}. \quad (3.133)$$

When describing the superconducting state, one usually employs quantities written in the Nambu basis, i.e., we are now using the generalized Gro'kov single-particle propagator in the equation for the susceptibility, not the regular Green's function [26, 78]. We will denote these Green's functions by an additional superscript,  $G_{12}^{sc;k}$ , and call them *superconducting* Green's functions. The corresponding Eliashberg equation can then be written as

$$\lambda_{s/t} \Delta_{s/t;12}^k = \pm \frac{1}{2} \sum_{k_1 k_2; abc\bar{d}} \Gamma_{s/t;1b2a}^{qkk_1} \chi_{s/t;0;ac\bar{b}\bar{d}}^{sc;qk_1 k_2} \Delta_{s/t;\bar{d}c}^{k_2}, \quad (3.134)$$

yielding an eigenvalue problem with  $\lambda_{s/t}$  as the corresponding eigenvalue. The irreducible vertex  $\Gamma_{s/t;1234}^{qkk'}$  appearing in Eq. (3.134) describes the scattering of two electrons with spin-orbit index 1, 2 and momenta  $(k + q, -k)$  to electrons with spin-orbit index 3, 4 and momenta  $(k' + q, -k')$ . Here, the bare bubble susceptibility  $\chi_{0;1234}^{sc;qkk'}$  is now built from the superconducting Green's function  $G_{12}^{sc;k}$  and therefore contains the anomalous self-energy in the following form

$$G_{12}^{sc;k} = \frac{i\nu\delta_{12} + \varepsilon_{12}^k + \Sigma_{12}^k}{(i\nu\delta_{12} + \varepsilon_{12}^k + \Sigma_{12}^k)(i\nu\delta_{12} + \varepsilon_{12}^k - \Sigma_{12}^k) - |\Delta_{12}^k|^2}, \quad (3.135)$$

which results from the generalized Dyson equation of Eq. (3.129)<sup>[26]</sup>. A divergence of  $\chi_{s/t;1234}^{qkk'}$  is associated with the largest eigenvalue of  $-\Gamma_{s/t;1b2a}^{qkk_1} \chi_{s/t;0;acb\delta}^{sc;qk_1k_2}$  becoming unity. In other words: When the temperature is lowered, the superconducting instability takes place at  $T_c$ , where  $\lambda_{s/t} \rightarrow 1$ <sup>[27]</sup>. Eq. (3.134) is the full Eliashberg equation, which represents a non-linear implicit equation for the superconducting gap function  $\Delta_{12}^k$ . To solve this equation numerically, one often linearizes the Eliashberg equation and neglects the gap function in the denominator of the superconducting Green's function. This is then commonly coined the *linearized* Eliashberg equation and reads

$$\lambda_{s/t} \Delta_{s/t;12}^k = \pm \frac{1}{2} \sum_{k_1 k_2; abcd} \Gamma_{s/t;1b2a}^{qkk_1} \chi_{s/t;0;acb\delta}^{qk_1k_2} \Delta_{s/t;\delta c}^{k_2}, \quad (3.136)$$

where the superconducting Green's function transitions to the regular Green's function for a vanishing  $\Delta_{12}^k$ . Eq. (3.136) is diagrammatically depicted for the case  $q = 0$  in Fig. 3.18. Choosing this single point of vanishing transfer momentum simplifies the problem, as Cooper pairs form at zero total energy (i.e., in the centre-of-mass system), making the equation effectively static (c.f. Migdal-Eliashberg theory). Finite  $q$  can indicate competing (pair-)density wave states, i.e., charge density waves or spin density waves [79].

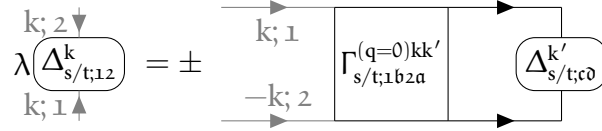


FIGURE 3.18 – Linearized Eliashberg equation for vanishing transfer frequency  $q = 0$ , see Eq. (3.136).

Due to Pauli's principle requiring  $\Delta$  to be antisymmetric under the exchange of two particles, the combined symmetry operation of (i) spin flip ( $\hat{S}; \sigma \rightarrow \bar{\sigma}$ ), (ii) parity ( $\hat{P}; \mathbf{k} \rightarrow -\mathbf{k}$ ), (iii) orbital exchange ( $\hat{O}; n_1 \leftrightarrow n_2$ ) and (iv) time reversal ( $\hat{T}; \nu \rightarrow -\nu$ ) has to yield [80]

$$\hat{S}\hat{P}\hat{O}\hat{T}\Delta_{12}^k = -\Delta_{21}^{-k}. \quad (3.137)$$

The pairing type of the Cooper pairs can be uniquely determined by individually applying the symmetry operations (i)-(iv). The (anti-)symmetric behavior of  $\Delta_{12}^k$  under these operations of course limits the solutions of the linearized Eliashberg equations to a small subset, which is important to be aware of when solving them numerically. Additionally, the corresponding gap function for singlet pairing fulfills  $\Delta_{12}^k = \Delta_{21}^{-k}$ , whereas the corresponding gap function for triplet pairing fulfills  $\Delta_{12}^k = -\Delta_{21}^{-k}$  [81].

If the largest eigenvalues of  $M = -F\chi$  are non-degenerate, one can solve the linearized Eliashberg equation through a power iteration, e.g., a Lanczos algorithm. For a converged solution, one specifies a starting eigenvalue  $\lambda_0$  and normalized gap function  $\Delta_0$  and then iterates through the following equations self-consistently:

$$\Delta_n = M\Delta_{n-1}, \quad (3.138a)$$

<sup>[26]</sup>  $\Delta_{s/t;12}^k$ , as already mentioned above, is the superconducting gap function that transitions smoothly into the anomalous self-energy below the critical temperature  $T_c$ .

<sup>[27]</sup> One way to find  $T_c$  numerically is via the evolution of  $\lambda_{s/t}$ : One often calculates the superconducting eigenvalue for a few (low) temperature regimes and extrapolates it to the region of  $\lambda_{s/t} \rightarrow 1$ .

$$\Delta_n = \frac{\Delta_n}{\|\Delta_n\|} \quad \text{and} \quad (3.138b)$$

$$\lambda_n = \Delta_n^\dagger M \Delta_n, \quad (3.138c)$$

where  $n$  denotes the iteration number. Solving this set of equations is not difficult, the computationally demanding part of solving the linearized Eliashberg equation is the calculation of the irreducible vertex in the particle-particle channel. Following the derivation outlined in the supplemental material of [82] and generalizing the equations to account for multiple orbitals yields for the full vertex in ladder-D $\Gamma$ A for  $r \in \{d/m\}$  spin combinations

$$\begin{aligned} F_{r,1234}^{qv v'} = & \beta^2 \left[ \left( \chi_{0;1234}^{qv v'} \right)^{-1} - \sum_{v_1 v_2; abcd} \left( \chi_{0;12ba}^{qv v_1} \right)^{-1} \chi_{r;abcd}^{*;qv_1 v_2} \left( \chi_{0;dc34}^{qv_2 v'} \right)^{-1} \right] \\ & + \sum_{\substack{abcd \\ efgh}} \gamma_{r,12ab}^{qv} \mathcal{U}_{r;bacd}^q \left( \mathbb{1}_{cdgh} - \mathcal{U}_{r;cdef}^q \chi_{r;efgh}^q \right) \gamma_{r;hg34}^{qv'} \end{aligned} \quad (3.139)$$

with the auxiliary susceptibility  $\chi_{r,1234}^{*,qv v'}$  of Eq. (3.60) and the three-leg vertex  $\gamma_{r,1234}^{qv}$  of Eq. (3.63). In the following section, we will present a short derivation of the particle-particle pairing vertex for the case of  $q = 0$  within the framework of ladder-D $\Gamma$ A.

### 3.11.1 Derivation of the pairing vertex $\Gamma_{pp}$ within ladder-D $\Gamma$ A

The vertex of Eq. (3.139) does not fulfill any crossing-symmetry relation, since it has been created from the BSE in the particle-hole channel only. It therefore solely possesses the particle-swapping symmetry [28]. To restore the crossing symmetry, we plug this vertex into Eq. (3.113) and obtain for the  $\uparrow\downarrow$ -component [27, 28]

$$F_{1234;\uparrow\downarrow}^{D\Gamma A; qkk'} = \frac{1}{2} \left( F_{d;1234}^{qv v'} - F_{m;1234}^{qv v'} \right) - F_{m;1432}^{(k-k')v(v-\omega)} - \frac{1}{2} \left( F_{d;1234}^{\omega v v'} - F_{m;1234}^{\omega v v'} \right). \quad (3.140)$$

The  $F_{m;1432}^{(k-k')v(v-\omega)}$ -term arises from the  $ph \rightarrow \overline{ph}$  transformation to restore crossing symmetry and hence introduces an orbital permutation as well as frequency shifts. This is an equation only written down for the  $\uparrow\downarrow$ -component of the full vertex. Luckily, one can obtain the  $\uparrow\downarrow$ -component via a crossing symmetry relation of the  $\uparrow\downarrow$ -component in the following way:

$$F_{1234;\uparrow\downarrow}^{qkk'} = -F_{1432;\uparrow\downarrow}^{(k-k')k(k-q)}. \quad (\pi)$$

One therefore recovers for the  $\uparrow\downarrow$ -component via Eq. ( $\pi$ )

$$\begin{aligned} F_{1234;\uparrow\downarrow}^{D\Gamma A; qkk'} = & -\frac{1}{2} \left( F_{d;1432}^{(k-k')v(v-\omega)} - F_{m;1432}^{(k-k')v(v-\omega)} \right) + F_{m;1234}^{qv v'} \\ & + \frac{1}{2} \left( F_{d;1432}^{(v-v')v(v-\omega)} - F_{m;1432}^{(v-v')v(v-\omega)} \right). \end{aligned} \quad (3.142)$$

This yields for the full vertices in  $ph$ -notation for both the singlet ( $\uparrow\downarrow - \overline{\uparrow\downarrow}$ )

$$\begin{aligned} F_{s;1234}^{D\Gamma A; qkk'} = & \frac{1}{2} \left( F_{d;1234}^{qv v'} - 3F_{m;1234}^{qv v'} \right) - \frac{1}{2} \left( F_{d;1234}^{\omega v v'} - F_{m;1234}^{\omega v v'} \right) \\ & + \frac{1}{2} \left( F_{d;1432}^{(k-k')v(v-\omega)} - 3F_{m;1432}^{(k-k')v(v-\omega)} \right) - \frac{1}{2} \left( F_{d;1432}^{(v-v')v(v-\omega)} - F_{m;1432}^{(v-v')v(v-\omega)} \right) \end{aligned} \quad (3.143)$$



and triplet ( $\uparrow\downarrow + \uparrow\downarrow$ ) spin combination

$$\begin{aligned} F_{t;1234}^{D\Gamma A; qkk'} &= \frac{1}{2} \left( F_{d;1234}^{qv\omega} + F_{m;1234}^{qv\omega} \right) - \frac{1}{2} \left( F_{d;1234}^{\omega v\omega} - F_{m;1234}^{\omega v\omega} \right) \\ &\quad - \frac{1}{2} \left( F_{d;1432}^{(k-k')v(\omega-\omega)} + F_{m;1432}^{(k-k')v(\omega-\omega)} \right) + \frac{1}{2} \left( F_{d;1432}^{(v-v')v(\omega-\omega)} - F_{m;1432}^{(v-v')v(\omega-\omega)} \right). \end{aligned} \quad (3.144)$$

We now want to evaluate this expression for  $q_{pp} = 0$  by setting  $q_{ph} = k_{pp} + k'_{pp}$ ,  $k_{ph} = k_{pp}$  and  $k'_{ph} = k'_{pp}$  [28]. Inserting these frequencies and momenta yields for the singlet channel

$$\begin{aligned} F_{s;1234}^{D\Gamma A; (q_{pp}=0)kk'} &= \frac{1}{2} \left( F_{d;1234}^{(k+k')v\omega} - 3F_{m;1234}^{(k+k')v\omega} \right) - \frac{1}{2} \left( F_{d;1234}^{(v+v')v\omega} - F_{m;1234}^{(v+v')v\omega} \right) \\ &\quad + \frac{1}{2} \left( F_{d;1432}^{(k-k')v(-\omega)} - 3F_{m;1432}^{(k-k')v(-\omega)} \right) - \frac{1}{2} \left( F_{d;1234}^{(v-v')v(-\omega)} - F_{m;1234}^{(v-v')v(-\omega)} \right) \\ &= \underbrace{\frac{1}{2} \left( F_{d;1234}^{(k+k')v\omega} - 3F_{m;1234}^{(k+k')v\omega} \right) - F_{1234; \uparrow\downarrow}^{(v+v')v\omega}}_{\tilde{F}_{s;1234}^{D\Gamma A; (q=0)kk'}} + \underbrace{\left( k' \rightarrow -k' \ \& \ 1234 \rightarrow 1432 \right)}_{\tilde{F}_{s;1432}^{D\Gamma A; (q=0)k(-k')}}. \end{aligned} \quad (3.145)$$

For the triplet channel we analogously find

$$\begin{aligned} F_{t;1234}^{D\Gamma A; (q_{pp}=0)kk'} &= \frac{1}{2} \left( F_{d;1234}^{(k+k')v\omega} + F_{m;1234}^{(k+k')v\omega} \right) - \frac{1}{2} \left( F_{d;1234}^{(v+v')v\omega} - F_{m;1234}^{(v+v')v\omega} \right) \\ &\quad - \frac{1}{2} \left( F_{d;1432}^{(k-k')v(-\omega)} + F_{m;1432}^{(k-k')v(-\omega)} \right) + \frac{1}{2} \left( F_{d;1234}^{(v-v')v(-\omega)} - F_{m;1234}^{(v-v')v(-\omega)} \right) \\ &= \underbrace{\frac{1}{2} \left( F_{d;1234}^{(k+k')v\omega} + F_{m;1234}^{(k+k')v\omega} \right) - F_{1234; \uparrow\downarrow}^{(v+v')v\omega}}_{\tilde{F}_{t;1234}^{D\Gamma A; (q=0)kk'}} - \underbrace{\left( k' \rightarrow -k' \ \& \ 1234 \rightarrow 1432 \right)}_{\tilde{F}_{t;1432}^{D\Gamma A; (q=0)k(-k')}}. \end{aligned} \quad (3.146)$$

We can construct the pairing vertex in either singlet or triplet channel by subtracting the purely *local* particle-particle reducible diagrams. We only need to consider the local diagrams here, since neglecting the momentum dependence of particle-particle reducible diagrams is a key approximation in ladder-D $\Gamma$ A. This yields

$$\Gamma_{s/t;1234}^{(q=0)kk'} = F_{s/t;1234}^{D\Gamma A; (q=0)kk'} - \Phi_{s/t;1234}^{(\omega=0)v\omega}. \quad (3.147)$$

The local reducible diagrams can be subtracted straightforwardly from  $\tilde{F}_{s/t;1234}^{D\Gamma A; (q_{pp}=0)k(\pm k')}$  in the following fashion

$$\begin{aligned} \Gamma_{s/t;1234}^{(q=0)kk'} &= \tilde{F}_{s/t;1234}^{D\Gamma A; (q=0)kk'} \pm \tilde{F}_{s/t;1432}^{D\Gamma A; (q=0)k(-k')} - \Phi_{s/t;1234}^{(\omega=0)v\omega} \\ &= \tilde{F}_{s/t;1234}^{D\Gamma A; (q=0)kk'} \pm \tilde{F}_{s/t;1432}^{D\Gamma A; (q=0)k(-k')} - \left( \Phi_{pp;1234; \uparrow\downarrow}^{(\omega=0)v\omega} \mp \Phi_{pp;1234; \uparrow\downarrow}^{(\omega=0)v\omega} \right) \\ &= \tilde{F}_{s/t;1234}^{D\Gamma A; (q=0)kk'} \pm \tilde{F}_{s/t;1432}^{D\Gamma A; (q=0)k(-k')} - \left( \Phi_{pp;1234; \uparrow\downarrow}^{(\omega=0)v\omega} \pm \Phi_{pp;1432; \uparrow\downarrow}^{(\omega=0)v(-\omega)} \right) \\ &= \underbrace{\tilde{F}_{s/t;1234}^{D\Gamma A; (q=0)kk'} - \Phi_{pp;1234; \uparrow\downarrow}^{(\omega=0)v\omega}}_{\tilde{\Gamma}_{s/t;1234}^{(q=0)kk'}} \pm \underbrace{\left( \tilde{F}_{s/t;1432}^{D\Gamma A; (q=0)k(-k')} - \Phi_{pp;1432; \uparrow\downarrow}^{(\omega=0)v(-\omega)} \right)}_{\tilde{\Gamma}_{s/t;1432}^{(q=0)k(-k')}} \\ &= \tilde{\Gamma}_{s/t;1234}^{(q=0)kk'} \pm \left( k' \rightarrow -k' \ \& \ 1234 \rightarrow 1432 \right). \end{aligned} \quad (3.148)$$

[28] The frequency notation for the particle-particle channel used in this thesis has been written down in Eq. (3.29c).



### 3.11.2 Symmetry of the gap function

We can show that the gap function inherits the correct symmetry upon using the symmetrized vertices of Eq. (3.148). Recall that the multi-orbital Eliashberg equation for the case  $q = 0$  is given by

$$\lambda_{s/t} \Delta_{s/t;12}^k = \pm \frac{1}{2} \sum_{k'; abc\bar{d}} \Gamma_{s/t;1b2a}^{(q=0)kk'} \chi_{s/t;0;acbd}^{(q=0)k'} \Delta_{s/t;\bar{d}c}^{k'} \quad (3.149)$$

for  $q = 0$  and the singlet and triplet gap functions fulfill  $\Delta_{s;12}^k = \Delta_{s;21}^{-k}$  and  $\Delta_{t;12}^k = -\Delta_{t;21}^{-k}$ , respectively. We can write  $\Gamma$  in the symmetrized form with the irreducible vertices  $\tilde{\Gamma}$  from Eq. (3.148) above, i.e.,

$$\Gamma_{s/t;1234}^{(q=0)kk'} = \tilde{\Gamma}_{s/t;1234}^{(q=0)kk'} \pm \tilde{\Gamma}_{s/t;1432}^{(q=0)k(-k')}, \quad (3.150)$$

where  $\tilde{\Gamma}_{s/t;1234}^{(q=0)kk'}$  contains both the non-local and local contribution to the irreducible vertex. To confirm that this combination enforces the correct symmetry of the gap function, we need to show that

$$\Delta_{s;12}^k - \Delta_{s;21}^{-k} = 0 \quad \text{and} \quad (3.151a)$$

$$\Delta_{t;12}^k + \Delta_{t;21}^{-k} = 0. \quad (3.151b)$$

This expression for  $q = 0$  then reads for both the singlet and triplet channels

$$\Delta_{s;12}^k - \Delta_{s;21}^{-k} \propto \sum_{k'; abc\bar{d}} \left[ \Gamma_{s;1b2a}^{(q=0)kk'} - \Gamma_{s;2b1a}^{(q=0)(-k)k'} \right] \chi_{s;0;acbd}^{(q=0)k'} \Delta_{s;\bar{d}c}^{k'} \quad \text{and} \quad (3.152a)$$

$$\Delta_{t;12}^k + \Delta_{t;21}^{-k} \propto \sum_{k'; abc\bar{d}} \left[ \Gamma_{t;1b2a}^{(q=0)kk'} + \Gamma_{t;2b1a}^{(q=0)(-k)k'} \right] \chi_{t;0;acbd}^{(q=0)k'} \Delta_{t;\bar{d}c}^{k'}. \quad (3.152b)$$

The full non-local ladder vertices of Eq. (3.145) and Eq. (3.146) fulfill the swapping symmetry, which is passed along to the pairing vertex  $\Gamma_{s/t;1234}^{(q=0)kk'}$  and reads in pp-notation for  $q = 0$

$$\Gamma_{s/t;1234}^{(q=0)kk'} = \Gamma_{s/t;3412}^{(q=0)(-k)(-k')} \stackrel{(3.150)}{=} \pm \Gamma_{s/t;3214}^{(q=0)(-k)k'}. \quad (3.153)$$

Applying Eq. (3.153) to Eq. (3.152a) then yields for the singlet channel

$$\Delta_{s;12}^k - \Delta_{s;21}^{-k} \propto \sum_{k'; abc\bar{d}} \left[ \Gamma_{s;1b2a}^{(q=0)kk'} - \Gamma_{s;1b2a}^{(q=0)kk'} \right] \chi_{s;0;acbd}^{(q=0)k'} \Delta_{s;\bar{d}c}^{k'} = 0 \quad (3.154)$$

and analogously for the triplet channel, see Eq. (3.152b),

$$\Delta_{t;12}^k + \Delta_{t;21}^{-k} \propto \sum_{k'; abc\bar{d}} \left[ \Gamma_{t;1b2a}^{(q=0)kk'} - \Gamma_{t;1b2a}^{(q=0)kk'} \right] \chi_{t;0;acbd}^{(q=0)k'} \Delta_{t;\bar{d}c}^{k'} = 0, \quad (3.155)$$

confirming that the symmetrization in Eq. (3.150) leads to the correct symmetry of the gap function.

### 3.11.3 Efficient solving of the Eliashberg equation via a Fourier transform

To avoid having to deal with two momentum indices for the pairing vertex  $\Gamma_{1234}^{(q=0)kk'}$  in the calculation, one can perform a Fourier transform to real space. However, this is only of advantage in the ladder approximation of the vertex, since then  $\Gamma_{1234}^{(q=0)kk'} = \Gamma_{1234}^{k-k',(\omega=0)\nu\nu'}$ . The sum over  $k'$  of Eq. (3.136) is essentially a convolution in momentum space, which reduces to a multiplication in Fourier space. We thus take the Fourier transform of Eq. (3.136) in the case of  $q = 0$  with respect to  $\mathbf{k}$

$$\lambda_{s/t} \sum_{\mathbf{k}} e^{i\mathbf{k}\mathbf{x}} \Delta_{s/t;12}^{\mathbf{k}} = \pm \frac{1}{2} \sum_{\mathbf{k}\mathbf{k}';\mathbf{a}\mathbf{b}\mathbf{c}\mathbf{d}} e^{i\mathbf{k}\mathbf{x}} \Gamma_{s/t;1\mathbf{b}2\mathbf{a}}^{k-k',(\omega=0)\nu\nu'} \chi_{s/t;0;\mathbf{a}\mathbf{c}\mathbf{b}\mathbf{d}}^{\mathbf{k}'} \Delta_{s/t;\mathbf{d}\mathbf{c}}^{\mathbf{k}'} \quad (3.156)$$

where  $\mathbf{x} = (x_1, \dots, x_D)$  is a real-space vector for systems in  $D$  dimensions. If we introduce

$$\tilde{\Delta}_{s/t;\mathbf{b}\mathbf{a}}^{\mathbf{k}'} = \sum_{\mathbf{c}\mathbf{d}} \chi_{s/t;0;\mathbf{a}\mathbf{c}\mathbf{b}\mathbf{d}}^{\mathbf{k}'} \Delta_{s/t;\mathbf{d}\mathbf{c}}^{\mathbf{k}'} \quad (3.157)$$

and use the shift  $\mathbf{k} = \mathbf{q} + \mathbf{k}'$ , we can rewrite Eq. (3.156) as

$$\lambda_{s/t} \sum_{\mathbf{k}} e^{i\mathbf{k}\mathbf{x}} \Delta_{s/t;12}^{\mathbf{k}} = \pm \frac{1}{2} \sum_{\nu'\mathbf{a}\mathbf{b}} \sum_{\mathbf{q}} e^{i\mathbf{q}\mathbf{x}} \Gamma_{s/t;1\mathbf{b}2\mathbf{a}}^{q,(\omega=0)\nu\nu'} \sum_{\mathbf{k}'} e^{i\mathbf{k}'\mathbf{x}} \tilde{\Delta}_{s/t;\mathbf{b}\mathbf{a}}^{\mathbf{k}'} \quad (3.158)$$

This reads in Fourier-transformed quantities as

$$\lambda_{s/t} \Delta^{\mathbf{x}\nu} = \pm \frac{1}{2} \sum_{\nu'\mathbf{a}\mathbf{b}} \Gamma_{s/t;1\mathbf{b}2\mathbf{a}}^{\mathbf{x},(\omega=0)\nu\nu'} \tilde{\Delta}_{s/t;\mathbf{b}\mathbf{a}}^{\mathbf{x}\nu} \quad (3.159)$$

In essence, we have reduced the convolution of Eq. (3.136) in momentum space to a product of the quantities in real space, effectively reducing the object from two momentum dimensions  $N_{\mathbf{k}} \times N_{\mathbf{k}}$  to a single real-space dimension  $N_{\mathbf{x}} (= N_{\mathbf{k}})$ , reducing the object size by a factor  $N_{\mathbf{k}}$ . Numerically, solving the equation now can be done by performing a discrete Fourier transform on the quantities before executing the power iteration to calculate the gap function on the real-space axis. To afterwards obtain the momentum-dependent gap function, one simply applies the inverse transformation to the result.



## CHAPTER

## 4

## THE CODE

The main part of this thesis is the implementation of a self-consistent ladder- $D\Gamma A$  calculation with an emphasis on usability and minimal setup effort. The code is designed to be both accessible and performant, targeting fast execution through efficient parallelization and extensive memory optimizations. It is written in Python and relies mainly on NumPy for numerical computations, making use of vectorized operations and optimized linear algebra routines. In addition, the code carefully exploits symmetries inherent to the physical problem to further reduce computational cost and memory usage. In this chapter, we present the implementation of the computational framework developed to achieve a fully converged self-energy through the self-consistency algorithm of the ladder- $D\Gamma A$  equations and a subsequent calculation of the superconducting eigenvalues and gap functions for both singlet and triplet electron pairing.

The code is designed to efficiently compute vertex functions, such as the one-particle Green's function, irreducible and full vertices, three-leg vertices, the electron self-energy and many more, while maintaining flexibility for extensions and modifications. Building upon the underlying theoretical foundations which were established already in the previous chapters, this numerical implementation aims to translate the formal expressions into a working algorithm. Special attention has been given to structuring the code in a modular and efficient manner, ensuring that it can be used not only for the ladder- $D\Gamma A$  equations, but also for other algorithms that require multi-point vertex functions within the Matsubara frequency framework in condensed matter physics.

The package will be provided under the MIT license, making it freely available for use, modification, and distribution. This permissive license promotes collaboration and allows academics and developers to make changes on the code without placing restrictions. By publishing the implementation open-source, we hope to encourage accessibility, reproducibility, and community development.

In this chapter, we start with an overview of the overall structure and design choices of the code, followed by a detailed discussion of its core components and algorithms. We then describe the typical workflow for using the code, including input handling, computational steps and output generation. Finally, we discuss validation methods and potential improvements for future work.

## 4.1 Structure and design choices

Please note that there already exist two programs that allow the calculation of vertex functions and the self-energy through ladder- $D\Gamma A$ : (i) Abinitio $D\Gamma A$  [28, 42, 83], which is a one-shot multi-

orbital calculation of the D $\Gamma$ A self-energy and (ii) DGAPy [84], which is the one-band version of it, where additional quantities are calculated, such as the superconducting eigenvalues and real-valued Green's functions. The former is written in Fortran, whereas the latter has been developed in Python. The purpose of the code developed in the course of this thesis is to provide the functionality of AbinitioD $\Gamma$ A, while being easily accessible and quick to set-up, similar to DGAPy. Therefore, we decided to write the program in Python. A main advantage of this programming language is its low entry-barrier and the easy set-up and code-execution. In theory, all that is needed is a Python environment with the necessary packages<sup>[1]</sup>, DMFT input files and the configuration file.

As already mentioned, there already exists a Python package, called DGAPy [84], written by Paul Worm, which is capable of performing a single-band  $\lambda$ -corrected one-shot ladder-D $\Gamma$ A calculation. The code in this thesis will, however, be concerned with the multi-orbital implementation of the algorithm, additionally employing a self-consistency loop contrary to the  $\lambda$ -correction and will be capable of handling non-local Coulomb interactions. So far, DGAPy has successfully been used in several instances, for example in Refs. [85, 86], to only mention a few. Since it is already widely used among researchers, the transition from DGAPy to this code should be as simple as possible, hence the configuration file and some internal modules are designed very similar.

#### 4.1.1 Parallelization via MPI

To lower the computation time, we employ the use of the mpi4py library in Python, which enables distributed computing across multiple processes in a straightforward and Pythonic manner. This allows the program to run inside a process pool, where objects can easily be sliced and passed to or gathered from other processes. While an ideal speed-up factor of  $n$  for  $n$  processes is theoretically possible, in practice, communication overhead and memory transfer costs typically limit the effective gain. Nevertheless, for large-scale computations involving high-dimensional vertex functions or large frequency boxes, this parallelization leads to significant reductions in runtime.

The central class handling parallelization is the `MpiDistributor`, which is initialized at the point where the explicitly non-local parts of the ladder-D $\Gamma$ A algorithm begin. This class abstracts the communication logic and provides a consistent interface for scattering and gathering objects across processes. The current implementation slices the data along the transferred momentum  $\mathbf{q}$ , which is possible due to the block-diagonal structure of most equations up to the Schwinger-Dyson equation (3.64). Each MPI process is responsible for a specific set of  $\mathbf{q}$ -points, allowing for highly parallel and independent evaluation of vertex contractions.

Internally, the slicing is guided by knowledge of the irreducible Brillouin zone, and the distributor automatically determines the mapping from global  $\mathbf{q}$ -grid indices to process-local ones. This separation of concerns between parallelization logic and physics routines enhances maintainability and flexibility of the code. Further MPI optimizations, such as asynchronous communications or load balancing across uneven grid sizes, could be explored in future versions.

#### 4.1.2 Memory reduction through symmetry

The memory demands of a full ladder-D $\Gamma$ A calculation can be substantial, especially for multi-orbital models and large frequency ranges. To mitigate this, the code incorporates several symmetry-based

---

<sup>[1]</sup>For a detailed list of requirements including package versions, see the file `requirements.txt` in the source code directory.

optimizations that significantly reduce the memory footprint and enable efficient scaling to larger systems.

First, the calculation of non-local quantities is performed exclusively within the irreducible Brillouin zone. Thanks to the crystal symmetries of common lattice structures (e.g., square or quasi-1D lattices), only a small subset of the full momentum grid needs to be explicitly computed. The code determines this set via symmetry operations specified in the `brillouin_zone` module, which ensures compatibility with arbitrary lattice symmetries defined in the configuration. For instance, on a  $16 \times 16 \times 1$  grid, only 45 out of 256  $\mathbf{q}$ -points are needed for a square lattice, which directly reduces both computational and memory load by more than a factor of five and even higher for larger grid sizes.

To further save memory, we keep most of the objects in half of their bosonic Matsubara frequency range: Due to the symmetry  $F_{1234}^{\omega\nu\nu'} = (F_{4321}^{(-\omega)(-\nu)(-\nu')})^* = (F_{4321}^{(-\omega)\nu\nu'})^*$ <sup>[2]</sup>, we can restrict the objects to their positive bosonic Matsubara frequency region only. This saves half of the memory and thus a very large amount for the biggest objects, such as the auxiliary susceptibility or the full vertex.

These symmetry-based reductions are implemented in a transparent way for the user: the internal representation is compressed, but the high-level API provides access to the full data. This allows for both memory efficiency and usability, enabling the user to work with large systems that would otherwise be intractable on a single machine.

### 4.1.3 Object-oriented API

We tried to keep a very object-oriented approach when developing the toolbox for the program, as opposed to both `DGApy` and `AbinitioDGA`. Hence instead of directly working with NumPy arrays, we work with `(Local)FourPoint`, `(Local)Interaction`, `SelfEnergy`, `GreensFunction` and `GapFunction` classes. The reason being that in Python, it is very easy to overload operators, i.e. with so-called “dunder” methods, hence we implemented the most common operators “+/-/@/~”<sup>[3]</sup>, alongside multiplication and division with numbers, for these objects to help make the implementation of equations easier. This might not be an obvious improvement at first, however the underlying structure allows a very simple high-level handling of these objects, where most of the logic is performed in the background and only has to be coded once. We will discuss the explicit implementation of these dunder methods later.

Compared to `DGApy`, we stripped down the module responsible for the Matsubara frequency handling, since most of the features now can be called directly from the objects themselves. Instead of calling a method from the `matsubara_frequencies` module to cut an objects’ frequency range, it is now a method on the object itself, e.g., `object.cut_niv(10)`. Most of these methods are only implemented once in a base class which all subtypes inherit from. These base classes already cover most of the objects’ functionality, where the subclass only implements features unique to this object type.

All modules should be very self-explanatory, their names already provide a good description of what the module does and what its responsibilities are. For any details, we refer the reader to the documentation of the code inside the repository.

<sup>[2]</sup>The transformation from  $-\nu, -\nu'$  to  $\nu, \nu'$  is possible due to the symmetrized nature of the two-particle Green’s function and the inherited vertex functions.

<sup>[3]</sup>Corresponding to addition, subtraction, multiplication and inversion.

One benefit of the object-oriented approach is the now easy implementation of various equations. For example, writing an arbitrary equation with arbitrary (non-local) vertex functions  $A$ ,  $B$ ,  $C$  and  $D$  like

$$D_{1234}^{qv'v'} = \frac{1}{2\beta} \sum_{v_1;ab} A_{12ab}^{qv'v_1} (B_{ba34}^{\omega v_1} + C_{ba34}^{\omega v_1 v'}) \quad (4.1)$$

can be done with a call of  $D = 1 / (2 * \text{beta}) * A.\text{matmul}(B.\text{add}(C))$  or the dunder methods for matrix multiplication “@” and addition “+”, i.e.,  $D = 1 / (2 * \text{beta}) * A @ (B + C)$ , where the index contraction, frequency handling and summation will be done in the background. This eases readability in the code and reduces redundancy. Furthermore, it allows for very straightforward optimization of contractions and multiplications through this architecture. Furthermore, inverting a vertex function is also very easy now, all that needs to be called is the `obj.invert()` function (or with a “~” prefix, i.e. `~obj`) on any object and the code performs the inversion in the background using NumPy’s vectorization and SciPy’s memory-optimized inversion by converting the object to compound indices. Furthermore, other operations, such as addition/subtraction in the form of `A.add(B)/A.sub(B)` or just simply  $A \pm B$  are possible and automatically handle different amounts of frequency dimensions etc. for you. There are a bunch of other convenience methods available, where we would like to refer the interested reader to the code and its documentation for more details.

#### 4.1.4 Setup and execution

The code is very easy to set-up as it is available as an installable Python package, called `scdga`. After installing the necessary packages denoted in the `requirements.txt` file to the Python environment, one simply has to run “`pip install -e .`” from the repository directory in the terminal to install the package in editable mode. This allows the user to now access any module and class inside the `scdga` package. The main entry point to the program is the file `dga_main.py` file, which can be started with either “`python dga_main.py`” for single-core execution (mostly used for testing purposes) or “`mpiexec -np <n_proc> python dga_main.py`” for multi-core processing. There are two additional command line parameters available to append to the execution:

- “-p”: With “-p <path>” you can specify the path to the configuration file, which contains all run-specific parameters. This is useful if one wants to store multiple configuration files in different directories. If this parameter is not set, the path defaults to the location of the repository directory.
- “-c”: With “-c <config name>” you can specify the name of the configuration file you want to load. This defaults to `dga_config.yaml`.

As an example, the following shell command runs the code using 8 MPI processes and loads the configuration file `my_config.yaml` from the path `/configs/`:

“`mpiexec -np 8 python dga_main.py -p /configs/ -c my_config.yaml`”.

Additionally, we feature extensive logging: every important step in the calculation will be logged. If it is started from a terminal, the logging will be done to the standard output. If the code is executed on a slurm-based cluster, you will find the logs in the job output file. The reason we employ a lot of logging is the ease of finding errors that might occur during a calculation.

### 4.1.5 Configuration

The configuration file is split into small blocks of configuration sections, which will be explained in detail in the following. For those entries where only a single data type is expected, the code will try to parse the input to this specific type. If the parsing was unsuccessful, a warning is logged and a default value for this variable is used.

The first block of the configuration is concerned with the number of Matsubara frequencies one wants to use for the calculation:

```
box_sizes:
  niw_core: 50 # int, default: -1
  niv_core: 30 # int, default: -1
  niv_shell: 20 # int, default: 0
```

The “core” region defines the frequency box used for explicitly solving the Bethe-Salpeter and Schwinger-Dyson equations, while the “shell” region sets the size of the asymptotic tails needed for vertex reconstruction through the method described in Sec. 3.7.2. It is possible to set the core frequencies to “-1”, which means that the number of Matsubara frequencies from the DMFT calculation will be taken.

The next section is concerned with the Hamiltonian of the system, which currently is a little bit complex, since we wanted to adapt the existing configuration file from DGAPy and added new features. It defines the lattice symmetries, the momentum grid sizes and the kinetic and interaction part of the Hamiltonian:

```
lattice:
  symmetries: "two_dimensional_square"
                                     # string, default: "two_dimensional_square"
  type: "from_wannier90"             # string, default: "from_wannier90"
  hr_input: "/path/to/file"          # string | list[float], default: None
  interaction_type: "local_from_dmft"
                                     # string, default: "local_from_dmft"
  interaction_input: "/path/to/file"
                                     # string | list[float], default: None
  nk: [16, 16, 1]                   # list[int], default: [16, 16, 1]
  nq: [16, 16, 1]                   # list[int], default: [16, 16, 1]
```

Here, we have a bunch of settings available that can be combined in different ways. First, we can define the lattice symmetry, where one has to enter a set of predefined symmetry sets. It is possible to extend the symmetries the code supports by adding the corresponding symmetry operations and symmetry sets in the code. The available symmetry sets are `two_dimensional_square`, `quasi_one_dimensional_square`, `simultaneous_x_y_inversion` and `quasi_two_dimensional_square_symmetries`. Next is the type of input to the kinetic part of the Hamiltonian we require. It can either be `from_wannier90`, `from_wannierHK` or `t_tp_tpp` (only for single-band input). The first input type is used if the subsequent field `hr_input` references to a file, where the hopping elements are written in real space, whereas `from_wannierHK` is used if the Hamiltonian in Fourier space is available as a file<sup>[4]</sup>. The last option is only used for single-band input, where the band distribution is that of a  $t$ ,  $t'$  and  $t''$  hopping model only. If this type is specified, then a list of three float values in `hr_input` is expected.

Since this code is capable of performing multi-orbital calculations with non-local interactions,

<sup>[4]</sup>Note that for the former, it is possible to use arbitrary  $\mathbf{k}$ -grid sizes, since the Fourier transform will be performed in the code, whereas for the latter one the correct grid size has to be entered.



we require the definition of a interaction type and an input. The available interaction types are `local_from_dmft`, `kanamori_from_dmft`, `kanamori` and `custom`. If `local_from_dmft` is specified, we expect a single-band input, where the interaction strength is taken from DMFT. Similar to that, the `kanamori_from_dmft` option takes the interaction values from DMFT and constructs the correct interaction matrix with the Kanamori-specific entries. In both cases, the field `interaction_input` will not be read. If `kanamori` is specified, then we expect a list of four values in `interaction_input`, which contains the number of orbitals as the first entry and then  $U$ ,  $J$  and  $V$  as the next three entries. One can enter whole numbers for the number of bands and floating point values for the interaction strengths. Lastly, if one specifies `custom` as the interaction type, we then expect a path to a file, which is structured similarly to a real-space Hamiltonian file but with four orbital entries instead of just two. It is possible to include non-local interactions there. Furthermore, it is possible to set the sizes of both the  $\mathbf{k}$ - and  $\mathbf{q}$ -grid in the fields `nk` and `nq`, respectively. It is possible to not set `nq`, where `nk` will be used for the  $\mathbf{q}$ -grid. Note, that the execution of the Eliashberg equation is only possible if both the  $\mathbf{k}$ - and the  $\mathbf{q}$ -grid are of the same size.

The next configuration section is concerned with the self-consistency calculation and defines the convergence behavior and mixing strategy of the self-consistency loop:

```
self_consistency:
    max_iter: 20                # int , default: 20
    save_iter: True            # bool , default: True
    epsilon: 1e-6              # float , default: 1e-4
    mixing: 0.3                # float , default: 0.2
    mixing_strategy: "pulay"    # string , default: "linear"
    mixing_history_length: 2    # int , default: 3
    previous_sc_path: "path/to/files" # string , default: "./"
```

The field `max_iter` is to set an upper boundary on the number of iterations during the self-consistency cycle. If the self-energy does not converge within `max_iter` iterations, the iteration will stop. When setting `save_iter` to `True`, the code will save the non-local D $\Gamma$ A self-energy for each iteration. The next parameter, `epsilon`, is set to determine the absolute value difference allowed for the last two calculated sigmas to be considered converged. The convergence will be tested on a predefined set of  $\mathbf{k}$ -points and frequencies  $\nu$ . Next, we can specify the mixing parameter that will be used in the mixing scheme and is a floating point number between  $(0, 1]$ . We can furthermore specify the mixing scheme in the next parameter, called `mixing_strategy`. Here, we can choose from either `linear` or `pulay` mixing, where if `pulay` is specified, it takes `mixing_history_length` number of previous self-energy results to construct a prediction. If the number of iterations is less than the history length, we will use linear mixing for these iterations and switch to Pulay mixing afterwards. The last parameter, `previous_sc_path` allows us to specify the path to a previous self-consistency iteration folder, which might not have been converged or which needs to be converged further or with different parameters. The program then takes the last iterations of the already performed calculation and uses these as a starting point for the next calculation. If the number of iterations from the previous calculation is equal or larger than `mixing_history_length` and `pulay` is specified, then Pulay mixing will be applied, otherwise we mix linearly.

Given the improved speed and scalability of this code compared to DGApy, we have also implemented two  $\lambda$ -correction schemes which only work for single-band cases and can be configured with the following short section:

```
lambda_correction:
    perform_lambda_correction: True # bool, default: False
    type: "spch" # string, default: "spch"
```

Here, setting `perform_lambda_correction` to `True` will perform a  $\lambda$ -correction if the input is a single-band model. Otherwise, an error is raised and the code exits. Notice that if one wants a one-shot  $\lambda$ -corrected self-energy and calculation of the Eliashberg equation, then `max_iter` and mixing in the `self_consistency` section need to be set to “1”. The other parameter is the type of  $\lambda$ -correction which will be performed. Setting this to `spch` will renormalize both the density and magnetic susceptibilities, whereas setting it to `sp` will only renormalize the magnetic susceptibility.

The next section is a very important one, since it is concerned with the location of the DMFT files and mainly defines their location and file names:

```
dmft_input:
    type: "w2dyn" # string, default: "w2dyn"
    input_path: "/path/to/files" # string, default: "./"
    fname_1p: "filename" # string, default: "1p-data.hdf5"
    fname_2p: "filename" # string, default: "g4iw_sym.hdf5"
    do_sym_v_vp: True # bool, default: True
```

Currently, the `type` argument only supports `w2dyn` as input type, but this could be extended in the future to also support input files from other sources with other file structures. Next, `input_path` needs to be set to the folder that contains the output data from `w2dynamics`. We require two files, one containing one-particle quantities (such as the DMFT Green’s function and self-energy) and one containing two-particle quantities (such as the two-particle Green’s function); their filenames can be set in `fname_1p` and `fname_2p`, respectively. Notice that `w2dynamics` outputs a large `Vertex.hdf5`-file, where we have to extract the relevant worm components beforehand. This can be done with the script `symmetrize.py`, which is also part of the repository. This will automatically extract all relevant worm components of the two-particle Green’s function and writes it to a separate file containing the density and magnetic contributions. Lastly, we have the option to symmetrize the two-particle Green’s function in  $v$  and  $v'$  before processing them further. This might be necessary sometimes to ensure numerical symmetry of the vertex functions.

The second to last configuration section we will cover here is the output section which, as the name already suggests, covers the program’s output settings, such as the output path and plotting instructions:

```
output:
    output_path: "/path" # string, default: "./"
    do_plotting: True # bool, default: "True"
    plotting_subfolder_name: "Plots" # string, default: "Plots"
    save_quantities: True # bool, default: True
```

We are able to choose the path where the output of the program is saved to. If this field is chosen empty, the output will be put into a sub-folder inside the DMFT input folder. If we specify `do_plotting`, then we plot a selective set of quantities and save them to the sub-folder specified in `plotting_subfolder_name`. We then have the possibility to additionally save almost all quantities that are calculated during the main program as `numpy` files, except for the pairing vertex and the full ladder- $D\Gamma A$  vertex. These are separately handled in the Eliashberg section, since they are only calculated if you want to perform the calculation of the superconducting eigenvalue and gap function.

Finally, the last configuration section is concerned with the Eliashberg equation and is configuring the eigenvalue and gap function-finding through a Lanczos method:

```
eliashberg:
  perform__eliashberg: True      # bool, default: False
  save__pairing__vertex: False  # bool, default: False
  save__fq: False               # bool, default: False
  n__eig: 2                     # int, default: 2
  epsilon: 1e-9                 # float, default: 1e-6
  symmetry: "random"            # string, default: "random"
  include__local__part: True    # bool, default: True
  subfolder__name: "Eliashberg" # string, default: "Eliashberg"
```

Here, the first setting is to let the program know if you want to perform the Eliashberg equation to obtain the superconducting singlet and triplet eigenvalues and gap functions, respectively. If this setting is set to “False”, then the program will exit after the self-energy has been calculated. The next two settings allow to save the pairing vertex  $\Gamma^{(q=0)kk'}$  and the full ladder vertex  $F^{qv'}$  to a file. These are set to “False” per default, as these objects can be quite large, especially the full vertex, which can reach up to hundreds of gigabytes. Both will be saved for the irreducible Brillouin zone only to save memory. The following three settings, `n__eig`, `epsilon` and `symmetry` are concerned with the power iteration that is performed to solve the Eliashberg equation. Here, it is possible to specify the number of eigenvalues and eigenvectors one wants to calculate in `n__eig`. Notice, that we will always calculate `n__eig+1` eigenvalues. This is due to the fact that first we calculate the single largest eigenvalue with a Lanczos method and then calculate the `n__eig` eigenvalues that are closest to one using shift-invert mode. Most of the time, however, the eigenvalues of both calculations are equal. `epsilon` is the setting that determines the target precision of the power iteration which is performed and `symmetry` determines the starting vector. There are a couple of options available for `symmetry` that may help speeding up the power iteration convergence if one knows the pairing symmetry of the gap function a priori: `random`, `p-wave-x`, `p-wave-y` and `d-wave`. In almost all cases it should suffice to pick a random starting vector for the power iteration.

In principle one also needs the *purely local* full and reducible vertices for the pairing vertex, however these can be omitted if one expects d-wave symmetry of the gap function, where the local vertex functions do not contribute to the eigenvalue and gap function due to symmetry. Setting `include__local__part` to “False” does exactly that. Not calculating the local part allows for a slightly larger frequency box and a better estimation of the eigenvalue and gap function for d-wave symmetry cases.

The last setting is the sub-folder name where the Eliashberg output will be saved to.

#### 4.1.6 Input files

After the vertex calculation has been performed with `w2dynamics` [52], we have to extract a couple of key quantities, such as the local self-energy, Green’s function, interaction and two-particle Green’s functions from the output files of `w2dyn`. There is a script located in the repository, called `symmetrize.py`, which allows for the straightforward extraction of the two-particle Green’s function from the vertex file of `w2dyn`. A simple execution of this script yields a new file, where the density and magnetic components of  $G_{r,1234}^{\omega v v'}$  are written to. This is handy, since the vertex file from `w2dyn` is usually very large and it can be deleted after the symmetrization process. Then one is left with the `1p-data.hdf5` and `g4iw_sym.hdf5` files, which contain the one-particle and two-particle (symmetrized) quantities. These are, next to a file containing the real-space (e.g., `wannier_hr.dat`) or Fourier-space

(e.g., `wannier.hk`) Hamiltonian, the only input files needed for the execution of the D $\Gamma$ A algorithm. Notice that no file name is fixed and they can be specified in the corresponding `dga_config.yaml` file.

## 4.2 Result validation

In order to check if the program's output is correct, we created a few simple test cases to validate our results:

- A single-band test, where the code should reproduce the results of DGApy
- A two-band test with the same parameter as the case above, where each band is indistinguishable and electrons in one band do not interact with electrons in the other band. The outputs should be equal to the single-band case in two orbital components and zero elsewhere.
- A rotation of the previous test-case. When rotating the DMFT input data, i.e. the local one- and two-particle Green's function and the self-energy, and the Hamiltonian in orbital space, we expect the output to produce the same results as the second test case after a orbital rotation in the opposite direction.



## CHAPTER

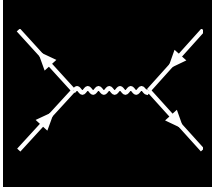
**5**

---

---

**CONCLUSIONS AND  
OUTLOOK**



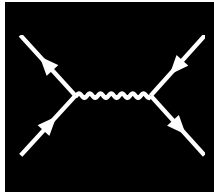


## LIST OF FIGURES

2.1	Visual representation of a subset of interaction and hopping terms of Eq. (2.14). We show two lattice sites $i$ and $j$ with orbitals $m, n$ and $m', n'$ , respectively. . . . .	8
2.2	Kanamori parameters $U, U'$ and $J$ as described in the text: (A) intra-orbital Coulomb interaction, (B)-(C) inter-orbital Coulomb interaction, (D) spin-flip of an electron pair and (E) pair hopping. . . . .	10
2.3	Visual representation of the two-dimensional square lattice Hubbard model. Each lattice site either contains zero, one or two electrons. Every circle represents a local orbital at any site. Here, $t, t'$ and $t''$ denote nearest-neighbor hopping, next-nearest-neighbor hopping and next-next-nearest-neighbor hopping, respectively. Reasonable values for $t, t', t''$ and $U$ are obtained from density functional theory (DFT) calculations [10] or extracted from ARPES studies [11]. For e.g., cuprates, one finds that $t \approx 0.3-0.5$ eV, $t' \approx -0.2t$ , $t'' \approx 0.1t$ and $U \approx 8t$ . . . . .	12
3.1	Diagrammatic representation of the one-particle Green's function $G_{12}$ . The electron is annihilated at 1, propagates in imaginary time from $\tau_1$ to $\tau_2$ and is created at 2. . . . .	14
3.2	First order diagrams for the single-particle Green's function. The corresponding diagrams are coined the Hartree- and the Fock-term, respectively. As the name suggests, taking only these two diagrams as the whole perturbation expansion leads to the Hartree-Fock approximation, formulated as a diagrammatic theory. . . . .	17
3.3	Diagrammatic representation of Eq. (3.18). The full Green's function $G_{12}^k$ is drawn as a thick black line. . . . .	18
3.4	In the case of absent spin-orbit coupling, these are the only non-vanishing spin combinations of the two-particle Green's function. . . . .	19
3.5	Diagrammatic representation of the crossing symmetry relations in order of Eq. (3.27a) - Eq. (3.27c). . . . .	20
3.6	Two-particle Green's functions in the different frequency notations of Eq. (3.29a) - Eq. (3.29c) expressed in Feynman diagrams. The frequency notation is encoded in an additional subscript, $\{\text{ph}, \overline{\text{ph}}, \text{pp}\}$ . . . . .	21
3.7	Diagrammatic representation of the two-particle connected Green's function up to order two. It includes the possible interaction processes that occur between two propagating electrons. The particle labels are only written down for the first diagram, the other diagrams are labeled analogously. . . . .	22
3.8	Disconnected part (second and third term on the right hand side of Eq. (3.31)) of the two-particle Green's function. . . . .	22
3.9	The physical susceptibility is defined as the generalized susceptibility with contracted legs, see Eq. (3.45). . . . .	25



3.10	Diagrammatic version of the BSE in all three channels for arbitrary spin components, see Eq. (3.49). The lower legs are exchanged in pp-notation, hence their direction is reversed. . . . .	27
3.11	Representation of the Schwinger-Dyson equation (3.56). . . . .	28
3.12	Interaction-reducible form of the Schwinger-Dyson equation (3.61) with susceptibilities. . . . .	29
3.13	Interaction-reducible form of the Schwinger-Dyson equation (3.64) with three-leg vertices. . . . .	30
3.14	Numerical SIAM results for all local vertices contained in the parquet equation Eq. (3.33) for vanishing transfer frequency $\Omega = 0$ , taken from Ref. [35]. In our convention, $\Omega$ should be replaced by $\omega$ . . . . .	31
3.15	Crossing-symmetric interaction, see Eq. (3.66). . . . .	32
3.16	Diagrammatic version of the kernel-1 and kernel-2 functions of Eq. (3.70) and Eq. (3.72). . . . .	33
3.17	This flowchart shows the D $\Gamma$ A self-consistency cycle. The first box is concerned with the bandstructure and interaction calculations using DFT and/or cRPA. The next box denotes the DMFT calculation which is performed using the previously calculated quantities. From the converged DMFT calculation we extract the DMFT self-energy and local two-particle vertex functions, such as the two-particle Green's function in the ph and pp-channel. The three boxes below describe the self-consistency cycle of the D $\Gamma$ A approach. The output quantities from DFT/cRPA and DMFT, i.e. all purely local vertex functions and the interaction, are kept constant throughout the D $\Gamma$ A self-consistency cycle. . . . .	46
3.18	Linearized Eliashberg equation for vanishing transfer frequency $q = 0$ , see Eq. (3.136). . . . .	49




---

## BIBLIOGRAPHY

- [1] P. Hohenberg and W. Kohn, “Inhomogeneous Electron Gas”, [Physical Review \*\*136\*\*, B864–B871 \(1964\)](#).
- [2] J. P. Perdew and K. Schmidt, “Jacob’s Ladder of Density Functional Approximations for the Exchange-Correlation Energy”, [AIP Conference Proceedings \*\*577\*\*, 1–20 \(2001\)](#).
- [3] P. Blaha, K. Schwarz, F. Tran, R. Laskowski, G. K. H. Madsen, and L. D. Marks, “WIEN2k: An APW+lo Program for Calculating the Properties of Solids”, [The Journal of Chemical Physics \*\*152\*\*, 074101 \(2020\)](#).
- [4] G. Kresse and J. Hafner, “Ab Initio Molecular Dynamics for Open-Shell Transition Metals”, [Physical Review B \*\*48\*\*, 13115–13118 \(1993\)](#).
- [5] J. Kuneš, R. Arita, P. Wissgott, A. Toschi, H. Ikeda, and K. Held, “Wien2wannier: From Linearized Augmented Plane Waves to Maximally Localized Wannier Functions”, [Computer Physics Communications \*\*181\*\*, 1888–1895 \(2010\)](#).
- [6] A. A. Mostofi, J. R. Yates, Y.-S. Lee, I. Souza, D. Vanderbilt, and N. Marzari, “Wannier90: A Tool for Obtaining Maximally-Localised Wannier Functions”, [Computer Physics Communications \*\*178\*\*, 685–699 \(2008\)](#).
- [7] L. Zhang and H.-P. Cheng, cRPA Calculation of On-Site and Nearest Neighbor Coulomb Interaction of version 1, June 16, 2022, pre-published.
- [8] A. Georges, L. de’Medici, and J. Mravlje, “Strong Correlations from Hund’s Coupling”, [Annual Review of Condensed Matter Physics \*\*4\*\*, 137–178 \(2013\)](#).
- [9] J. Kanamori, “Electron Correlation and Ferromagnetism of Transition Metals”, [Progress of Theoretical Physics \*\*30\*\*, 275–289 \(1963\)](#).
- [10] E. Pavarini, I. Dasgupta, T. Saha-Dasgupta, O. Jepsen, and O. K. Andersen, “Band-Structure Trend in Hole-Doped Cuprates and Correlation with  $T_{\text{cmax}}$ ”, [Physical Review Letters \*\*87\*\*, 047003 \(2001\)](#).
- [11] M. Hashimoto, T. Yoshida, H. Yagi, M. Takizawa, A. Fujimori, M. Kubota, K. Ono, K. Tanaka, D. H. Lu, Z.-X. Shen, S. Ono, and Y. Ando, “Doping Evolution of the Electronic Structure in the Single-Layer Cuprate  $\text{Bi}_2\text{Sr}_{2-x}\text{La}_x\text{CuO}_{6+\delta}$ : Comparison with Other Single-Layer Cuprates”, [Physical Review B \*\*77\*\*, 094516 \(2008\)](#).
- [12] T. Matsubara, “A New Approach to Quantum-Statistical Mechanics”, [Progress of Theoretical Physics \*\*14\*\*, 351–378 \(1955\)](#).
- [13] G. C. Wick, “Properties of Bethe-Salpeter Wave Functions”, [Physical Review \*\*96\*\*, 1124–1134 \(1954\)](#).

- [14] N. E. Bickers, D. J. Scalapino, and S. R. White, “Conserving Approximations for Strongly Correlated Electron Systems: Bethe-Salpeter Equation and Dynamics for the Two-Dimensional Hubbard Model”, [Physical Review Letters](#) **62**, 961–964 (1989).
- [15] E. H. Hwang and S. Das Sarma, “Quasiparticle Spectral Function in Doped Graphene: Electron-electron Interaction Effects in ARPES”, [Physical Review B](#) **77**, 081412 (2008).
- [16] J. Jang, H. M. Yoo, L. N. Pfeiffer, K. W. West, K. W. Baldwin, and R. C. Ashoori, “Full Momentum- and Energy-Resolved Spectral Function of a 2D Electronic System”, [Science](#) **358**, 901–906 (2017).
- [17] A. A. Abrikosov, L. P. Gor’kov, and I. Dzyaloshinskii, [Quantum Field Theoretical Methods in Statistical Physics](#) Vol. 36, 3 (Courier Corporation, 1975).
- [18] W. Nolting and W. D. Brewer, [Fundamentals of Many-body Physics](#) (Springer, Berlin, Heidelberg, 2009).
- [19] G. C. Wick, “The Evaluation of the Collision Matrix”, [Physical Review](#) **80**, 268–272 (1950).
- [20] L. G. Molinari, [Notes on Wick’s Theorem in Many-Body Theory](#), Oct. 14, 2023, pre-published.
- [21] M. Helias and D. Dahmen, “Linked Cluster Theorem”, in [Statistical Field Theory for Neural Networks](#), edited by M. Helias and D. Dahmen (Springer International Publishing, Cham, 2020), pp. 39–52.
- [22] J. Kaufmann, “Calculation of Vertex Asymptotics from Local Correlation Functions”, MA thesis (Technische Universität Wien, 2017).
- [23] P. Kappl, F. Krien, C. Watzenböck, and K. Held, “Nonlinear Responses and Three-Particle Correlators in Correlated Electron Systems Exemplified by the Anderson Impurity Model”, [Physical Review B](#) **107**, 205108 (2023).
- [24] C. Watzenböck, “Vertex Corrections in Strongly Correlated Electron Systems : Timescales of the Spin and Charge Response”, PhD thesis (Technische Universität Wien, 2022).
- [25] E. E. Salpeter and H. A. Bethe, “A Relativistic Equation for Bound-State Problems”, [Physical Review](#) **84**, 1232–1242 (1951).
- [26] Y. Nambu, “Force Potentials in Quantum Field Theory”, [Progress of Theoretical Physics](#) **5**, 614–633 (1950).
- [27] G. Rohringer, “New Routes towards a Theoretical Treatment of Nonlocal Electronic Correlations”, PhD thesis (Technische Universität Wien, 2013).
- [28] A. Galler, P. Thunström, P. Gunacker, J. M. Tomczak, and K. Held, “Ab Initio Dynamical Vertex Approximation”, [Physical Review B](#) **95**, 115107 (2017).
- [29] A. Galler, “Towards an Ab Initio Treatment of Materials with Local and Non-Local Electronic Correlations”, PhD thesis (Technische Universität Wien, 2017).
- [30] L. Hedin, “New Method for Calculating the One-Particle Green’s Function with Application to the Electron-Gas Problem”, [Physical Review](#) **139**, A796–A823 (1965).
- [31] F. Krien and A. Valli, “Parquetlike Equations for the Hedin Three-Leg Vertex”, [Physical Review B](#) **100**, 245147 (2019).

- [32] T. Schäfer, S. Ciuchi, M. Wallerberger, P. Thunström, O. Gunnarsson, G. Sangiovanni, G. Rohringer, and A. Toschi, “Nonperturbative Landscape of the Mott-Hubbard Transition: Multiple Divergence Lines around the Critical Endpoint”, [Physical Review B \*\*94\*\*, 235108 \(2016\)](#).
- [33] F. Krien, A. Valli, and M. Capone, “Single-Boson Exchange Decomposition of the Vertex Function”, [Physical Review B \*\*100\*\*, 155149 \(2019\)](#).
- [34] J. Kuneš, “Efficient Treatment of Two-Particle Vertices in Dynamical Mean-Field Theory”, [Physical Review B \*\*83\*\*, 085102 \(2011\)](#).
- [35] N. Wentzell, G. Li, A. Tagliavini, C. Taranto, G. Rohringer, K. Held, A. Toschi, and S. Andergassen, “High-Frequency Asymptotics of the Vertex Function: Diagrammatic Parametrization and Algorithmic Implementation”, [Physical Review B \*\*102\*\*, 085106 \(2020\)](#).
- [36] A. Tagliavini, S. Hummel, N. Wentzell, S. Andergassen, A. Toschi, and G. Rohringer, “Efficient Bethe-Salpeter Equation Treatment in Dynamical Mean-Field Theory”, [Physical Review B \*\*97\*\*, 235140 \(2018\)](#).
- [37] G. Li, N. Wentzell, P. Pudleiner, P. Thunström, and K. Held, “Efficient Implementation of the Parquet Equations: Role of the Reducible Vertex Function and Its Kernel Approximation”, [Physical Review B \*\*93\*\*, 165103 \(2016\)](#).
- [38] S. Hummel, “Asymptotic Behavior of Two-Particle Vertex Functions in Dynamical Mean-Field Theory”, MA thesis (Technische Universität Wien, 2014).
- [39] J. Kaufmann, P. Gunacker, and K. Held, “Continuous-Time Quantum Monte Carlo Calculation of Multiorbital Vertex Asymptotics”, [Physical Review B \*\*96\*\*, 035114 \(2017\)](#).
- [40] M. Kitatani, R. Arita, T. Schäfer, and K. Held, “Strongly Correlated Superconductivity with Long-Range Spatial Fluctuations”, [Journal of Physics: Materials \*\*5\*\*, 034005 \(2022\)](#).
- [41] P. Pudleiner, P. Thunström, A. Valli, A. Kauch, G. Li, and K. Held, “Parquet Approximation for Molecules: Spectrum and Optical Conductivity of the Pariser-Parr-Pople Model”, [Physical Review B \*\*99\*\*, 125111 \(2019\)](#).
- [42] A. Galler, J. Kaufmann, P. Gunacker, M. Pickem, P. Thunström, J. M. Tomczak, and K. Held, “Towards Ab Initio Calculations with the Dynamical Vertex Approximation”, [Journal of the Physical Society of Japan \*\*87\*\*, 041004 \(2018\)](#).
- [43] P. Pudleiner, A. Kauch, K. Held, and G. Li, “Competition between Antiferromagnetic and Charge Density Wave Fluctuations in the Extended Hubbard Model”, [Physical Review B \*\*100\*\*, 075108 \(2019\)](#).
- [44] P. Worm, “Numerical Analysis of Many-Body Effects in Cuprate and Nickelate Superconductors”, PhD thesis (Technische Universität Wien, 2023).
- [45] A. A. Katanin, A. Toschi, and K. Held, “Comparing Pertinent Effects of Antiferromagnetic Fluctuations in the Two- and Three-Dimensional Hubbard Model”, [Physical Review B \*\*80\*\*, 075104 \(2009\)](#).
- [46] N. Parragh, “A New Scheme for LDA+DMFT Calculations and Algorithmic Improvements for a Multi-Band DMFT-solver”, MA thesis (Technische Universität Wien, 2010).
- [47] M. Kinza and C. Honerkamp, “Two-Particle Correlations in a Functional Renormalization Group Scheme Using a Dynamical Mean-Field Theory Approach”, [Physical Review B \*\*88\*\*, 195136 \(2013\)](#).

- [48] W. Metzner and D. Vollhardt, “Correlated Lattice Fermions in  $d = \infty$  Dimensions”, [Physical Review Letters](#) **62**, 324–327 (1989).
- [49] A. Georges and G. Kotliar, “Hubbard Model in Infinite Dimensions”, [Physical Review B](#) **45**, 6479–6483 (1992).
- [50] K. Held, “Electronic Structure Calculations Using Dynamical Mean Field Theory”, [Advances in Physics](#) **56**, 829–926 (2007).
- [51] D. Vollhardt, “Dynamical Mean-Field Theory of Strongly Correlated Electron Systems”, in [Proceedings of the International Conference on Strongly Correlated Electron Systems \(SCES2019\)](#), Vol. 30, JPS Conference Proceedings 30 (Journal of the Physical Society of Japan, Mar. 18, 2020).
- [52] M. Wallerberger, A. Hausoel, P. Gunacker, A. Kowalski, N. Parragh, F. Goth, K. Held, and G. Sangiovanni, “W2dynamics: Local One- and Two-Particle Quantities from Dynamical Mean Field Theory”, [Computer Physics Communications](#) **235**, 388–399 (2019).
- [53] G. Kotliar, S. Y. Savrasov, K. Haule, V. S. Oudovenko, O. Parcollet, and C. A. Marianetti, “Electronic Structure Calculations with Dynamical Mean-Field Theory”, [Reviews of Modern Physics](#) **78**, 865–951 (2006).
- [54] G. Rohringer, A. Valli, and A. Toschi, “Local Electronic Correlation at the Two-Particle Level”, [Physical Review B](#) **86**, 125114 (2012).
- [55] C. Slezak, M. Jarrell, T. Maier, and J. Deisz, “Multi-Scale Extensions to Quantum Cluster Methods for Strongly Correlated Electron Systems”, [Journal of Physics: Condensed Matter](#) **21**, 435604 (2009).
- [56] J. Kaufmann, C. Eckhardt, M. Pickem, M. Kitatani, A. Kauch, and K. Held, “Self-Consistent Ladder Dynamical Vertex Approximation”, [Physical Review B](#) **103**, 035120 (2021).
- [57] L. Del Re and A. Toschi, “Dynamical Vertex Approximation for Many-Electron Systems with Spontaneously Broken  $SU(2)$  Symmetry”, [Physical Review B](#) **104**, 085120 (2021).
- [58] A. Valli, T. Schäfer, P. Thunström, G. Rohringer, S. Andergassen, G. Sangiovanni, K. Held, and A. Toschi, “Dynamical Vertex Approximation in Its Parquet Implementation: Application to Hubbard Nanorings”, [Physical Review B](#) **91**, 115115 (2015).
- [59] T. Schäfer, N. Wentzell, F. Šimkovic, Y.-Y. He, C. Hille, M. Klett, C. J. Eckhardt, B. Arzhang, V. Harkov, F.-M. Le Régent, A. Kirsch, Y. Wang, A. J. Kim, E. Kozik, E. A. Stepanov, A. Kauch, S. Andergassen, P. Hansmann, D. Rohe, Y. M. Vilk, J. P. F. LeBlanc, S. Zhang, A.-M. S. Tremblay, M. Ferrero, O. Parcollet, and A. Georges, “Tracking the Footprints of Spin Fluctuations: A MultiMethod, MultiMessenger Study of the Two-Dimensional Hubbard Model”, [Physical Review X](#) **11**, 011058 (2021).
- [60] K. Held, A. A. Katanin, and A. Toschi, “Dynamical Vertex Approximation: An Introduction”, [Progress of Theoretical Physics Supplement](#) **176**, 117–133 (2008).
- [61] J. Stobbe and G. Rohringer, “Consistency of Potential Energy in the Dynamical Vertex Approximation”, [Physical Review B](#) **106**, 205101 (2022).
- [62] P. Augustinský and V. Janiš, “Multiorbital Simplified Parquet Equations for Strongly Correlated Electrons”, [Physical Review B](#) **83**, 035114 (2011).

- [63] K.-M. Tam, H. Fotso, S.-X. Yang, T.-W. Lee, J. Moreno, J. Ramanujam, and M. Jarrell, “Solving the Parquet Equations for the Hubbard Model beyond Weak Coupling”, [Physical Review E \*\*87\*\*, 013311 \(2013\)](#).
- [64] A. Toschi, A. A. Katanin, and K. Held, “Dynamical Vertex Approximation: A Step beyond Dynamical Mean-Field Theory”, [Physical Review B \*\*75\*\*, 045118 \(2007\)](#).
- [65] J. M. Tomczak, P. Liu, A. Toschi, G. Kresse, and K. Held, “Merging GW with DMFT and Non-Local Correlations Beyond”, [The European Physical Journal Special Topics \*\*226\*\*, 2565–2590 \(2017\)](#).
- [66] N. D. Mermin and H. Wagner, “Absence of Ferromagnetism or Antiferromagnetism in One- or Two-Dimensional Isotropic Heisenberg Models”, [Physical Review Letters \*\*17\*\*, 1307–1307 \(1966\)](#).
- [67] T. Moriya, *Spin Fluctuations in Itinerant Electron Magnetism*, red. by P. Fulde, M. Cardona, and H.-J. Queisser, Vol. 56, Springer Series in Solid-State Sciences (Springer, Berlin, Heidelberg, 1985).
- [68] G. Rohringer and A. Toschi, “Impact of Nonlocal Correlations over Different Energy Scales: A Dynamical Vertex Approximation Study”, [Physical Review B \*\*94\*\*, 125144 \(2016\)](#).
- [69] A. S. Banerjee, P. Suryanarayana, and J. E. Pask, “Periodic Pulay Method for Robust and Efficient Convergence Acceleration of Self-Consistent Field Iterations”, [Chemical Physics Letters \*\*647\*\*, 31–35 \(2016\)](#).
- [70] J. Peil, “ $\lambda$ -Correction Meets Self-Consistency: Testing New Tools for Strongly Correlated Electron Systems”, BA thesis (Technische Universität Wien / Vienna University of Technology, 2022).
- [71] G. M. Eliashberg, “Interactions between Electrons and Lattice Vibrations in a Superconductor”, [Sov. Phys. - JETP \(Engl. Transl.\); \(United States\) \*\*11\*\*:3 \(1960\)](#).
- [72] F. Marsiglio, “Eliashberg Theory: A Short Review”, [Annals of Physics, Eliashberg Theory at 60: Strong-coupling Superconductivity and Beyond \*\*417\*\*, 168102 \(2020\)](#).
- [73] S. Käser, H. U. R. Strand, N. Wentzell, A. Georges, O. Parcollet, and P. Hansmann, “Interorbital Singlet Pairing in  $\text{Sr}_2\text{RuO}_4$ : A Hund’s Superconductor”, [Physical Review B \*\*105\*\*, 155101 \(2022\)](#).
- [74] Y. Yanase, T. Jujo, T. Nomura, H. Ikeda, T. Hotta, and K. Yamada, “Theory of Superconductivity in Strongly Correlated Electron Systems”, [Physics Reports \*\*387\*\*, 1–149 \(2003\)](#).
- [75] V. P. Mineev, K. Samokhin, and L. D. Landau, [Introduction to Unconventional Superconductivity](#) (CRC Press, Sept. 21, 1999), 204 pp.
- [76] J. Berges, “On the Scope of McMillan’s Formula”, MA thesis (Universität Bremen, Oct. 2016).
- [77] O. Gingras, R. Nourafkan, A.-M. S. Tremblay, and M. Côté, “Superconducting Symmetries of  $\text{Sr}_2\text{RuO}_4$  from First-Principles Electronic Structure”, [Physical Review Letters \*\*123\*\*, 217005 \(2019\)](#).
- [78] B. Putzer, [Multiband Eliashberg Theory](#) (Nov. 2023).
- [79] S. Yoshida, K. Yada, and Y. Tanaka, “Theory of a Pair Density Wave on a Quasi-One-Dimensional Lattice in the Hubbard Model”, [Physical Review B \*\*104\*\*, 094506 \(2021\)](#).



- [80] P. S. Riseborough, G. M. Schmiedeshoff, and J. L. Smith, “Heavy Fermion Superconductivity”, in [The Physics of Superconductors: Vol. II. Superconductivity in Nanostructures, High-T<sub>c</sub> and Novel Superc](#) edited by K. H. Bennemann and J. B. Ketterson (Springer, Berlin, Heidelberg, 2004), pp. 889–1086.
- [81] R. Nourafkan, G. Kotliar, and A.-M. S. Tremblay, “Correlation-Enhanced Odd-Parity Interorbital Singlet Pairing in the Iron-Pnictide Superconductor LiFeAs”, [Physical Review Letters](#) **117**, 137001 (2016).
- [82] M. Kitatani, T. Schäfer, H. Aoki, and K. Held, “Why the Critical Temperature of High-T<sub>c</sub> Cuprate Superconductors Is so Low: The Importance of the Dynamical Vertex Structure”, [Physical Review B](#) **99**, 041115 (2019).
- [83] A. Galler, P. Thunström, J. Kaufmann, M. Pickem, J. M. Tomczak, and K. Held, “The AbinitioDFA Project v1.0: Non-local Correlations beyond and Susceptibilities within Dynamical Mean-Field Theory”, [Computer Physics Communications](#) **245**, 106847 (2019).
- [84] P. Worm, [DGApy](#), Zenodo, Dec. 19, 2023.
- [85] S. Di Cataldo, P. Worm, J. M. Tomczak, L. Si, and K. Held, “Unconventional Superconductivity without Doping in Infinite-Layer Nickelates under Pressure”, [Nature Communications](#) **15**, 3952 (2024).
- [86] P. Worm, Q. Wang, M. Kitatani, I. Biało, Q. Gao, X. Ren, J. Choi, D. Csontosová, K.-J. Zhou, X. Zhou, Z. Zhu, L. Si, J. Chang, J. M. Tomczak, and K. Held, “Spin Fluctuations Sufficient to Mediate Superconductivity in Nickelates”, [Physical Review B](#) **109**, 235126 (2024).